

**Two-Photon Excited Fluorescence Microscopy for
the Non-Invasive Characterization of Brain Cell
Metabolism and Structure**

A thesis submitted by

Emily DeBaun Stuntz

In partial fulfillment of the requirements for the degree of

Master of Science

in

Biomedical Engineering

TUFTS UNIVERSITY

August 2016

Advisor: Dr. Irene Georgakoudi

ABSTRACT

Two-photon excited fluorescence (TPEF) imaging is a robust and versatile non-invasive, non-destructive, high-resolution technique for studying cell structure and function in 2- and 3-dimensional *in vitro* systems. This thesis describes three applications of TPEF for studying brain cell structure and function. In the first application, TPEF is used to capture endogenous fluorescence of NADH and FAD in 2D cultures of primary rat neurons and astrocytes, as well as in cultures of adult human neural progenitor cells (AHNPs). Analyzing distributions of pixel-wise optical redox ratios, defined as $FAD/(FAD+NADH)$, reveals differences in astrocyte and neuron metabolism consistent with their known tendencies towards glycolysis and oxidative phosphorylation, respectively. Alterations in astrocyte and neuron redox ratio distributions in response to manganese toxicity are consistent with apoptosis and oxidative stress, and are recapitulated in a study with Parkinson's Disease-derived AHNPs. The second application of TPEF utilizes an automated imaging approach to quantify network density of 3D bioengineered cortical tissue. The analysis successfully shows an increase in neurite density in cultures that incorporate ECM derived from adult or fetal brains vs. a collagen control. The third application describes efforts to calibrate a TPEF-based optical tweezer instrument to assess local microrheometry of brain tissue models. In sum, these experiments demonstrate the broad applicability of TPEF for characterizing brain cell and tissue structure and function *in vitro*.

ACKNOWLEDGEMENTS

It takes a village to write a thesis, and there are numerous people I am indebted to for their help and advice over the past two years. I would first like to thank my advisor, Professor Irene Georgakoudi, for her constant support and encouragement throughout my time at Tufts – her vision, mentorship, and deep biomedical optics expertise have been crucial to the conception and progress of these projects. I would also like to thank Professor David Kaplan for serving on my thesis committee, sharing his expertise in brain tissue engineering, and offering insightful feedback throughout various stages of experimental planning. I would also like to thank Dr. Giuseppina Tesco for agreeing to serve as a member of my committee and to offer feedback on our research from her neuroscience and neurodegeneration expertise. I would also like to thank Professor Mark Cronin-Golomb for sharing his expertise in optical tweezers, and in particular, for offering troubleshooting approaches regarding instrumentation for that project. I'm deeply grateful also to Dean Panetta and the Tufts SoE Dean's Office for their fellowship support over the past two years, without which I would not have been able to pursue this graduate degree.

Yusi Gong was an invaluable contributor to the metabolic imaging project, particularly in the area of data collection – I am greatly appreciative of her work ethic, consistency, and ideas over the past year. I would also like to thank the other past and present members of the Georgakoudi lab, in particular Joe Lyons

and Drs. Martin Hunter, Dimitra Pouli, Zhiyi Liu, Carlo Alonzo, and Kyle Quinn, for their willingness to patiently share their knowledge, offer advice, and help with experimental troubleshooting.

Collaborators in the Kaplan Laboratory and the Steindler Laboratory had critical involvement in the projects described in this thesis. I am very grateful to Disha Sood, Dr. Olga Liaudanskaya, and the other members of the Kaplan Brain Mini-Group for their help learning basic cell culture techniques and validation approaches, and for their regular collaboration in the isolation of primary rat brain cells. I would like also like to thank Dr. Tong Zheng and Dr. Dennis Steindler for collaborating and providing adult human neural progenitor (AHNP) samples for metabolic imaging.

Several other Tufts BME members offered their support over the past two years. Dr. Ben Partlow, Lauren Baugh, Marc Simon, and Berney Peng all contributed their knowledge of gel preparation and rheometry for the optical tweezers project. Milva Ricci, Meghan McGill, and the members of the OSA offered friendship and moral support throughout my time at Tufts.

Last, but certainly not least, I would like to thank many wonderful friends and especially my abundant local family – Andy, Mom, Dad, Dave, Kara, Andrew, Sarah, Sam, Liz, Ruth, and Herman – for their constant love and personal support through a hectic couple of years.

CONTENTS

Abstract.....	i
Acknowledgements.....	ii
I. Thesis Introduction.....	1
2. TPEF for the Characterization of Metabolism in Healthy Brain Cells and Neurodegenerative Disease Models.....	4
2.a. Background – Healthy and Diseased Brain Cell Metabolism.....	4
2.a.i. Brief Motivation for Studying Brain Cell Metabolism	4
2.a.ii. Metabolic Pathways in Brain Cells	5
2.a.iii Mitochondrial Dynamics	8
2.a.iv. Astrocytes and Neurons: Metabolic and Functional Features, Coupling.....	9
2.a.v. Metabolism in Parkinson’s Disease	12
2.a.vi. Manganese Poisoning as a Parkinson’s Disease Model.....	14
2.b. Background - Two-Photon Excited Fluorescence Imaging	19
2.b.i. Introduction to Fluorescence and Two-Photon Excitation	19
2.b.ii. TPEF for Monitoring Cell Metabolism Using Optical Redox Ratios.....	22
2.b.iii. Two-Photon Excited Fluorescence Lifetime Imaging	24
2.b.iv. Prior Studies of NADH and FAD Autofluorescence in Brain Tissue.....	27
2.b.v. Analysis of Mitochondrial Organization Using NADH Autofluorescence	29

2.c. Characterizing Astrocyte and Neuron Metabolism Using TPEF – Monocultures, Co-Cultures, and Manganese Toxicity.....	31
2.c.i Introduction.....	31
2 c.ii. Materials and Methods.....	32
2.c.iii. Results.....	50
2.c.iv. Discussion	76
2.d. Characterizing normal vs. diseased cell metabolism in adult human neural progenitor cells (AHNPs) derived from healthy and Parkinson’s patients	86
2.d.i. Introduction.....	86
2.d.ii. Materials and Methods	86
2.d.iii. Results	89
2.d.iv. Discussion.....	92
3. Automated Image Analysis for Neurite Density Quantification in a 3D Bio-engineered Brain Model	94
3.a. Background and Introduction.....	95
3.b. Materials and Methods.....	96
3.b.i. Data Collection	96
3.b.ii. Image Analysis Approach.....	97
3.b.iii. Statistics.....	98
3.c. Results.....	99

3.d. Discussion.....	101
4. Optical Tweezers for the Study of Local Biomechanics.....	102
4.a. Introduction and Background.....	102
4.b. Materials and Methods.....	105
4.b.i. Instrumentation	105
4.b.ii. Preparation of calibration gels	107
4.b.iii. Image Analysis	108
4.b.iv. Statistics	109
4.b.v. Notes on alternative methods:.....	109
4.c. Results	113
4.c.i. Measurements in Polyacrylamide Gels	113
4.c.ii. Measurements in Collagen Gels	115
4.d. Discussion.....	117
5. Thesis Conclusions and Future Research Directions	121
6. Appendix.....	126
7. References.....	143

LIST OF FIGURES

Figure 1: Schematic of glycolytic and mitochondrial ATP production. Reproduced from [7]	5
Figure 2 : The electron transport chain (ETC).....	7
Figure 3: Diagrams of neuron (a) and astrocyte (b) morphology. Reproduced from [2],[6]	9
Figure 4: The role of PDH and Pfkfb3 in neuron and astrocyte metabolism. Modified from [8]	10
Figure 5: The Astrocyte-Neuron Lactate Shuttle – reproduced from [8]	11
Figure 6: Parkinson’s Disease is characterized by loss of pigmented dopaminergic neurons in the substantia nigra. Reproduced from [5, 6]	12
Figure 7: Pathways of manganese toxicity in brain cells.....	16
Figure 8: Manganese toxicity disrupts normal metabolic coupling between astrocytes and neurons	17
Figure 9: Jablonski diagram of processes involved in fluorescence.....	19
Figure 10: The Stokes Shift	20
Figure 11: Two-photon absorption	20
Figure 12: (a) Two-photon absorption spectra of NADH and FAD (b) Fluorescence emission spectra of NADH and FAD; Reproduced from [7]	22

Figure 13: Schematic of time-correlated single photon counting (TCSPC). Modified from [1]	24
Figure 14: Phasor plot of a biexponential decay.....	26
Figure 15: Schematic of the sandwich co-culture setup	33
Figure 16: Schematic of transwell co-culture used to image neurons; the opposite cell type arrangement was used to image astrocytes.	34
Figure 17: Scattering correction on reference dye emission spectra	39
Figure 18: Cell excitation spectra before and after corrections	41
Figure 19: Cell excitation spectra before and after corrections	42
Figure 20: Fluorescein excitation spectrum pre-and post-corrections.....	42
Figure 21 Astrocyte (a) and neuron (b) emission spectra when excited at 755 or 860nm	49
Figure 22: Relative contribution of NADH/FAD at each excitation wavelength based on spectral fitting	50
Figure 23 : Basis emission spectra for spectral fitting.....	50
Figure 24: Excitation spectra of astrocytes and neurons relative to the 460nm channel.	51
Figure 25 (a-b) Transmission images of astrocyte and neuron morphology (c-d) Redox ratio maps (e-f) False-coloring based on gaussian components (g-h) Redox histograms and fits	52

Figure 26: Gaussian components unmixed from aggregate monoculture redox ratio distributions	53
Figure 27: Aggregate redox histograms of neurons and astrocyte monocultures.	53
Figure 28 Astrocyte and Neuron relative component weights.....	54
Figure 29: Neurons with normal morphology (green box) exhibit combinations of all three redox ratio components, while neurons with nuclear blebbing and abnormal morphology (red box) have higher redox ratio and are dominated by component 3.....	55
Figure 30: Relative weights of redox Gaussian components for astrocyte and neuron monocultures.....	55
Figure 31: (a-b) NADH intensity (c-d) Masks for PSD analysis (e-f) Cloned images (g-h) PSD curves characterizing mitochondrial organization	56
Figure 32: Astrocyte and neuron clustering β values	56
Figure 33: Aggregate phasor plots of astrocytes and neurons	57
Figure 34: False-colored FLIM images of astrocytes and neurons.....	57
Figure 35: Phasor FLIM metrics of neuron and astrocyte monocultures. (a) Bound fraction (b) Image-wise standard deviation of bound fraction.....	58
Figure 36 Effects of increasing doses of MnCl_2 on neuron morphology and redox ratio. (a-d) Transmittance images (e-h) Redox ratio maps (i-l) Redox component maps	59

Figure 37 Neuron redox ratio histograms with increasing MnCl_2 dose.....	59
Figure 38: When treated with increasing doses of MnCl_2 , neurons display a drop in weight of component 2, and increases in weight of component 3.....	60
Figure 39: Caspase-3 assay in control vs. Mn-treated neurons	61
Figure 40: Relative weights redox ratio components in Mn-treated neuron monocultures (a) $W1/(W2+W3)$ (b) $W2/(W1+W3)$ (c) $W3/(W1+W2)$	61
Figure 41: Effects of increasing doses of MnCl_2 on astrocyte morphology and redox ratio. (a-d) Transmittance images (e-h) Redox ratio maps (i-l) Redox component maps	62
Figure 42: Redox histograms of MnCl_2 -treated astrocytes reveal a shift to the right with increasing doses, similar to neurons, but at higher concentrations.....	63
Figure 43 Astrocytes see a MnCl_2 . dose-dependent increase in weight of component 3 and decrease in weights 1 and 2.....	63
Figure 44: When astrocytes are treated with sufficiently high doses of Mn, they show a decrease in relative weights of components 1 and 2, and an increase in component 3.....	64
Figure 45: Caspase-3 assay in control and Mn-treated astrocytes	65
Figure 46: NADH intensity images (a-b), masks (c-d), cloned images (e-f), and PSD curves (g-h) for neurons with and without Mn treatment.....	66

Figure 47 NADH intensity images (a-b), masks (c-d), cloned images (e-f), and PSD curves (g-h) for astrocytes with and without Mn treatment	66
Figure 48: Neuron β value is not significantly different between treatment groups.	67
Figure 49: Astrocyte β value increases between 0 and 750 uM treatment	67
Figure 50: NADH fluorescence lifetime images of neurons with and without 500 μ M Mn (a-b) and astrocytes with and without 1000 μ M Mn (c-d).....	68
Figure 51: Phasor plots of NADH lifetime data from untreated (a) and Mn-treated (b) neurons	68
Figure 52: (a) Control vs. Mn-treated astrocyte bound fraction (b) Control vs. Mn-treated astrocyte imagewise bound fraction standard deviation	69
Figure 53: Phasor plots of NADH lifetime data from untreated (a) and Mn-treated (b) astrocytes	69
Figure 54: (a) Control vs. Mn-treated neuron bound fraction (b) Control vs. Mn-treated neuron imagewise bound fraction standard deviation.....	69
Figure 55: Relative redox component values in sandwich co-cultures.....	70
Figure 56: Redox histograms for sandwich co-cultures	71
Figure 57: Redox ratio distributions for astrocytes (a) and neurons (b) in transwell experiments	72

Figure 58: Redox ratio distributions for astrocytes (a) and neurons (b) in conditioned-media experiments	72
Figure 59: Redox ratio components in media transfer experiments	73
Figure 60: Redox ratio components for media conditioning experiments.....	73
Figure 61: Redox distributions for transwells treated with Mn	75
Figure 62: Redox distributions for sandwich co-cultures treated with Mn	75
Figure 63: Redox components for transwell co-cultures treated with Mn.....	76
Figure 64: Redox components for sandwich co-cultures treated with Mn	76
Figure 65: Images of control and PD-derived AHNPs (a-b) Transmittance images (c-d) Redox maps (e-f) False-colored redox components (g-h) Redox histograms with fits	89
Figure 66: Redox ratio distributions for control and PD-derived AHNPs.....	91
Figure 67: Gaussian redox components un-mixed from the control AHNP redox distribution.	91
Figure 68: Redox components for AHNPs	92
Figure 69: Component weights for AHNPs.....	92
Figure 70: Clustering results for AHNPs.....	93
Figure 71 Control vs. PD-derived AHNP NADH intensity images (a-b) image masks (c-d) cloned images (e-f) and PSD curves (g-h)	94

Figure 72: Representative images and masks from various ECM conditions (a-c)	
Maximum projection images of z-stacks (d-f) Representative raw images (g-i)	
Neurite masks (j-l) Background area masks	99
Figure 73: Comparison of neurite network density between ECM and	
matricellular protein conditions.	100
Figure 74: Schematic of imaging and optical tweezing setup. Reproduced from	
[3, 4].	106
Figure 75: (a) Raw bead image (b) Normalized bead image (c) Bead mask (d)	
Mask with ellipsoid fit	108
Figure 76 The apparent size of polystyrene beads in a 23- and 6-pascal	
polyacrylamide gel.....	113
Figure 77: Comparison of apparent bead diameters in polyacrylamide gel	115
Figure 78: The apparent size of carboxyl-functionalized beads in a 15 pa collagen	
gel prepared with a low concentration (0.3mg/ml) of EDC.....	116
Figure 79: The apparent size of carboxyl-functionalized beads in a 15 pa collagen	
gel prepared with a high concentration (10mg/ml) of EDC	117

I. THESIS INTRODUCTION

The brain is one of the most complex and important organs in the human body, responsible for functions as diverse as motion control, sensory integration, learning, memory, and emotion, to name just a few [9]. Understanding brain function and dysfunction is a massive research effort across scientific disciplines and length scales, motivated largely by efforts to understand and treat neurodegenerative diseases and traumatic brain injury (TBI). Neurodegenerative diseases, such as Parkinson's Disease and Alzheimer's Disease, are characterized by progressive brain cell death [10]. In older adults, Alzheimer's Disease is the major cause of dementia, a cognitive condition that impacts 6-7% of the North American population above age 60 [11]. Parkinson's Disease has cognitive impacts in addition to severe effects on motor function; its prevalence is 1-2% in the 60+ population of developed nations [12]. TBI is another major public health concern, with an estimated 2.4 million cases in 2009; approximately 5.3 million individuals in the US are currently disabled due to TBI, placing a substantial emotional and psychological burden on caregivers, as well as a tremendous financial burden on the broader healthcare system [13, 14]. An improved understanding of cell-level dysfunction and injury mechanisms is desperately needed to devise novel diagnostics and treatments for neurodegenerative diseases and traumatic brain injury; advances in basic science are crucial to improve

quality of life for patients and caregivers and to reduce the public health burden of these conditions.

Optical imaging approaches are well-suited to study disease and injury mechanisms at the cellular level. Techniques such as two-photon excited fluorescence (TPEF) microscopy allow non-invasive, non-destructive assessment of cells either via endogenous fluorescence or with the aid of exogenous contrast agents [7]. TPEF has the advantage of providing high-resolution images with minimal photobleaching, enabling live cell imaging, as well as adequate depth penetration and optical sectioning for probing thick specimens such as 3D engineered brain tissue [15]. TPEF is therefore well-suited to both capture brain tissue structure and function in a variety of *in vitro* models.

This thesis describes three applications of TPEF imaging for the study of brain cells in *in vitro* cultures. The first application employs TPEF to capture cell function; brain cell metabolism is assessed via two-photon imaging of NADH and FAD autofluorescence. We use optical redox imaging, fluorescence lifetime imaging, and mitochondrial organization analysis to characterize metabolic differences between healthy brain cell types in addition to cell responses to manganese, a known neurotoxin. We also use optical redox imaging and mitochondrial organization analysis to characterize differences between healthy and Parkinson's Disease-derived adult neural progenitor cells. The second application uses automated image analysis of TPEF z-stacks from engineered

brain tissue to identify differences in neurite network density between experimental extracellular matrix conditions. The third application discusses approaches to building a TPEF-based optical tweezing microrheometry instrument with potential applications in neural tissue engineering. Together, these projects illustrate how TPEF imaging is a robust and broadly applicable technique for studying brain tissue structure and function.

2. TPEF FOR THE CHARACTERIZATION OF METABOLISM IN HEALTHY BRAIN CELLS AND NEURODEGENERATIVE DISEASE MODELS

2.A. BACKGROUND – HEALTHY AND DISEASED BRAIN CELL METABOLISM

2.A.1. *BRIEF MOTIVATION FOR STUDYING BRAIN CELL METABOLISM*

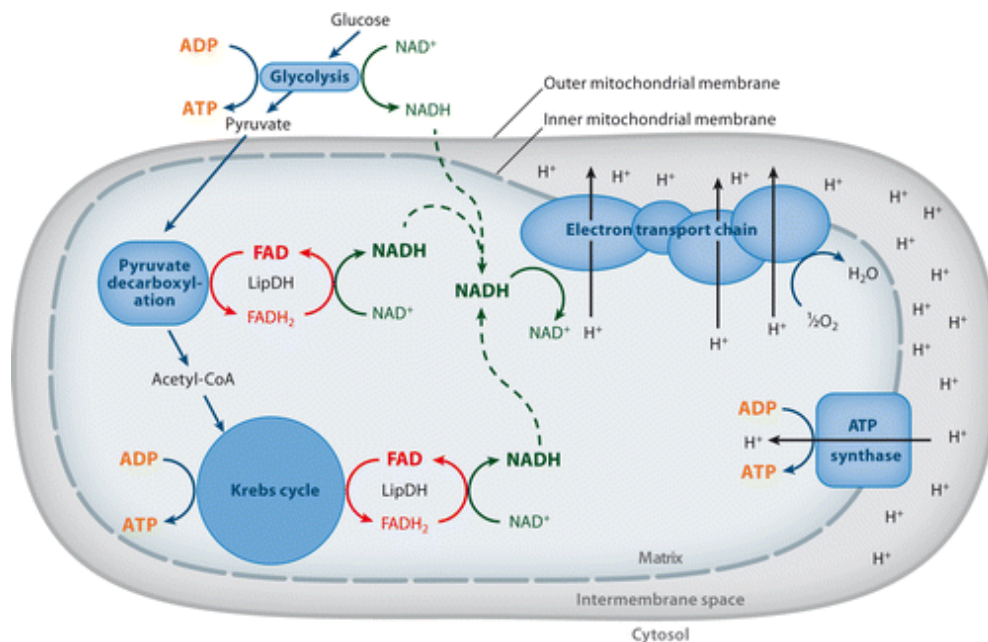
The brain is an energetically demanding organ; in spite of only making up 2% of the body's mass, it is responsible for 20% of its energy usage [16]. Proper glucose metabolism is responsible for both maintaining baseline brain electrophysiology (~30% of glucose usage), and for enabling spontaneous brain activity (~70% of glucose usage) [17]. Understandably, malfunctions in brain cell metabolism have grave consequences and are thought to be in part responsible for debilitating neurodegenerative diseases, including Alzheimer's disease and Parkinson's disease [10]. A concurrent and interdependent combination of mitochondrial dysfunction and oxidative stress are thought to be involved in neurodegeneration [10]; however, exact mechanisms are not yet well understood and continue to be a focus of research studies.

An improved understanding of both healthy and diseased brain cell metabolism, on the cellular level, is needed in order to develop novel strategies for diagnosing and treating neurodegenerative diseases. Quantitative optical metabolic imaging utilizing two-photon microscopy provides a non-destructive, high-resolution approach to monitoring cellular metabolic function via cell auto-

fluorescence [7]. Optimizing such imaging approaches for *in vitro* 2-dimensional brain cell cultures lays the groundwork for future studies in more complex 3-D cultures or *in vivo* systems, ultimately allowing researchers to tackle a range of questions regarding brain cell metabolism in both diseased and healthy tissues.

2.A.II. METABOLIC PATHWAYS IN BRAIN CELLS

Brain cells process glucose through three major metabolic pathways: glycolysis, mitochondrial processes (e.g., oxidative phosphorylation and the Krebs cycle), and the pentose phosphate pathway [8]. Glycolysis and mitochondrial processes each result in adenosine triphosphate (ATP) production (Figure 1). Glycolysis occurs outside of the mitochondria, when glucose is processed into pyruvate while converting NAD^+ to NADH and producing ATP




 Georgakoudi I, Quinn KP. 2012.
Annu. Rev. Biomed. Eng. 14:351–67

Figure 1: Schematic of glycolytic and mitochondrial ATP production.
Reproduced from [7]

[7, 8]. Glycolysis does not require oxygen and, in many cells, is preferred only in anaerobic conditions. However, some cell types, such as astrocytic brain cells, produce energy via both oxidative phosphorylation and glycolysis under normal oxygen conditions [8].

Mitochondrial processes, including the Krebs cycle (also known as the tri-carboxylic acid cycle or citric acid cycle) and oxidative phosphorylation, have a much higher energy yield than glycolysis [8]. Processes in the mitochondria involve numerous reduction-oxidation reactions to produce ATP; these reactions lead to varying concentrations of coenzymes nicotinamide adenine dinucleotide (NADH) and flavin adenine dinucleotide (FAD) [7]. First, in pyruvate decarboxylation, pyruvate dehydrogenase (PDH) converts pyruvate into acetyl-CoA, which reduces coenzyme FAD into FADH_2 , which may in turn reduce one NAD^+ to NADH [7]. Next, acetyl-CoA will enter the Krebs cycle to produce ATP; for each acetyl-CoA molecule that undergoes this process, three NAD^+ molecules are reduced to NADH with charge donated from FADH_2 [7].

ATP production subsequently occurs through oxidative phosphorylation via the electron transport chain (ETC) (Figure 2). The ETC involves a series of five complexes of the mitochondrial inner membrane which use energy released from oxidation of electron donors such as NADH and FADH_2 to pump protons out of the inner mitochondrial membrane, producing a charge gradient across the inner mitochondrial membrane [7]. The first of these complexes (Complex I)

exchanges NADH for NAD⁺ and uses the energy released to pump a proton out of the inner membrane [18]. The second of these complexes performs a similar exchange with FADH₂, reducing it to FAD [19]. Complexes III and IV continue to build the proton gradient while transporting the electrons from Complexes I and II; these electrons ultimately react with oxygen to form water [20]. ATP is finally formed from adenosine diphosphate (ADP) via the ATP synthase (also known as Complex V), which is stimulated by charges flowing back into the cell along the charge gradient produced by the other complexes [7].

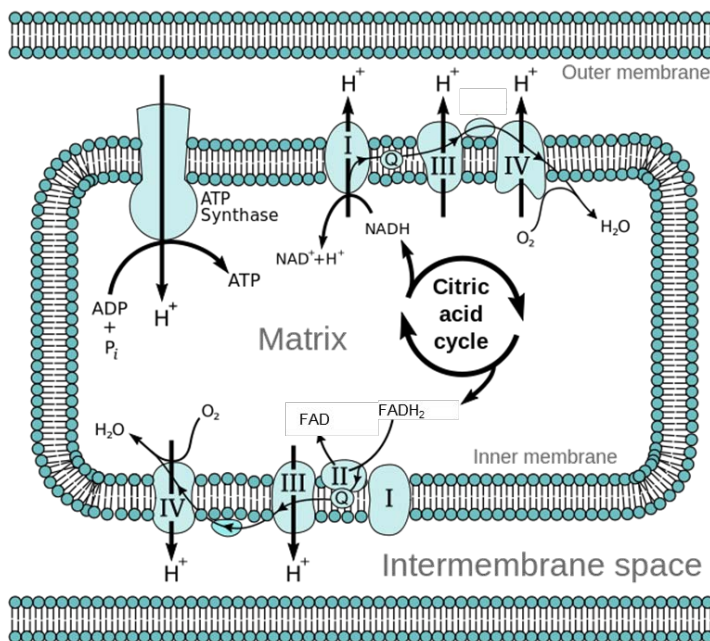


Figure 2 : The electron transport chain (ETC)

The pentose phosphate pathway (PPP) is the final metabolic pathway used to process glucose in brain cells. Unlike glycolysis and mitochondrial processes, the PPP does not result in ATP production.

However, the PPP is still essential to cell health, notably by producing reducing equivalents to maintain the redox balance of the cell by cycling NADP⁺ with NADPH [8, 21]. The PPP occurs in the cytosol [21].

2.A.III MITOCHONDRIAL DYNAMICS

Mitochondria are not static, separated organelles within cells, but rather undergo dynamic processes of fusion and fission in networks in order to carry out several key functions [22]. Mitochondrial networks generally allow for adaptive formation and distribution of ATP within a cell, based on energy demand in various parts of the cell [22]. The usual fusion-fission cycles of mitochondria preserve mitochondrial DNA and ensure structural, electrical, and chemical homeostasis of the mitochondrial networks [23]. Both fission and fusion play important roles in mitochondrial and cellular health. Mitochondrial fusion allows for mitochondrial DNA (mtDNA) exchange and complementation to occur, providing quality control for mtDNA [22]. Fusion also allows mitochondria to share proteins and metabolites and may also allow for continued energy production under stress conditions [23, 24]. Fission ensures proper distribution of mitochondrial DNA during mitochondrial reproduction, regulates mitochondrial placement within the cell, and triggers disposal of damaged DNA [22, 23]. When fission dominates over fusion, mitochondria appear fragmented or clumpy [22]. When fusion dominates over fission, mitochondria appear to form connected networks [22]. Defects in either fusion or fission may lead to an imbalance in the relative processes, potentially jeopardized mtDNA quality and accelerating apoptosis [22].

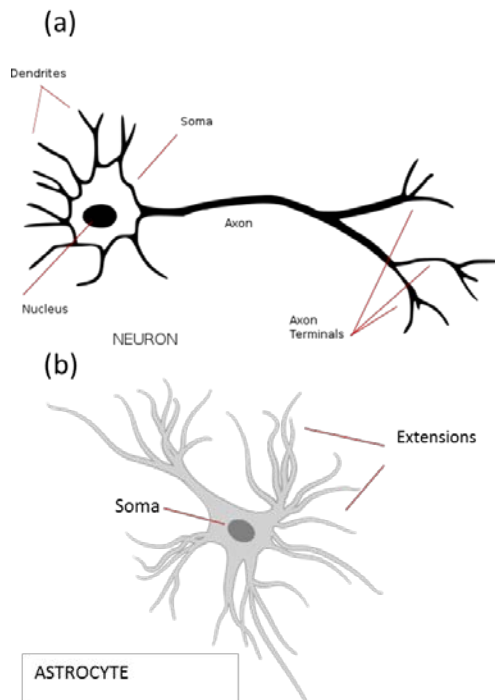


Figure 3: Diagrams of neuron (a) and astrocyte (b) morphology. Reproduced from [2],[6]

2.A.IV. ASTROCYTES AND NEURONS: METABOLIC AND FUNCTIONAL FEATURES, COUPLING

Neurons and astrocytes are two primary cell types within brain tissue, and each has a distinct function and metabolic profile. The relative number of astrocytes to neurons in the brain increases with brain complexity, with a ratio of roughly 1:3 in rodents and 2:3 in humans [25]. Neurons are the electrically active cells within the brain; their distinct morphology includes extensions known as axons and dendrites

(Figure 3), which allow propagation of electrical signals between cells at junctions known as synapses [26]. These extensions typically form dense networks to allow for intercellular signaling. Astrocytes have broader cell bodies and extensions and support neurons both structurally and functionally (Figure 3). Astrocytes help maintain the ion balances necessary for neuron health [26]. They also convert glutamate, a neurotransmitter, to its precursor glutamine in order to prevent excitotoxicity at the synaptic cleft and allow for efficient neurotransmitter synthesis [26]. Astrocytes are also thought to support neuron metabolism, which we will now discuss in more detail [8].

Astrocytes and neurons have contrasting, complementary metabolic characteristics. Many studies have asserted that astrocytes tend to produce energy primarily through glycolysis, likely due to gene expression leading to the deactivation of PDH, reducing their ability to generate energy via mitochondrial processes (Figure 4) [8, 27]. However, it is important to note that astrocytes do have mitochondria, and other studies have demonstrated that TCA cycle enzymes are highly expressed in these cells [28]. It seems likely that both glycolytic and mitochondrial processes occur within astrocytes, but that relative rates of

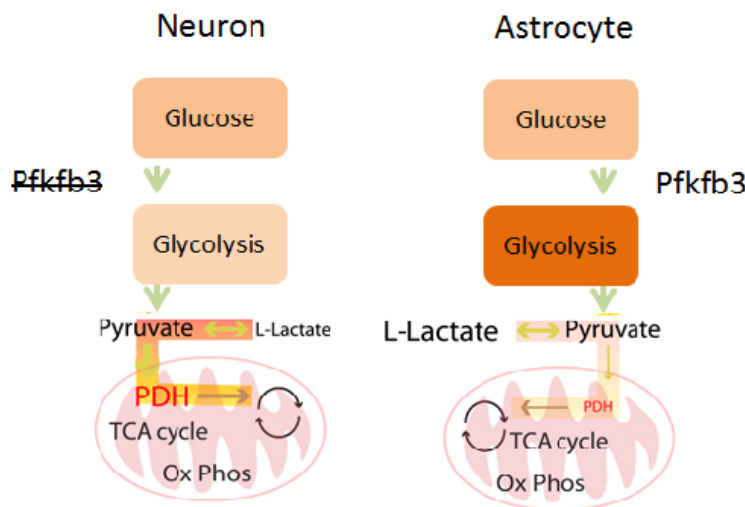


Figure 4: The role of PDH and Pfkfb3 in neuron and astrocyte metabolism. Modified from [8]

glycolysis vs. oxidative metabolism are higher than in neurons. Metabolism type may depend on specific energy demands and spatial location within astrocytes. Oxidative metabolic activities are thought to more typically occur in astrocytes' cell bodies while more glycolytic activities occur in extensions [29].

Neurons tend to generate energy through oxidative processes. In contrast to astrocytes, neurons have high activation of pyruvate dehydrogenase, allowing for import of pyruvate into the mitochondria (Figure 4) [8] [27]. Neurons also degrade PFKFB3, a glycolysis-promoting enzyme, preventing them from responding with glycolysis when mitochondrial energy production is inhibited (Figure 4) [8] [30]. Given that PFKFB3 degradation would also prevent neurons from fully processing glucose, it has been postulated that neurons generate energy from external sources of lactate / pyruvate and use glucose primarily to produce reducing equivalents through the pentose phosphate pathway to reduce oxidative stress [8].

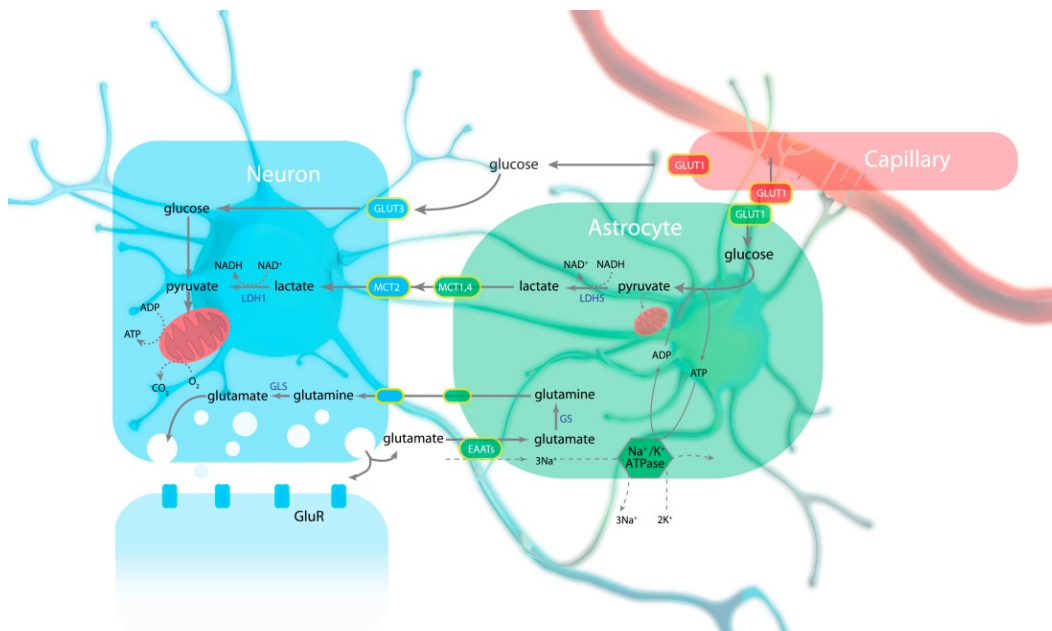


Figure 5: The Astrocyte-Neuron Lactate Shuttle – reproduced from [8]

As their complementary metabolic profiles might suggest, astrocytes and neurons are thought to have interdependent metabolisms. The “astrocyte-neuron

lactate shuttle” is one theory of brain cell metabolic coupling; it postulates that energy demands at the synapse cause astrocytes to produce lactate via glycolysis, which is shuttled to neurons as an energy substrate for oxidative phosphorylation (Figure 5) [8]. The coupling is further enhanced by astrocytes’ ability to store glucose as glycogen, which can be synthesized into lactate and offered to neurons as an energy substrate as needed [31]. Though exact mechanisms may remain up for debate, it is agreed that astrocytes play an essential role in promoting healthy neuronal metabolism and oxidative balance.

2.A.V. *METABOLISM IN PARKINSON’S DISEASE*

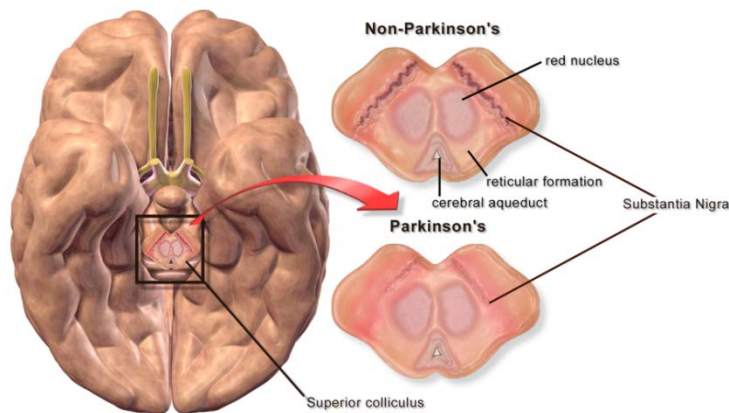


Figure 6: Parkinson’s Disease is characterized by loss of pigmented dopaminergic neurons in the substantia nigra. Reproduced from [5]

Parkinson’s disease (PD) is a common neurodegenerative condition that impacts ~1-2% of the population over 60 years old in developed countries [12, 32].

PD is typically diagnosed based on clinical features including bradykinesia, rigidity, tremor, or balance difficulty, and may be confirmed post-mortem based

upon brain features [12]. PD is characterized by loss of dopaminergic neurons in the substantia nigra, a portion of the basal ganglia essential to motor control (), and accumulation of protein aggregates known as Lewy bodies [32, 33]. In addition to the motion consequences of the disease, patients with PD may be more likely to suffer from psychiatric or cognitive difficulties and die sooner than their non-PD counterparts [12]. There are numerous potential causes of PD; old age and smoking are the main risk factors tied to Parkinson's, but genetic and other environmental causes have been proposed as well [12]. Only about 10% of cases are believed to be caused by strict Mendelian inheritance; others are thought to result from a complex combination of genetic susceptibilities and environmental factors [12].

PD's pathogenesis is complex and not well-defined, but is thought to involve mitochondrial dysfunction and oxidative stress among other factors [33]. Many patients with PD have shown reduced mitochondrial complex I activity in a range of cell types; however, the reduction in complex I activity alone is insufficient to explain the degree of neuronal death seen in PD patients, and may therefore play a greater role in cell death by increasing susceptibility to neurotoxins than by directly causing energy failure [32]. Complex I inhibition or dysfunction may also promote the formation of reactive oxygen species (ROS), such as superoxide, which then go on to critically damage mitochondrial DNA, lipids, and proteins essential to healthy cell function, including complex I itself

[23, 32]. Oxidative stress and ROS generation can also jeopardize the integrity of the mitochondrial membrane by leading to the formation of the mitochondrial permeability transition pore, a pore in the inner mitochondrial membrane which initiates apoptosis, resulting in subsequent apoptosis-inducing factor (AIF) release and caspase pathway initiation [34].

Mitochondrial dysfunction in PD (e.g., complex I inhibition) can also impact mitochondrial morphology and typical cycles of fission and fusion [32]. A number of studies have suggested that complex I inhibition disrupts the typical fusion-to-fission balance, resulting in an increase in mitochondrial fragmentation and ultimately cell death [35]. In some genetic cases of PD, problems with mutations in the PINK1 and parkin genes, normally involved in protein autophagy and quality control, may disrupt mitochondrial fission and fusion; parkin may also play a role in sporadic (non-genetic) cases of PD [36, 37].

2.A.VI. MANGANESE POISONING AS A PARKINSON'S DISEASE MODEL

Manganism is a condition caused by environmental exposure to toxic levels of manganese (Mn) which mimics the effects of PD [38]. Manganese exposure may occur through many routes, including water or food ingestion, inhalation while performing an occupation such as mining or welding, or intravenous delivery of total parenteral nutrition or medical imaging contrast agents containing Mn [38]. Manganism is characterized in its early stages by psychotic episodes, and later by motion-related symptoms similar to PD,

including rigidity, bradykinesia, and dystonia [39]. Mn accumulation in the brain also mimics the tissue-level effects of Parkinson's disease, including neuronal death and glial scarring in brain regions associated with motion signaling and control, including the substantia nigra [39]. As with PD, the way in which Mn specifically causes selective neuronal death and glial activation cannot be attributed to a single pathway or effect, but rather to a variety of interacting effects whose relative contribution and causal interdependence are not yet well-established [39, 40]. However, similar to PD, many of these effects involve the mitochondria, where manganese is actively sequestered [41].

Manganese can lead to cell death through a variety of interconnected pathways (Figure 7). Studies have consistently shown that manganese alters cells' oxidative energy metabolism and increases mitochondrial reactive oxygen species (ROS) production, however the direct site and mode of impact remain an area of active research [39, 40]. Studies report that manganese treatment results in depolarization of the mitochondria and inhibition of the respiratory chain [39, 40, 42]. With regard to site of action, studies report that (as with PD) complex I is inhibited by Mn, but that other mitochondrial complexes may also see decreased activity as well [43, 44]. Inhibition of the respiratory chain increases ROS production, which can cause further mitochondrial damage via oxidation [40]. Mn itself can also change oxidation states and either directly oxidize other molecules in the mitochondria, or generate ROS in the process of changing oxidation states

[38]. These effects may also be caused in part by calcium increases in the mitochondria resulting from Mn toxicity. Mn increases Ca^{2+} within mitochondria because it is imported into mitochondria via the Ca^{2+} uniporter and can

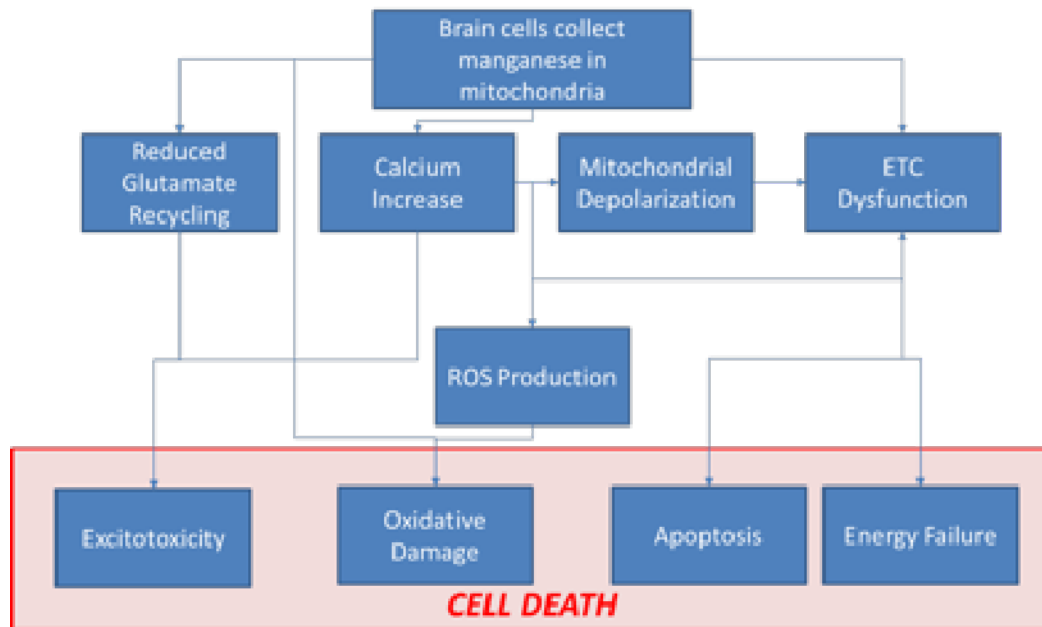


Figure 7: Pathways of manganese toxicity in brain cells.

competitively inhibit Ca^{2+} efflux from the cells [41, 45]. Calcium imbalances are associated with increased ROS production and may also play a role in neuronal excitotoxicity [39, 46].

Apoptosis is another well-documented result of Mn toxicity. Studies have reported increases in various apoptosis markers in primary neurons, astrocytes, and PC-12 cells with administration of varying doses of Mn [47-50]. Calcium increases in mitochondria are thought to contribute to apoptosis by accelerating the mitochondrial membrane permeability transition [45, 51]. ROS production

and complex I inhibition have also been proposed as factors triggering apoptosis, however some have argued that Mn^{2+} itself has antioxidant capacities which could neutralize some of the ROS to reduce the chance of apoptosis [40, 48].

Manganese affects astrocytes' and neurons' metabolisms differently, and can upset coupling between them (Figure 8). While astrocytes sequester manganese in higher concentrations than neurons and do experience alterations in metabolism, they have multiple robust energy production avenues (e.g., oxidative phosphorylation, glycolysis, glycogenolysis) and are therefore more resilient to Mn's effects than neurons [39, 50]. However, astrocytes' metabolic response to

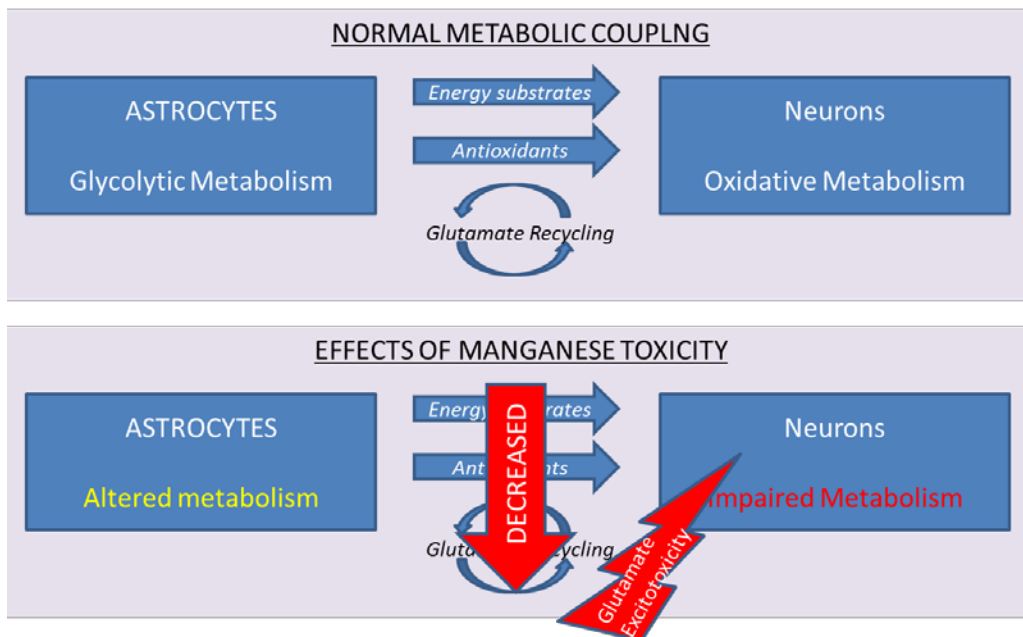


Figure 8: Manganese toxicity disrupts normal metabolic coupling between astrocytes and neurons

Mn reallocates energy resources normally devoted to several functions meant to

promote neuronal health [52]. Astrocytes affected by Mn may produce fewer energy substrates for neurons, fewer antioxidants, and have less capacity for recycling glutamate neurotransmitters into glutamine [53, 54]. As a result, neurons may face energy failure, ROS damage, and excitotoxicity due to excessive extracellular glutamate [50].

Relatively recent research has also connected manganese toxicity with changes in mitochondrial dynamics and associated genes. Two studies observed changes in mitochondrial-shaping proteins Opa-1 (associated with fusion) and Drp-1 (associated with fission) in rat astrocytoma C6 cells and Gli36 cells [55, 56]. In both studies, researchers observed shifts in Mn-treated cells toward mitochondrial fragmentation in conjunction with Opa-1 and Drp-1 changes and increased apoptosis markers [55, 56]. Other studies examined the effect of Mn treatment on expression of parkin in SH-SY5Y cells and concluded that Mn may up-regulate parkin expression in an effort to protect cells against apoptosis [57, 58]. These initial studies suggest that manganese treatment may impact mitochondrial shaping in ways similar to PD.

2.B. BACKGROUND - TWO-PHOTON EXCITED FLUORESCENCE IMAGING

2.B.1. INTRODUCTION TO FLUORESCENCE AND TWO-PHOTON EXCITATION

Fluorescence is a radiative process that can provide a source of contrast in optical imaging (Figure 9). When an incident photon is absorbed by a molecule in tissue, it may excite that molecule to a higher electronic energy state, if there is a

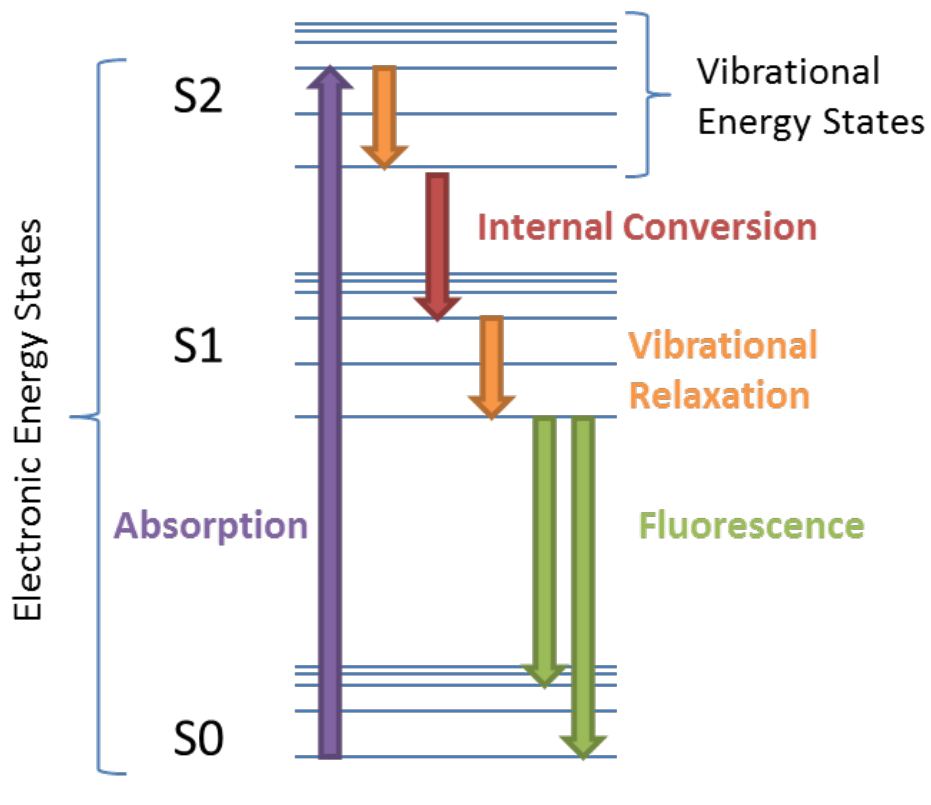


Figure 9: Jablonski diagram of processes involved in fluorescence

match between the energy carried by the photon and the distance between electronic energy states in the molecule [59]. Once excited, the molecule may relax to a lower vibrational energy state within the same electronic state, a process known as vibrational relaxation; it may also relax to a lower excited electronic

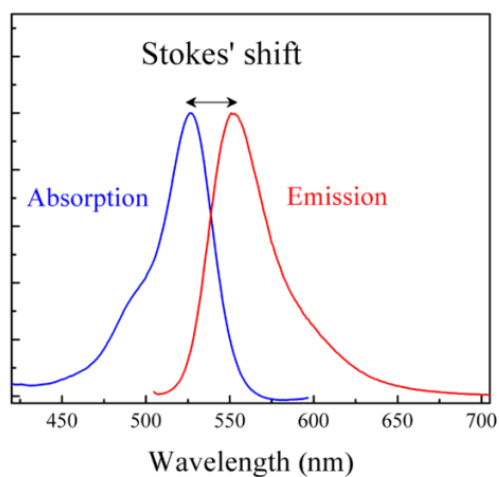


Figure 10: The Stokes Shift

[59]. The wavelength of the molecule is determined by the energy emitted during the relaxation, which depends on the distance between the lowest vibrational energy state of the first excited electronic state and the vibrational energy state of the ground electronic state to which the molecule relaxes, providing a range of potential emitted fluorescent light wavelengths [59]. Because the energy radiated by the photon is less than the energy originally absorbed by the molecule, the photon emitted will have a longer wavelength than the photon absorbed, known as a Stokes' shift (Figure 10) [59].

state, a process known as internal conversion [59]. Once it is in the lowest vibrational energy state of the first excited electronic state, it will relax back to the ground state; if the molecule emits a photon during this relaxation, the process is known as fluorescence

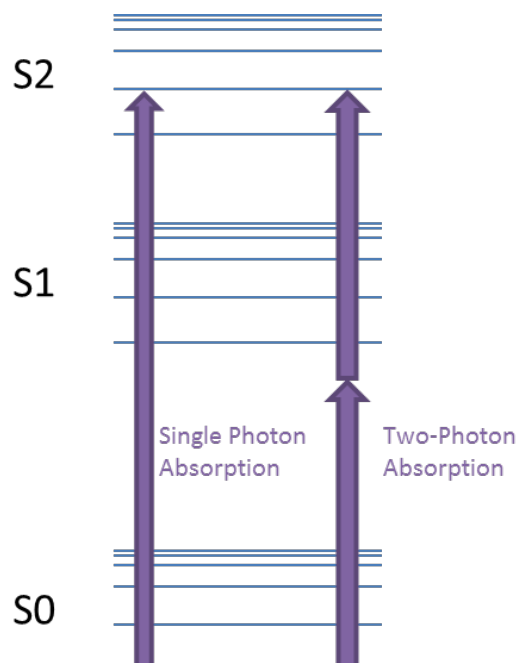


Figure 11: Two-photon absorption

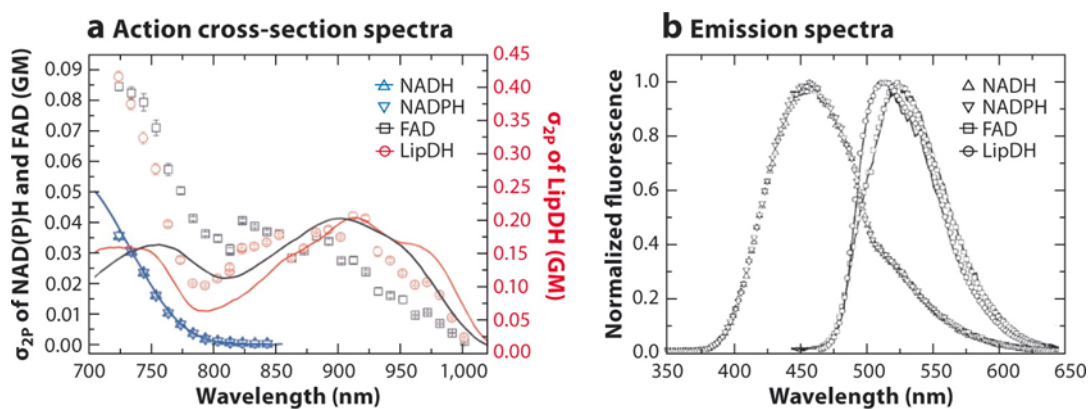
Two-photon excited fluorescence (TPEF) is a non-linear optical process that can be utilized for microscopic imaging. TPEF occurs when two photons of half the required energy (or approximately twice the wavelength) are simultaneously absorbed by a molecule, exciting it to a higher electronic energy state (Figure 11) [15]. When the molecule radiatively relaxes, it emits a single photon with a wavelength reflecting the energy gap between the excited electronic and ground energy states [15]. TPEF requires a very high photon flux in order to achieve simultaneous absorption of two photons and is therefore implemented using femtosecond pulsed lasers with high maximum intensity but low average intensity focused with a high numerical aperture objective lens [15]. TPEF is utilized for microscopy by raster-scanning the excitation light over a field of view and reconstructing an image from the emission collected at each excited focal volume [15].

Two-photon microscopy has many advantages for imaging live cells. Because the excitation light is confined to the focal volume, this technique provides high axial and lateral spatial resolution relative to traditional fluorescence microscopy and also minimizes photo-bleaching to samples relative to confocal microscopy [15]. Because all of the emission light at a given point is attributable to the single excited focal volume, two-photon microscopy also somewhat simplifies the required instrumentation relative to confocal microscopy by eliminating the need for a pinhole and emitted light de-scanning [15]. Signal-

to-noise ratio is also improved relative to traditional or confocal microscopy because there is a large distance between the excitation and emission light wavelengths [15]. For imaging thick specimens, TPEF allows for greater depth penetration into samples due to reduced scattering at increased excitation wavelengths [15].

2.B.II. TPEF FOR MONITORING CELL METABOLISM USING OPTICAL REDOX RATIOS

While TPEF is frequently used in conjunction with exogenous dyes, it can also provide a non-destructive technique for assessing tissue metabolism via endogenous fluorophores. Notably, mitochondrial coenzymes NADH and FAD




 Georgakoudi I, Quinn KP. 2012. Annu. Rev. Biomed. Eng. 14:351–67

Figure 12: (a) Two-photon absorption spectra of NADH and FAD (b) Fluorescence emission spectra of NADH and FAD; Reproduced from [7]

absorb infrared light and emit fluorescence, while their oxidized and reduced counterparts (NAD and FADH₂) do not (Figure 12). Both NADH and FAD undergo two-photon excitation well in the mid-700nm range, while only FAD

absorbs well above 850nm [7]. NADH and FAD emit fluorescence light with peaks around 460 and 525nm, respectively [7]. By selectively exciting the two fluorophores, it is possible to describe relative fluorescence intensities of the NADH and FAD via an optical redox ratio defined as $(FAD)/(FAD+NADH)$ [7].

Optical redox ratios have been used in a variety of applications to describe cellular metabolic activity. Typically, cell autofluorescence at ~755nm excitation and ~460nm emission is attributed to mitochondrial NADH, while fluorescence at ~860nm excitation and ~525nm emission is attributed to mitochondrial FAD [7]. In healthy cells, higher optical redox ratio, indicating greater FAD relative to NADH, is indicative of highly oxidative metabolic activity, while a lower optical redox ratio, resulting from an increase in NADH relative to FAD, is indicative of enhanced glycolytic activity [7].

In cells subject to various stress conditions, redox ratio changes may be associated with other metabolic modulations. For example, when potassium cyanide is added to cells to block the respiratory chain, NADH builds up relative to FAD, lowering the redox ratio; when the mitochondrial membrane potential is depolarized using carbonyl cyanide 4-(trifluoromethoxy)phenylhydrazone (FCCP), respiratory chain activity increases, increasing FAD concentration relative to NADH thus increasing the redox ratio [7]. Multiple spectroscopic and imaging studies have reported increasing redox ratio in relation to apoptosis [60,

61]. Other studies have tied a decrease in NADH/FAD (or an increased redox ratio) to oxidative stress [62-64].

2.B.III. TWO-PHOTON EXCITED FLUORESCENCE LIFETIME IMAGING

While much TPEF microscopy captures total fluorescence intensity over a fixed integration period, time-resolved fluorescence imaging approaches can yield additional information about molecules. Fluorescence lifetime imaging (FLIM) may be implemented by using time-correlated single photon counting (TCSPC), a

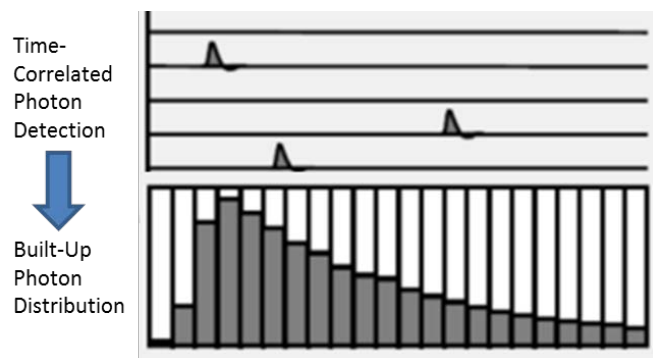


Figure 13: Schematic of time-correlated single photon counting (TCSPC). Modified from [1]

technique which detects individual photons and tracks their emission timing relative to the laser pulse (Figure 13) [65]. TCSPC detects photons over an extended integration period (~1-3 minutes),

allowing for generation of a histogram of photon counts relative to laser pulse timing. The decay profile of this histogram can be quantified to yield information about the fluorophore. For example, NADH has been demonstrated to have multiple distinct fluorescence lifetimes based upon its conformational folding and binding status [66]. Fluorescence lifetimes of ~350 and ~750ps have been reported for stretched and folded free NADH, while lifetimes from ~600-6000ps have been reported for varying species of bound NADH [66-68].

One approach to quantifying NADH fluorescence decay is to fit multiexponential curves to the decay. In this approach, the fluorescence decay curve of each pixel within an image is fit to the following form.

$$F = \sum_{n=1}^n \alpha_n e^{\frac{-t}{\tau_n}}$$

In this expression, n indicates the number of underlying NADH species contributing to the signal, α is the relative weight of that species to the overall decay, and τ is the characteristic time constant of the decay, also known as the fluorescence lifetime [69]. Ratios of component lifetimes or weights may be used to characterize metabolic activity [67, 70]. Typically, an increased concentration in free NADH is associated with glycolytic activity, while increased bound NADH is more associated with oxidative metabolic activity [67].

An alternative approach to analyzing fluorescence lifetime data uses phasor transforms. In this approach, each decay curve is mapped onto a polar plot in frequency space using the following relationships [71].

$$g_{i,j}(\omega) = \int_0^\infty I_{i,j}(t) \cos(\omega t) dt / \int_0^\infty I_{i,j}(t) dt$$

$$s_{i,j}(\omega) = \int_0^\infty I_{i,j}(t) \sin(\omega t) dt / \int_0^\infty I_{i,j}(t) dt$$

In this expression, I is the exponential decay, ω is the laser repetition frequency, (i,j) represent the pixel coordinates, and g and s represent the coordinates in the phasor plot. In the case where the decay is monoexponential, the mathematics simplify as follows.

$$g_{i,j}(\omega) = \frac{1}{1 + (\omega\tau)^2}$$

$$s_{i,j}(\omega) = \frac{\omega\tau}{1 + (\omega\tau)^2}$$

In this case, the phasor transform point will necessarily fall on a “universal circle” within the polar plot, where each position on the circle corresponds to a certain characteristic lifetime [71]. A biexponential decay will be found along a line drawn through its two monoexponential components, while a triexponential decay

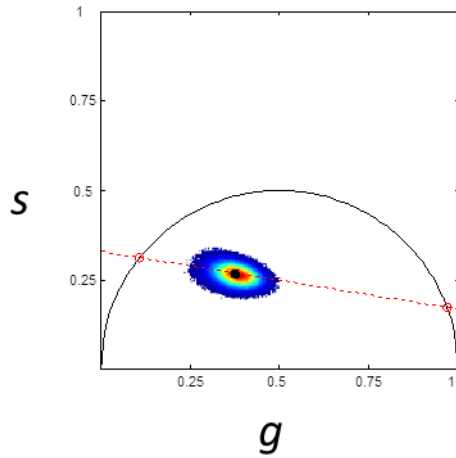


Figure 14: Phasor plot of a biexponential decay

will be found within a triangle drawn between its three monoexponential components (Figure 14) [71]. The phasor transform provides a simple graphical approach for identifying fluorophores with distinct decay profiles present in an image, without requiring any

exponential fitting [71].

2.B.IV. PRIOR STUDIES OF NADH AND FAD AUTOFLUORESCENCE IN BRAIN TISSUE

Many studies of brain tissue autofluorescence have focused on identifying changes associated with neuronal firing, in part to distinguish the metabolic functions of different cell types. Multiple studies in brain slices have reported an initial dip in NADH fluorescence upon neuronal activation, followed by an increase in NADH intensity [72, 73]. Some have cited this phenomenon as evidence for the astrocyte-neuron lactate shuttle, suggesting that the initial dip is due to oxidative neuronal metabolism while the NADH increases co-localize with astrocyte-specific markers, possibly signifying glycolytic lactate production [72]. Others have argued that neurons also give off significant NADH signal surrounding activation, and that there is not yet conclusive evidence for the cell sources of NADH transients, even as they serve as useful signifiers of brain activity [73]. These studies highlight the difficulty of segmenting fluorescence signals in brain slices containing multiple cell types, and the potential utility of controlled cell culture studies for studying the autofluorescence of individual cell types.

NADH and FAD fluorescence have also been utilized in brain tissue spectroscopy and microscopy to characterize metabolic differences in brain regions as well as metabolic responses to stress or disease. In one study of gerbil brain slices, the ratio of FAD to NADH was shown to be higher in

cerebellar/cerebral white matter than gray matter, suggesting increased oxidative energy production in white matter regions [74]. Fluorimetry, *in vivo* two-photon microscopy, and *in vitro* two-photon imaging of brain slices have examined autofluorescence response to oxygen deprivation and seizures [75-78]. A mouse model of Rett syndrome, a neurodevelopmental disorder, showed an increased FAD/NADH redox ratio in brain slices associated with oxidative stress [79]. Optical redox spectroscopy has also been explored as a tool for diagnosing brain cancers [80].

In spite of these diverse studies of NADH and FAD fluorescence in brain tissue, studies of PD or manganese toxicity using NADH and FAD autofluorescence have been limited. One recent study examined changes in NADH and FAD fluorescence lifetime in PC12 cells treated with 1-methyl-4-phenylpyridinium (MPP⁺), a neurotoxin damaging complex I [70]. This study reported a decrease in both NADH and FAD fluorescence lifetime with increasing doses of MPP⁺, as well as an increase in the ratio of unbound/bound NADH and an increase in the ratio of bound/unbound FAD [70]. The authors argue that this alteration indicates a shift towards glycolytic metabolic activity as more free NADH is present (either as a result of glycolysis or decreased complex I activity), and more bound FAD is present, which they attribute to a failure of the TCA cycle to regenerate FADH₂ [70]. While this article establishes the utility of NADH and FAD autofluorescence in probing metabolic changes in PD models,

further research is required to clearly establish relationships between autofluorescence, metabolism, and neurodegeneration across cell types and disease models.

2.B.V. ANALYSIS OF MITOCHONDRIAL ORGANIZATION USING NADH AUTOFLUORESCENCE

In addition to being used as a metabolic marker, NADH fluorescence provides endogenous contrast for characterizing cellular mitochondrial organization. Multiple studies have quantified mitochondrial organization by using a fourier-transform-based approach to quantify intracellular fractal patterns [81, 82]. In this approach, the squared amplitude of the fourier transform of an image, also known as the power spectral density (PSD) function, is first calculated [81]. In images with fractal features, the PSD as a function of frequency typically exhibits a negative power law dependence (i.e. $a^{-\beta}$) [81]. The value of the power law exponent (β) can be used to characterize the degree of clustering in an image, with higher β corresponding to more clustering of fractal features [81]. Artifacts due to cell edge and nuclear border effects may be eliminated by masking the image to only include cytoplasmic features, and by then applying a digital object cloning method to fill the field with the fractal features [81]. This approach has successfully identified cancer-related changes in mitochondrial organization in engineered healthy and cancerous skin tissue [82]. We will use it in a novel application to detect mitochondrial changes in healthy and diseased brain cells.

2.C. CHARACTERIZING ASTROCYTE AND NEURON METABOLISM USING TPEF – MONOCULTURES, CO-CULTURES, AND MANGANESE TOXICITY

2.C.1 INTRODUCTION

Astrocytes and neurons are known to have distinct metabolic profiles, with astrocytes preferring glycolytic metabolism, and neurons favoring oxidative phosphorylation [8]. The two cell types are known to participate in metabolic coupling *in vivo* in order to meet the high energy demands of cell signaling [31]. Astrocytes and neurons are also known to experience oxidative stress and undergo apoptosis when exposed to excessive quantities of manganese [39]. Astrocytes are less impacted by manganese than neurons, however toxicity may alter cell-cell coupling [39].

In this set of experiments, we sought to optimize two-photon excited fluorescence imaging methods and establish quantitative analysis metrics to characterize primary embryonic rat neuron and astrocyte metabolism in two-dimensional, *in vitro* cultures. We hypothesized that TPEF could capture redox and mitochondrial organization differences between astrocytes and neurons consistent with their known metabolic distinctions. We also hypothesized that autofluorescence changes assessed via TPEF could reflect cell responses to manganese poisoning. Finally, we hypothesized that imaging autofluorescence of co-cultured cells could reveal evidence of metabolic coupling and possibly alterations in metabolic responses to manganese.

Initially, we compared optical redox ratios, mitochondrial clustering, and fluorescence lifetime between neurons and astrocytes in monocultures to understand baseline detectable metabolic differences between the cell types, as well as their responses to manganese treatment. Next, we studied three separate co-culture conditions to assess whether interactions between the two cell types result in redox ratio changes evident using our imaging methods. As the first co-culture condition, we cultured astrocytes and neurons on separate glass panes of a “sandwich” co-culture to allow for reciprocal signaling and soluble factor exchange over a 150-200µm distance. As the second condition, we assessed the effect of exchanging conditioned media between the two cell types. Finally, we cultured cell types together in well-plates with one cell type on the bottom glass surface, and the other on a transwell membrane. After characterizing the different metabolic profiles of the two cell types in a range of co-culture conditions, we used redox analysis to assess the metabolic effect of MnCl₂ on cells in co-culture conditions.

2 C.II. MATERIALS AND METHODS

2.c.ii.1. Cell Culture of Primary Embryonic Rat Neurons and Astrocytes

2.c.ii.1.a. Neuron and Astrocyte Monocultures

Neurons were freshly isolated from embryonic day 18 (E18) rat cortices and plated on glass-bottomed petri dishes coated with 0.1 mg/ml poly-d-lysine. Astrocytes previously isolated and expanded from E18 rat cortices were thawed

from frozen and plated on glass-bottomed petri dishes. For emission spectra and TPEF imaging experiments, both cell types were cultured in neurobasal medium, supplemented with 2% B-27, 2% fetal bovine serum, 1% Glutamax, and 1% antibiotic/antimycotic. For excitation spectra experiments, neurons were cultured

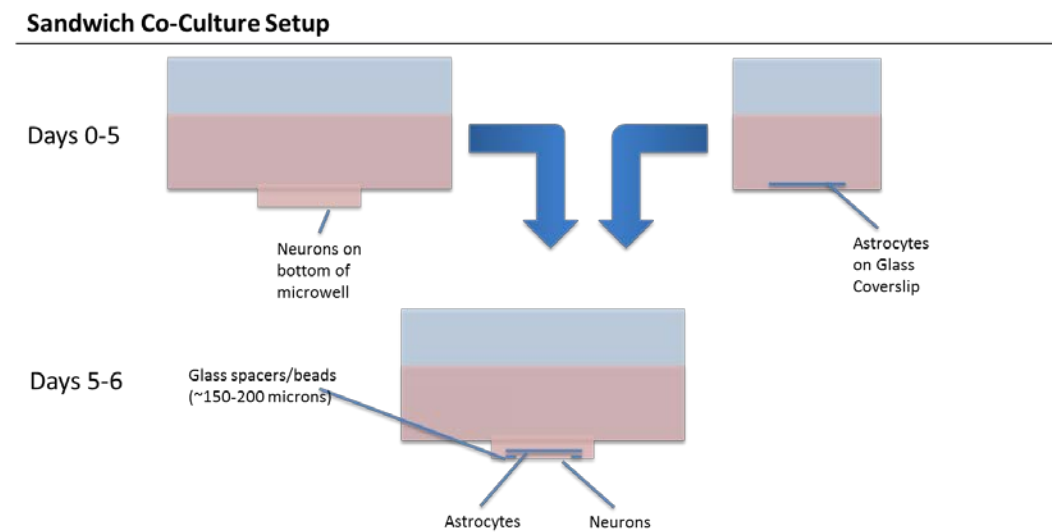


Figure 15: Schematic of the sandwich co-culture setup

in this same media, with FBS excluded, and astrocytes were cultured in media consisting of DMEM-F12, 10% FBS, 1% glutamax, and 1% antibiotic/antimycotic; excitation spectra data analysis corrected for background differences between the media types (See Data Analysis Section). Neurons were allowed to grow for at least 5 days prior to imaging to allow for neurite growth and network formation. Astrocytes were allowed to grow at least 3 days, imaging cells at least 50% confluent. Media was changed every 2-3 days, with the final change 24 hours prior to imaging. 20 mM HEPES was added to the media prior to imaging to buffer against changes in CO₂ levels.

2.c.ii.1.b. Sandwich Co-Cultures

Neurons were seeded as described for monocultures, while E18 astrocytes were thawed from frozen and plated on sterile 12mm glass coverslips. Both cell types were allowed to grow for at least 5 days in neurobasal medium, supplemented with 2% B-27, 2% fetal bovine serum, 1% Glutamax, and 1% antibiotic/antimycotic. Media was changed every 2-3 days. 24 hours prior to imaging, media was aspirated from the neuron cultures, and a small amount of sterile 150-200 micron glass beads were added as spacers to the cultures. The astrocyte coverslips were added to the neuron monocultures, such that the astrocytes and neurons were facing one another, spaced by the beads (Figure 15). 20 mM HEPES was added to the media prior to imaging to buffer against changes in CO₂ levels. The sandwich co-culture experiments typically contained a

Transwell Co-Culture Setup

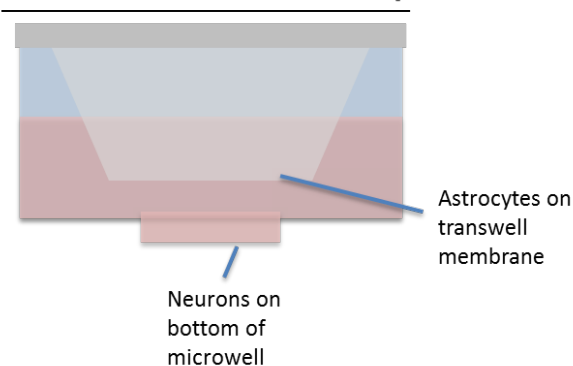


Figure 16: Schematic of transwell co-culture used to image neurons; the opposite cell type arrangement was used to image astrocytes.

monoculture group as well as a control for the co-culture group. To generate the “control for co-culture” condition, neurons and astrocytes were each plated on both glass-bottomed petri dishes and glass coverslips, and sandwich cultures were

assembled as previously described with either only astrocytes, or only neurons.

2.c.ii.1.c Transwell Co-cultures

Neurons and astrocytes were plated in glass-bottomed well plates as described for monocultures. Cells were either grown as monocultures with no transwell insert, or as co-cultures with a transwell insert containing the opposite cell type (Figure 16). Cells were cultured in transwells with the same coating and plating procedures described for monocultures. Only the cells plated on glass were imaged, due to strong fluorescence of the transwell inserts.

2.c.ii.1.d Media conditioning

Neuron and astrocyte monocultures were prepared as described above. Media was changed 2-3 days prior to imaging. At 24 hours prior to imaging, media conditioned on astrocytes or neuron monocultures for 1-2 days was extracted from the cultures and reserved. Astrocyte and neuron monocultures were then either treated with astrocyte-conditioned media, neuron-conditioned media, or fresh media for the 24 hours prior to imaging.

2.c.ii.1.e. Manganese Treatment

Aqueous stock solutions of MnCl_2 were prepared fresh and sterile-filtered. MnCl_2 solution was added to cell culture media for final concentrations of 100, 250, 500, 750, or 1000 μM Mn 24 hours prior to imaging. Stock solutions were sufficiently concentrated that the MnCl_2 solution comprised $\leq 5\%$ of the total volume of the culture medium added to cells. The untreated cell culture media

was determined to have $<0.1\mu\text{M}$ Mn based on inductively coupled plasma mass spectroscopy.

2.c.ii.2. Caspase-3 Assay

Caspase-3 content of Mn-treated cells was determined using a colorimetric assay (R&D Systems) as described in the manufacturer's protocol. In brief, cells were cultured in well plates and 24 hours prior to performing the assay, cells were given either fresh media or fresh media supplemented with $500\mu\text{M}$ (neurons) or $1000\mu\text{M}$ (astrocytes) MnCl_2 . The cells were lysed, centrifuged, and the supernatant was collected for analysis. The caspase-3 colorimetric substrate and reaction buffer were added to supernatant samples and blank samples. Samples were incubated for 2 hours, and the colorimetric change was quantified using a plate reader by measuring absorbance at 405nm. The blank sample values were subtracted from control and Mn-treated sample values to provide corrected absorbance values. N=3-4 cell lysate samples were evaluated per experimental condition.

2.c.ii.3. Two-photon Imaging of Primary Cultures

2.c.ii.3.a. Excitation and Emission spectra

Emission and excitation spectra were taken using a Leica SP2 confocal microscope fitted with a Ti:Sapphire laser. For emission spectra, light was focused to the sample using a 63x water-immersion objective (NA 1.2), and neutral density filters were used to achieve a power of 20-30 mW at the stage.

Images were 512x512 pixels, representing a 238x238 micron field of view. Cells were excited at 755 and 860nm, and fluorescence images were acquired using a photomultiplier tube (PMT) centered at wavelengths 400-700nm with a bandwidth of 20nm in 20 steps. Multiple spectra were taken for each cell type to verify spectral shape, and $n=3$ spectra were averaged to give the final reported spectra for each group.

For the excitation spectra, light was focused to the sample using a 40x water-immersion objective (NA 1.1), and neutral density filters were used to achieve a power of 20-30 mW at the stage. Images were 512x512 pixels, with the zoom feature of the software employed to achieve a 187x187 micron field of view. For excitation spectra, cells were excited at wavelengths ranging from 720-900nm (steps of 10 nm), and fluorescence images were formed using non-descanned detectors filtered to collect light at 460 \pm 20nm and 525 \pm 25nm. Multiple spectra were taken for each cell type to verify spectral shape, and $n=2-3$ spectra were averaged to give the final reported spectra for each group

2.c.ii.3.b. Imaging for Optical Redox Ratio Analysis

Redox images were taken with a Leica SP2 confocal microscope fitted with a Ti:Sapphire laser. Laser light was focused to the sample using a 40x water-immersion objective (NA 1.1), and neutral density filters were used to achieve a power of 20-25 mW at the stage. Samples were excited with light at 755nm and 860nm and fluorescence images were formed using non-descanned detectors

filtered to collect light at 460 +/- 20nm and 525 +/- 25nm. Images were 512x512 pixels, with the zoom feature of the built-in Leica Control software employed to achieve a 187x187 micron field of view. Images were formed based on an average of 12 scans. 3-6 non-overlapping images were taken per petri dish or well, and n=3 dishes or wells were imaged per cell type and treatment condition. The one exception to this sampling regime was the 500uM MnCl₂ monoculture group in the sandwich co-culture experiment. In this case, n=2 dishes were imaged due to contamination of the 3rd dish, however additional images were taken in each of the unaffected dishes to yield a consistent number of images taken across conditions. Redox and mitochondrial organization results from monocultures reflect 9 independent experiments. Redox and mitochondrial organization results from Mn-treated monocultures reflect 2 independent experiments. Sandwich co-culture and media conditioning redox results reflect 2 independent experiments. Transwell and Mn-treated sandwich co-culture results each reflect 1 experiment.

2.c.ii.3.c. Fluorescence Lifetime Imaging

Fluorescence lifetime images were taken using a custom-built two-photon microscope fitted with a Ti:Sapphire laser. Light was focused to the sample using a 40x water immersion objective (NA 1.1), and a half-wave plate was adjusted to achieve a power of 20 mW at the stage. Samples were excited with light at 755nm and collected using a PMT centered at 460nm +/- 20nm. Time-correlated single photon counting (TCPSC) was employed obtain time-resolved fluorescence decay

information. Images were 512x512 pixels, representing a 184x184 micron field of view, and were acquired over a 70s integration time. A calibration image of umbelliferone (7-hydroxycoumarin) was taken for each experimental day and showed the characteristic mean lifetime of 5.1ns. For the cell samples, 4-6 non-overlapping images were taken per petri dish and n=3 petri dishes were imaged per group.

2.c.ii.4. Data Analysis

2.c.ii.4.a. Spectral Analysis & Corrections

Emission spectra for each cell type were obtained by determining the average fluorescence intensity of images acquired at each emission wavelength. Because we observed unexpected and large intensity increases in the upper collection wavelengths for spectra taken at 755nm excitation, these spectra were then corrected for scattered excitation light. We took spectra of a strongly scattering sample at 755nm excitation using the same parameters used for the cells. We observed that subtracting a scaled version of this scattering spectrum

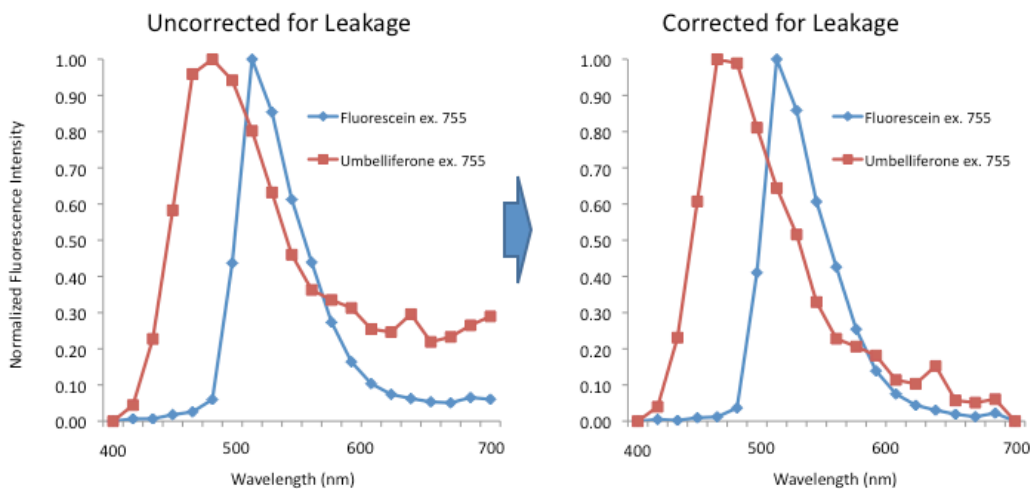


Figure 17: Scattering correction on reference dye emission spectra

from emission spectra of standard dyes such as fluorescein and umbelliferone produced their expected intensity peaks (Figure 17), and we therefore applied the same correction to the cell spectra. We assumed that all of the cell signal at 700nm was a result of scattered excitation light and therefore scaled the scattering sample spectrum to range from the minimum value of the cell spectrum to the value at 700nm. This scaled scattering sample spectrum was subtracted from the cell spectrum to remove the intensity contribution of scattered light. The spectra were then scaled between 0 and 100% (Figure 18). To assess the relative contributions of NADH and FAD to the emission spectra taken at 755nm and 860nm excitation, we used an NADH reference spectrum to un-mix our experimental spectra into two components using non-negative matrix factorization. The factorization was performed 100 times per image and the best-fit result was recorded, giving the weights of the fixed components yielding the

best fit to the experimental data.

Cell excitation spectra were also obtained by first determining average fluorescence intensity of images taken at each excitation wavelength. Because background intensity appeared to vary significantly with excitation wavelength, we took spectra of cell culture media and subtracted the average value at each excitation wavelength from the cell spectra. Because excitation power varied slightly by wavelength, we then also normalized the average intensity at each wavelength by the inverse square of the power delivered to the sample at that wavelength. Finally, to account for other instrumental wavelength variability, we took an excitation spectrum of fluorescein and determined a correction factor for each excitation wavelength to match reference values for the two-photon absorption spectrum of fluorescein (Figure 20) [10]. We applied these correction factors to our excitation spectra and normalized the spectra to a maximum of

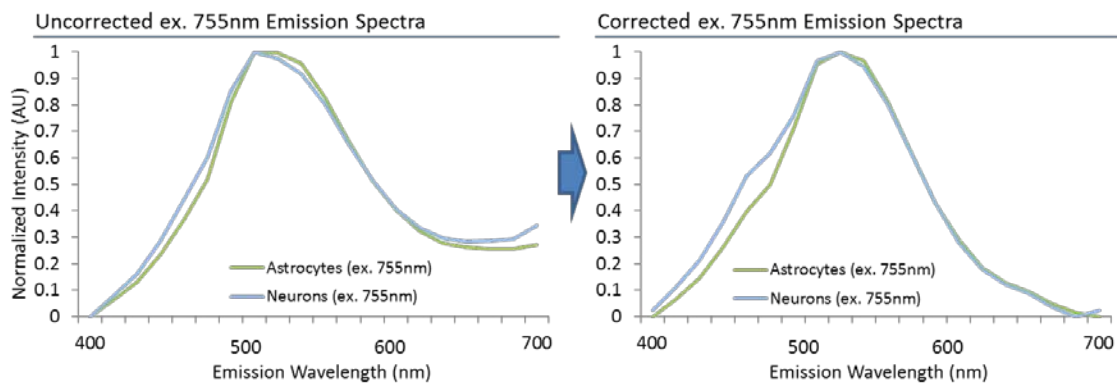


Figure 18: Cell excitation spectra before and after corrections

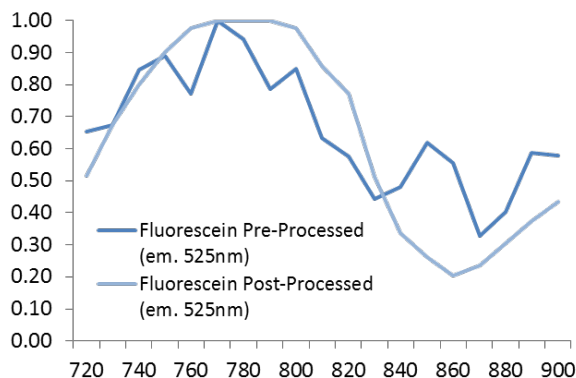


Figure 20: Fluorescein excitation spectrum pre-and post-corrections

100% (Figure 19).

2.c.ii.4.b. Redox Ratio Analysis

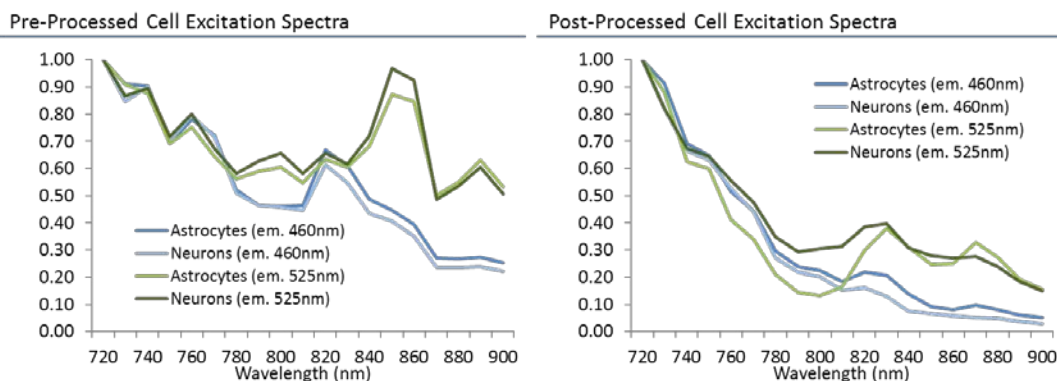
For redox analysis, images were processed in several steps. For a given field, the multiple corresponding images (e.g., different excitation and emission

wavelengths) were spatially co-

registered by determining the shift

producing the maximum correlation between channels. We corrected for the intensity contribution of background fluorescence by identifying and subtracting the mode of the low-intensity pixels, defined as having intensity less than an 8-bit integer value of 30. A cell mask was determined through several steps. First, we separately applied a Gaussian low-pass filter (3x3 pixels, 1.5 pixel standard deviation) to the NADH (ex. 755, em. 460) and FAD (ex. 860, em. 525) images to

Figure 19: Cell excitation spectra before and after corrections



slightly smooth the images and remove isolated, high-intensity background pixels. Next, we transformed the intensity of each image by raising it to a power of 1.75, in order to further separate high and low-intensity pixels for adaptive thresholding. We then used the Matlab `multithresh` function to generate two adaptive, intensity-based thresholds for each image based on the Otsu method. The `multithresh` function allows the user to input the number of thresholds that should be used to segment an image; threshold levels are chosen which minimize the variation within the groups that they delineate. Because the NADH channel included separate moderate and high-intensity pixel populations within cells, we used the lower of the two `multithresh` thresholds to mask the NADH image so that background pixels were excluded. We generated an FAD mask by applying the higher of its two intensity thresholds because cell pixels in this channel were more uniformly high-intensity and utilizing the lower of the two thresholds resulted in inclusion of significant background regions. The masks for the two separate channels were then combined through addition to generate an overall cell mask including all of the pixels included in either the NADH or FAD masks, and the Matlab `bwareaopen` function was applied to remove small objects with fewer than 50 connected pixels. Individual image channels were normalized to account for differences in gain and power between channels. We then removed saturated pixels and pixels not attributable to FAD or NADH fluorescence (e.g., with significant fluorescence in the ex. 860, em. 460 channel) from the mask. Pixel-

wise redox ratios were calculated by taking a ratio of the normalized but spatially unfiltered FAD intensity to FAD + NADH intensity.

Redox ratio histograms were generated by applying a spatial Gaussian low-pass filter (3x3 pixels with 0.5 pixel standard deviation) to the initial unfiltered redox maps in order to reduce the effects of minor co-registration issues and noisy data. The cell mask was then applied to the spatially filtered redox map and redox ratio values within the mask were used to generate histograms with 50 bins between redox ratio values of 0 and 1. Overall redox ratio histograms for treatment groups in a given experiment were generated by summing the bin counts for individual images and normalizing the resulting histogram so that the sum across all bins added up to 100%. In summary histograms displaying data from multiple experiments, the individual experiments were given equal weight and the resulting histogram was normalized to sum to 100%.

To determine the basis redox ratio components for the redox histograms, we first compiled all of masked, spatially filtered redox ratio pixels from astrocyte and neuron monoculture images. This data represented >250 images across 9 experiments, each containing n=3 separate cultures of each astrocytes and neurons. To determine the contributing Gaussian components to the redox histograms, we used the `gmdistribution.fit` function within Matlab to fit a 3-component Gaussian mixed model to the aggregate. The fitting was performed 10 times, and the mean and standard deviations of the three components from each fit

were averaged across the 10 iterations. Resulting components were similar to results obtained when un-mixing the aggregate neuron or astrocyte data separately.

We then determined the image-by-image relative weights of the redox basis components. We simulated the distributions of the basis components to obtain histograms with 50 bins and values between 0 and 1. We normalized these components to range from 0 to 100% and then used them as fixed components to fit to individual image histograms, yielding best-fit component weights for the experimental data. For each image, we normalized the weights of the three basis components to add up to 100%. Ratios of the component weights (i.e., $W1/(W2+W3)$, $W2/(W1+W3)$, and $W3/(W1+W2)$) were used to quantify and statistically test changes in the redox histograms.

Redox ratio maps in the results were generated by spatially filtering the raw redox ratio maps using a Gaussian low-pass filter (5x5 pixels with 0.55 standard deviation), assigning colors to each pixel based on redox ratio, and modulating intensity based upon average intensity of the normalized NADH and FAD channels. Redox ratio tri-colored component maps were assembled by first spatially filtering the raw redox ratio maps using the same Gaussian low-pass filter used for the redox histograms (3x3 pixels with 0.5 standard deviation). Next, pixels were assigned one of three colors based on where they fell relative to the

midpoints between the centers of the three unmixed redox components. Finally, the cell mask was used to exclude pixels not within the cell bodies.

2.c.ii.4.c. Mitochondrial Organization Analysis

Mitochondrial organization analysis was performed on a masked version of the normalized NADH channel. We used the same mask and normalization process described in the previous section, and applied an additional intensity threshold to the NADH channel to filter out very intense objects that were likely to produce artifacts in the PSD analysis. The rest of the analysis methods follow the approach previously published [81, 82]. In brief, the masked image was clone-stamped to eliminate the edge effects of cells. We then performed a Fourier transform, calculated the power spectral density (PSD) function, and determined average values at each frequency through radial sampling. 5 iterations of this process were performed to obtain an average PSD curve. We set a low frequency cutoff value to delineate the part of the curve describing intracellular features; the cutoff value chosen was 0.2 microns^{-1} , corresponding to a conservative maximum expected distance of 5 microns within cells based on neurons, which have smaller cell bodies than astrocytes. The upper frequency cutoff was set where the base-10 logarithm of the PSD value fell to 2% of its maximum. The log/log curve was then fit to an inverse power function to obtain the exponent value β . Neuron and astrocyte intensity and cloned images were slightly contrast-

enhanced using ImageJ (0.4% saturated pixels) for improved visualization in PSD-related figures in the results.

2.c.ii.4.d. Fluorescence Lifetime Analysis

FLIM phasor analysis was performed using custom Matlab software. To account for the instrument response function (IRF), a reference image (i.e., 7-hydroxycoumarin) was first transformed into phasor space, and correction matrices were calculated to determine the necessary phasor rotation and modulation to position the reference phasor on the unit circle according to its known lifetime (i.e. 5.1ns). For a given group of images to be analyzed (e.g., neurons with and without manganese), we formed an aggregated phasor plot to determine a standard curve for calculating bound fraction. To form this aggregate plot, we determined first a cell mask for each individual image by applying a low-pass Gaussian spatial filter (3x3 pixels, 1.5 pixel standard deviation) to the data, using Matlab's `multithresh` function to generate two intensity-based thresholds for the filtered image, and using the lower of the two intensity thresholds to binarize the image. We then calculated the IRF-corrected phasor coordinates (g,s) for each pixel within the mask. These pixels were aggregated across images and plotted on an overall phasor plot. When the distribution was confirmed to fall on a single trajectory, a line was fit to the data in order to determine the "standard curve." To determine individual images' bound fraction values, their average phasor (g,s) values were calculated and projected onto the standard curve. Bound fraction was

defined as the distance between the projected point and the standard curve's short-lifetime intersection with the circle, divided by the length of the standard curve within the circle. To obtain bound fraction standard deviation values for individual images, we projected each masked pixel's phasor coordinates (g,s) to the standard curve and calculated pixelwise bound fractions and determined the bound fraction standard deviation for pixels with non-zero bound fraction values. To obtain false-colored bound fraction images, each pixel's g and s values were projected to the standard curve to calculate pixel-wise bound fraction values. Pixel color was assigned based on bound fraction and intensity was modulated to reflect the pixel's intensity value.

2.c.ii.5. Statistics

Statistical software (JMP) was used to evaluate differences in means of various image metrics (e.g., redox ratio component weight ratios, β) between groups with certain fixed effects (e.g., cell type, Mn treatment). First, image-wise values were split by group and experiment to identify and exclude outliers (typically <5-10% of data). Outliers were identified as values falling greater than 1.5 times the interquartile range above the 75th quantile of the data, or 1.5 times the interquartile range below the 25th quantile of the data. When the final data set was established, a mixed model was specified, including fixed effects and their interaction effects (where applicable), as well as random effects (e.g., petri dish, experimental day). The model was estimated using a restricted maximum

likelihood (REML) method, and an F-test was used to assess the significance of the fixed effects and their interactions (where applicable). If an effect was significant, a post-hoc Tukey HSD test was applied to determine the significance of differences between individual groups. In cases where the model did not converge due to little variation in a random effect (e.g., experimental day), we determined that the effect could reasonably be excluded from the model and we estimated the revised model as described above. In graphs, error bars indicate standard error, and significance is indicated using asterisks * = $p < 0.05$, ** = $p < 0.01$, *** = $p < 0.001$, NS = not significant at $p < 0.05$ level.

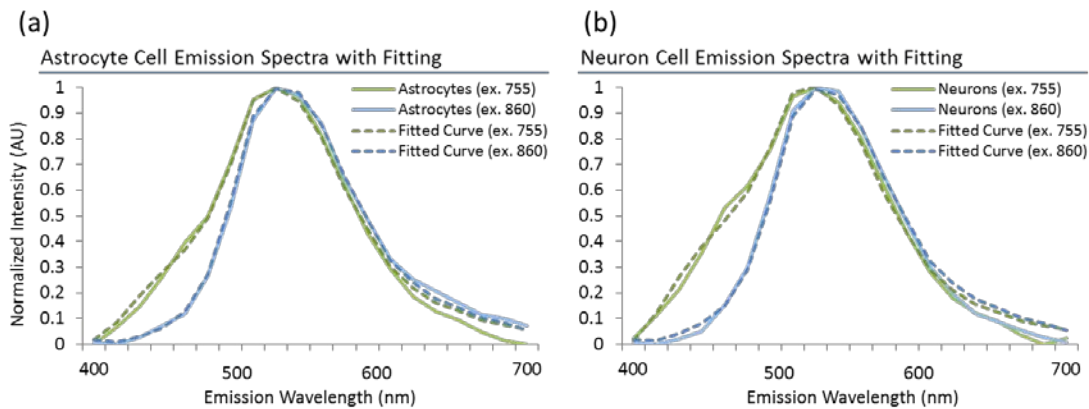


Figure 21 Astrocyte (a) and neuron (b) emission spectra when excited at 755 or 860nm

2.C.III. RESULTS

2.c.iii.1. Excitation and Emission Spectra

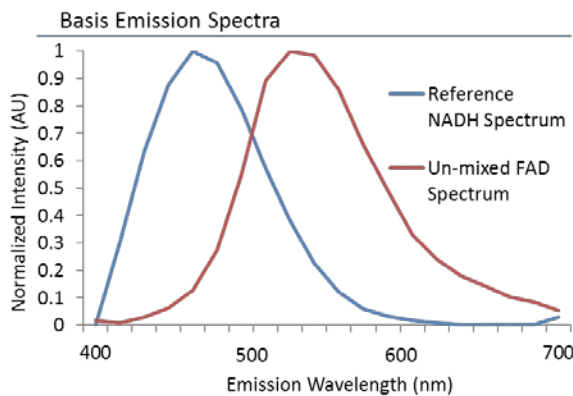


Figure 23 : Basis emission spectra for spectral fitting

We first obtained excitation and emission spectra of astrocytes and neurons in 2D monocultures, to verify that the autofluorescence could be primarily attributed to NADH and FAD. Both the emission and excitation spectra yield the expected fluorescence peaks for NADH and FAD (Figure 21).

At 755nm excitation, we expect both NADH and FAD to fluoresce, reflected by the modulation near 460nm (NADH), and the peak near 550nm (FAD) [7]. At

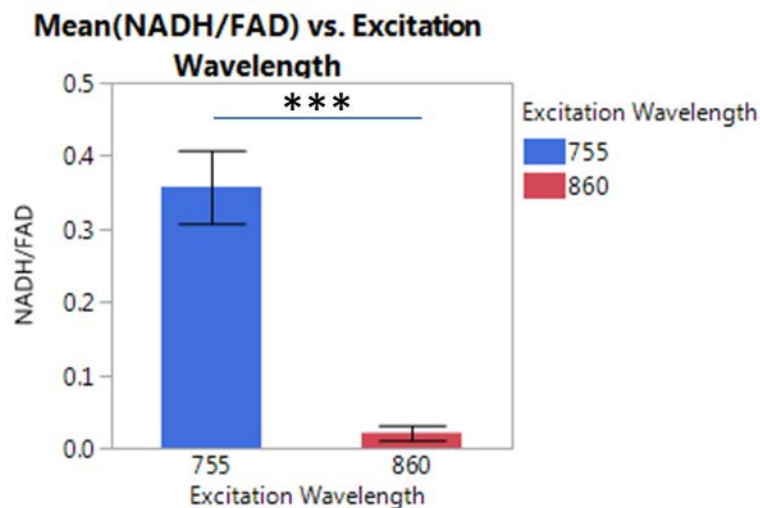


Figure 22: Relative contribution of NADH/FAD at each excitation wavelength based on spectral fitting

860nm, we expect FAD to fluoresce primarily, reflected by the single peak near 550nm [7]. The composition of these spectra are further confirmed by un-mixing with a fixed NADH spectrum to yield the FAD

spectrum shown in Figure 23. After fitting the experimental spectra with these basis components, we compared the fitted relative contributions of NADH and FAD between excitation wavelengths, and demonstrated that the relative contribution of NADH is significantly higher at 755nm than at 860nm, as expected (Figure 22).

In the excitation spectra, we expect fluorescence at 525nm to be primarily attributed to FAD; consistent with published values of FAD's two-photon cross section, the greatest fluorescence intensity is in the mid-700's, with a secondary peak in the 800's [7]. We expect fluorescence near 460nm to be primarily a result of NADH; the excitation spectrum collected at 460nm is consistent with NADH's two-photon absorption in the mid-700's, as evidenced by steep drop-off in signal after the mid 700's (Figure 24) [7].

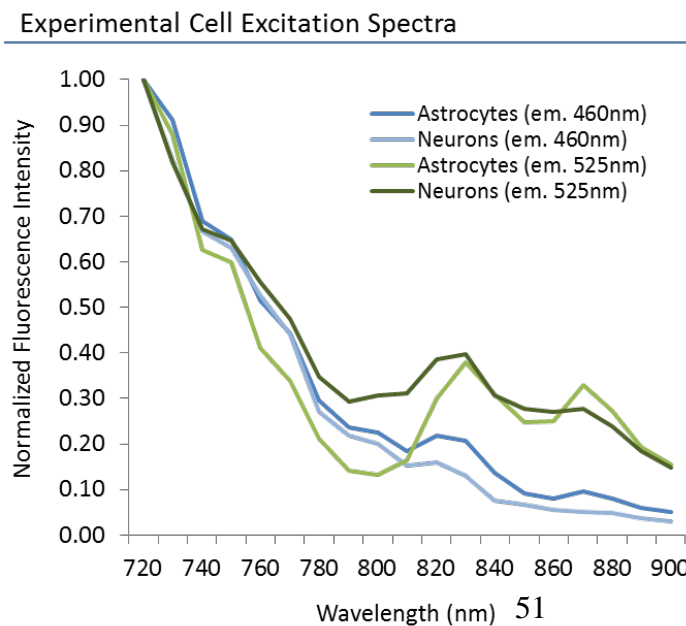


Figure 24: Excitation spectra of astrocytes and neurons relative to the 460nm channel.

2.c.iii.2. Astrocyte and Neuron Monocultures Redox Results

Astrocytes and neurons have distinct morphologies, autofluorescence patterns, and redox ratio distributions (Figure 25 a-b). Astrocytes are characterized by

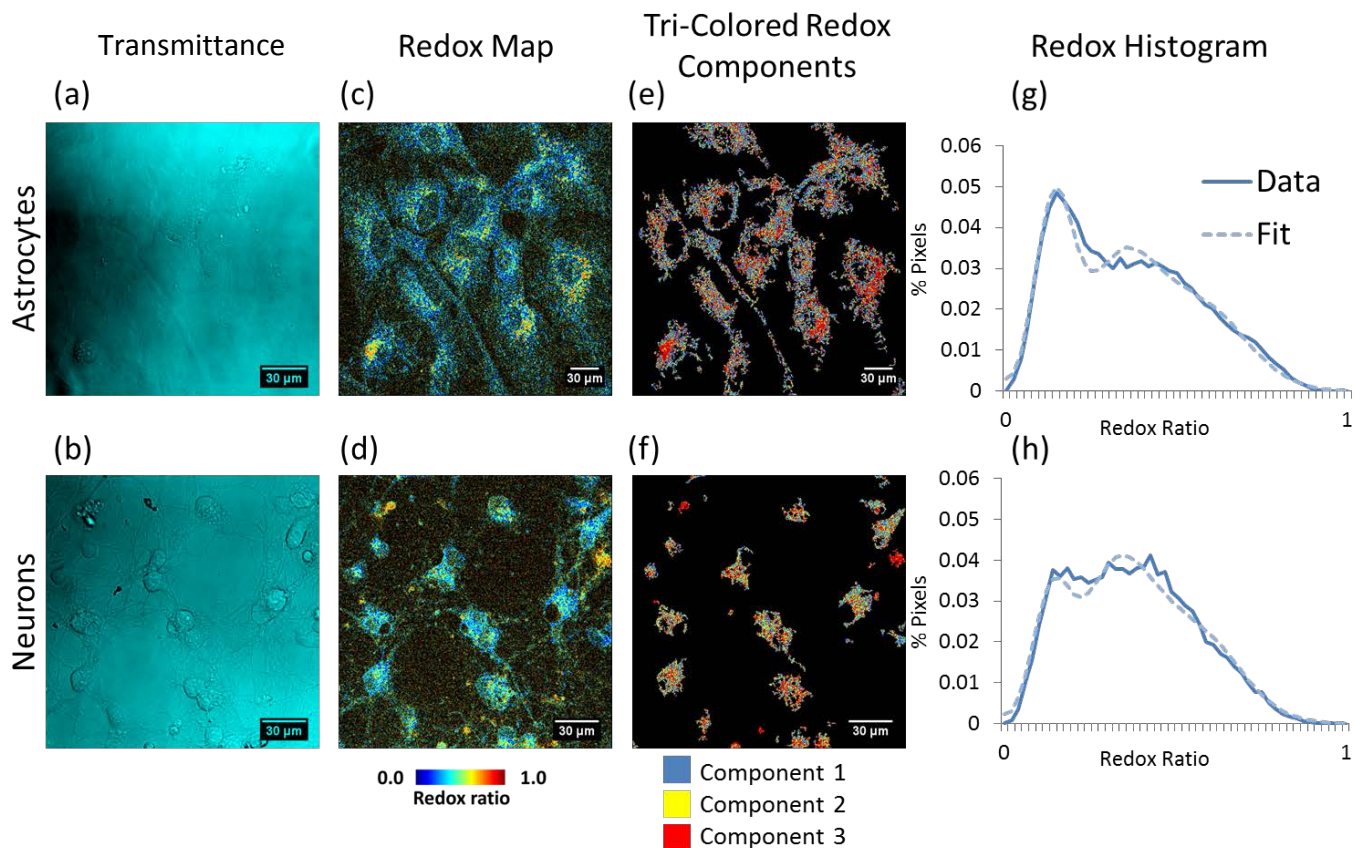


Figure 25 (a-b) Transmission images of astrocyte and neuron morphology (c-d) Redox ratio maps (e-f) False-coloring based on gaussian components (g-h) Redox histograms and fits

large, spread-out cell bodies, while neurons are characterized by smaller cell bodies and highly networked extensions (Figure 25 a-d). The distribution of neuron redox ratios tends to be shifted to the right relative to astrocyte redox ratios, as suggested both by the redox ratio maps (Figure 25 c-d) and the redox histograms (Figure 25g-h) of individual sample images, as well as the collective redox histograms accumulated over several experiments (Figure 27). The

astrocyte and neuron redox distributions may be modeled as a sum of three Gaussian components (Figure 26). When cells are false-colored to spatially

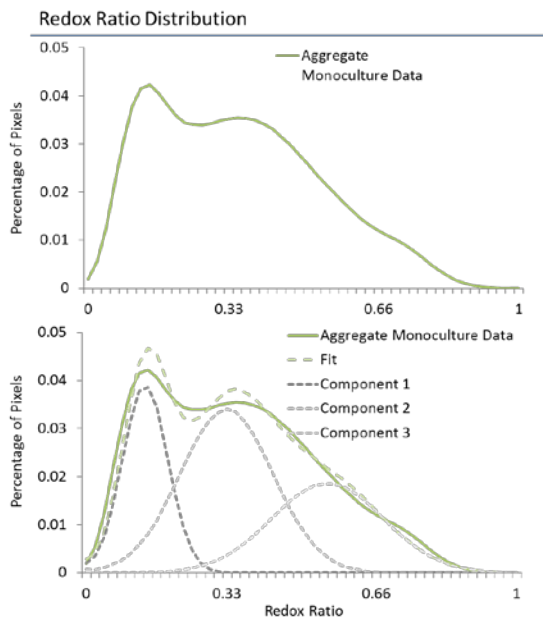


Figure 26: Gaussian components unmixed from aggregate monoculture redox ratio distributions

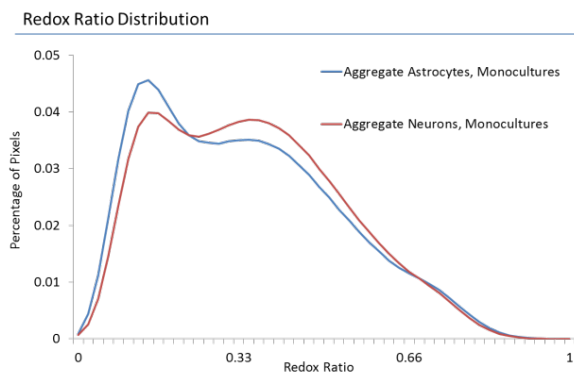


Figure 27: Aggregate redox histograms of neurons and astrocyte monocultures

localize these three components (Figure 25e-f), we note that healthy cells typically contain a combination of the three components, possibly representing contributions of multiple metabolic processes.

When the relative

weights of the three redox ratio components are compared between the groups, we note that astrocytes tend to place the most relative weight on component 1, while neurons place the most relative weight on component 2 (Figure 28), features reflected in the false-colored redox component

images (Figure 25 e-f). When relationships between relative weights are

quantified through ratios, we see that astrocytes have a statistically greater relative weight on component 1 ($W1/(W1+W2)$), while neurons have a statistically greater weight on components 2 ($W2/(W1+W3)$) and 3 ($W3/(W1+W2)$) (Figure 30a-c). If we consider component 1 to represent glycolysis, and components 2 and 3 to represent oxidative processes, these results suggest that neurons and astrocytes have distinct autofluorescence profiles which are consistent with known metabolic differences between the cell types including more oxidative metabolism in neurons vs. astrocytes. However, we also note that component 3 may be associated with some stress to cells; in cases where component 3 dominates an

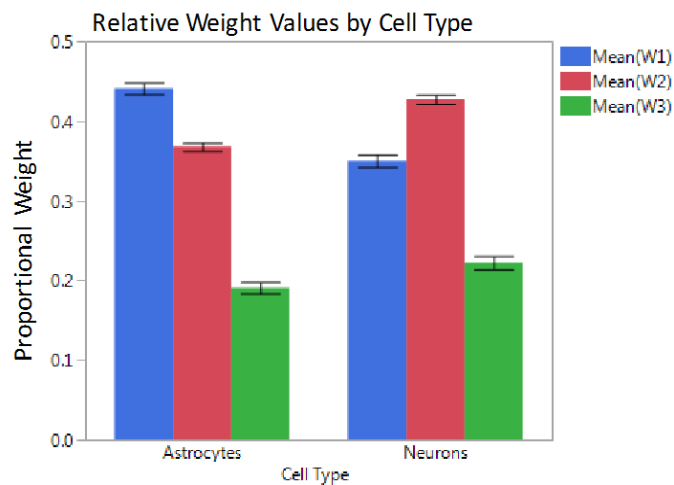


Figure 28 Astrocyte and Neuron relative component weights

entire neuron, it tends to exhibit nuclear blebbing consistent with apoptosis (Figure 29). However, few neurons exhibit these features in healthy monocultures.

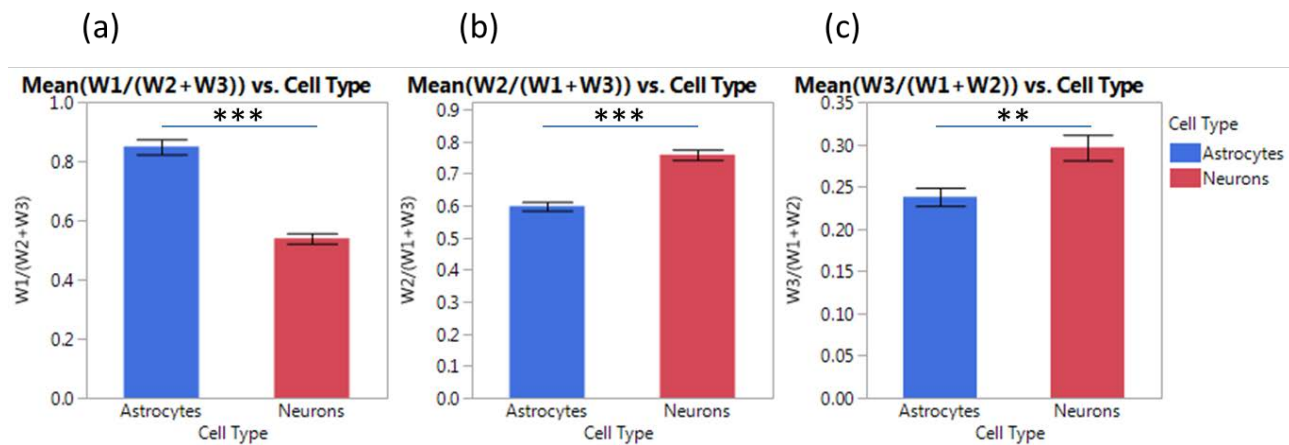


Figure 30: Relative weights of redox Gaussian components for astrocyte and neuron monocultures

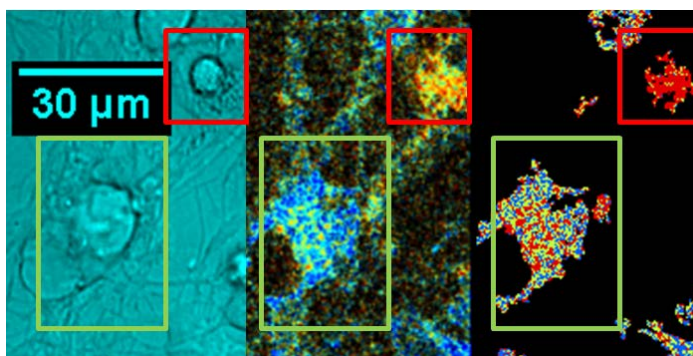


Figure 29: Neurons with normal morphology (green box) exhibit combinations of all three redox ratio components, while neurons with nuclear blebbing and abnormal morphology (red box) have higher redox ratio and are dominated by component 3.

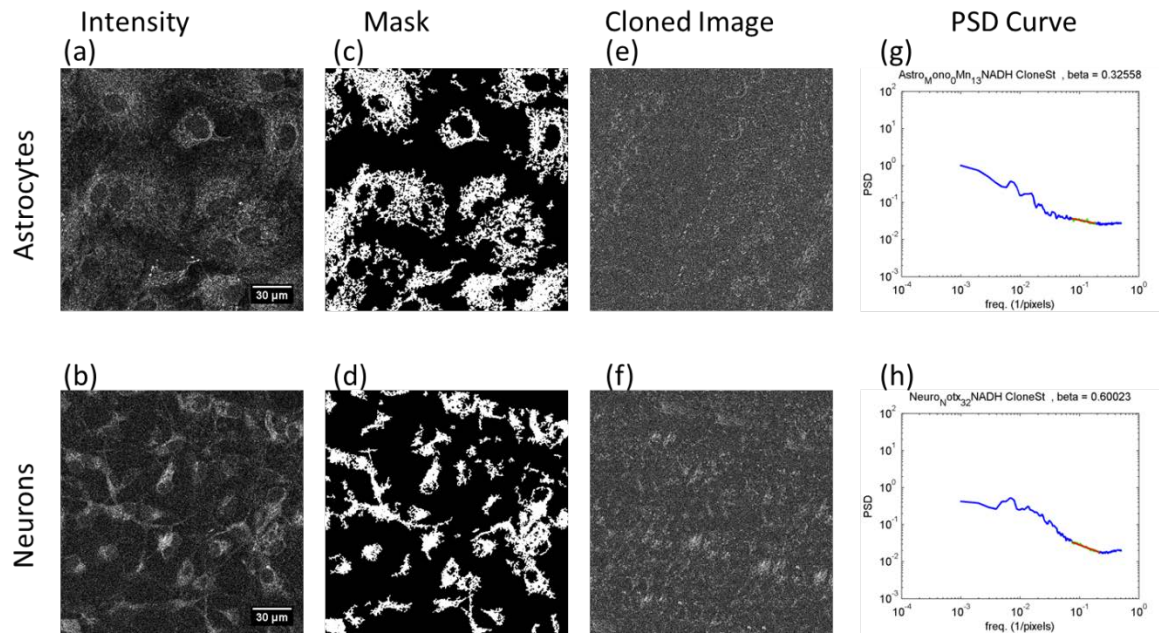


Figure 31: (a-b) NADH intensity (c-d) Masks for PSD analysis (e-f) Cloned images (g-h) PSD curves characterizing mitochondrial organization

2.c.iii.3. Mitochondrial Organization in Monocultures

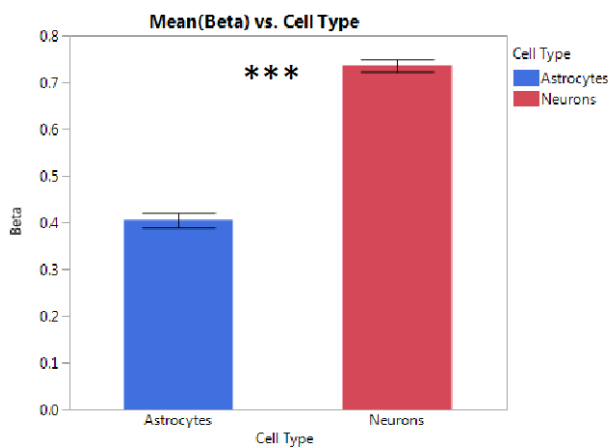


Figure 32: Astrocyte and neuron clustering β values

When comparing mitochondrial organization of the two cell types, neurons have a statistically greater β value than astrocytes (Figure 32). This difference is driven by the more tightly packed mitochondria

within neurons' small cell bodies (Figure 31a-b) relative to astrocytes' more spread out mitochondrial networks. This morphological difference yields larger features in the cloned images (Figure 31e-f), and therefore a steeper PSD curve (Figure 31g-h), yielding a greater average clustering value (β) in neurons vs. astrocytes.

2.c.iii.4. Monoculture FLIM

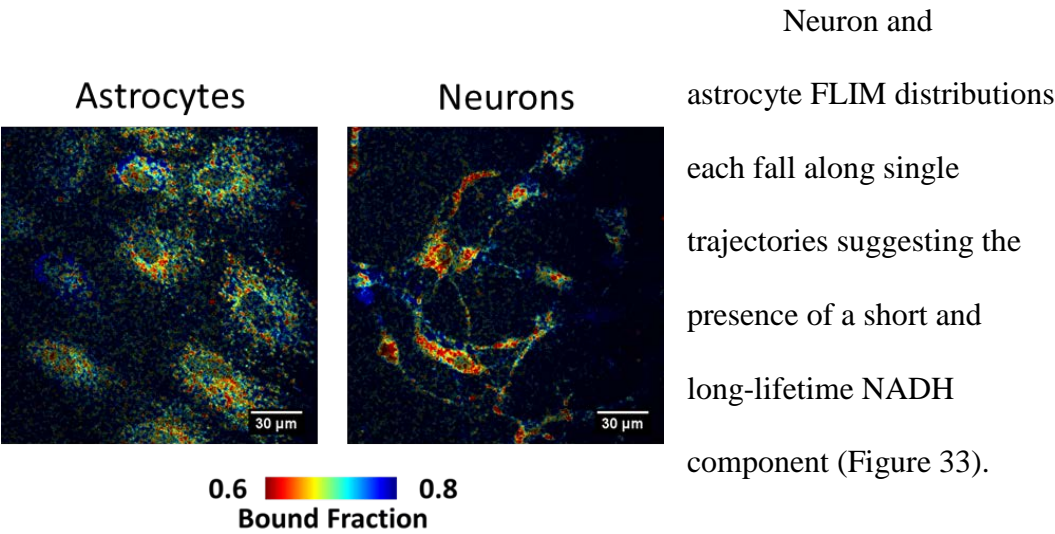


Figure 34: False-colored FLIM images of astrocytes and neurons

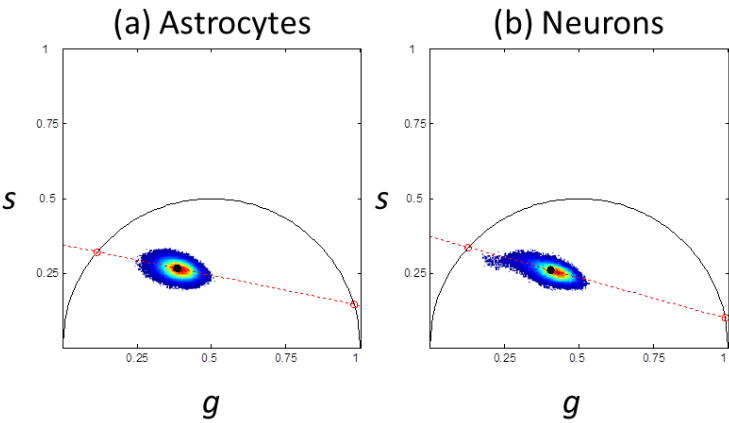


Figure 33: Aggregate phasor plots of astrocytes and neurons

bound fraction than astrocytes (Figure 35).

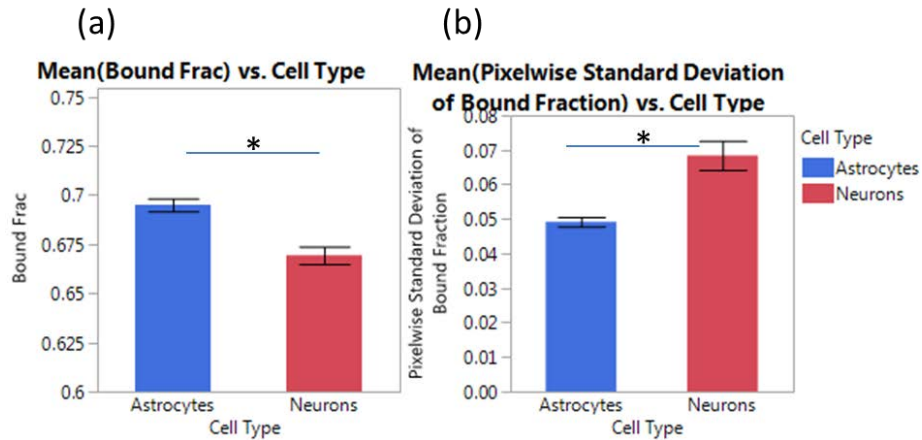


Figure 35: Phasor FLIM metrics of neuron and astrocyte monocultures. (a) Bound fraction (b) Image-wise standard deviation of bound fraction

These results, together with the aggregate phasor plots, suggest that astrocytes may have a higher NADH bound fraction, on average, than neurons, but that neurons have a greater spread in bound fraction values, particularly in the longer-lifetime direction, as suggested by the skewed phasor distribution in Figure 33b.

2.c.iii.5. Effect of Manganese on Monoculture Redox ratios

In the next set of experiments, neurons and astrocytes were exposed to increasing doses of MnCl_2 in order to assess effects on redox ratio distributions. Neurons exposed to increasing doses of MnCl_2 exhibited morphological changes including loss of axons and soma condensation, as

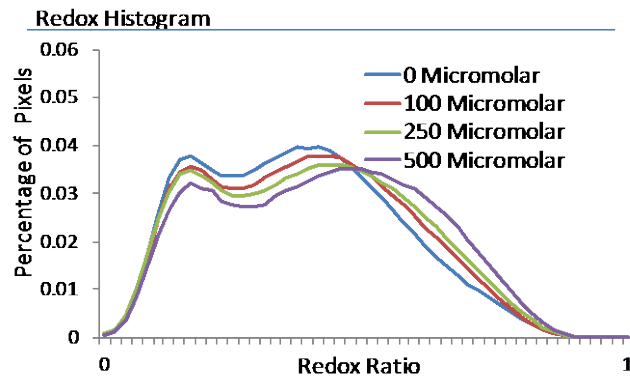


Figure 37 Neuron redox ratio histograms with increasing MnCl_2 dose

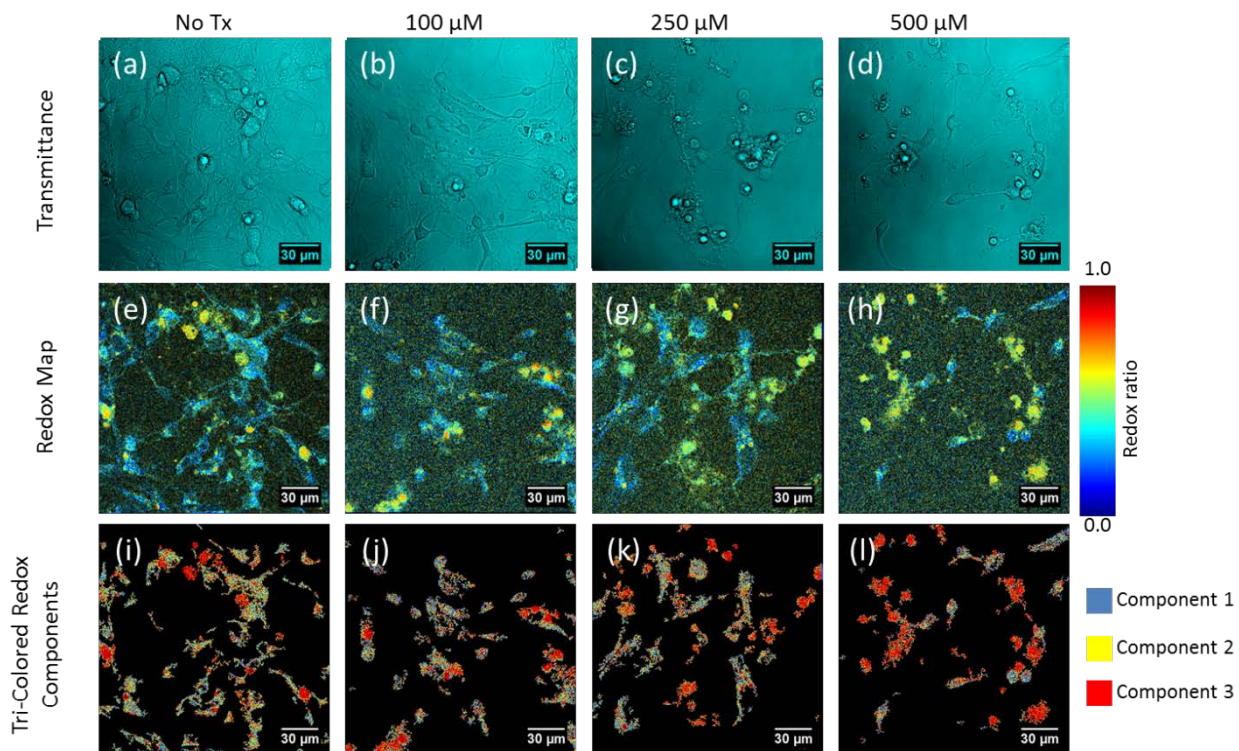


Figure 36 Effects of increasing doses of MnCl_2 on neuron morphology and redox ratio. (a-d) Transmittance images (e-h) Redox ratio maps (i-l) Redox component maps

visualized in transmittance images (Figure 36a-d). Redox ratios generally increased (Figure 36e-h), while cells also transitioned from having a mixture of redox ratio components to exhibiting primarily component 3 (Figure 36i-l). Cells with altered morphology tend to also exhibit this redox ratio shift. A dose-dependent shift in redox ratio distributions is reflected in aggregate redox histograms (Figure 37).

When examining the relative component weights, we see a dose-dependent decrease in the relative weight of component 2, and a dose-dependent increase in the relative weight of component 3 (Figure 38).

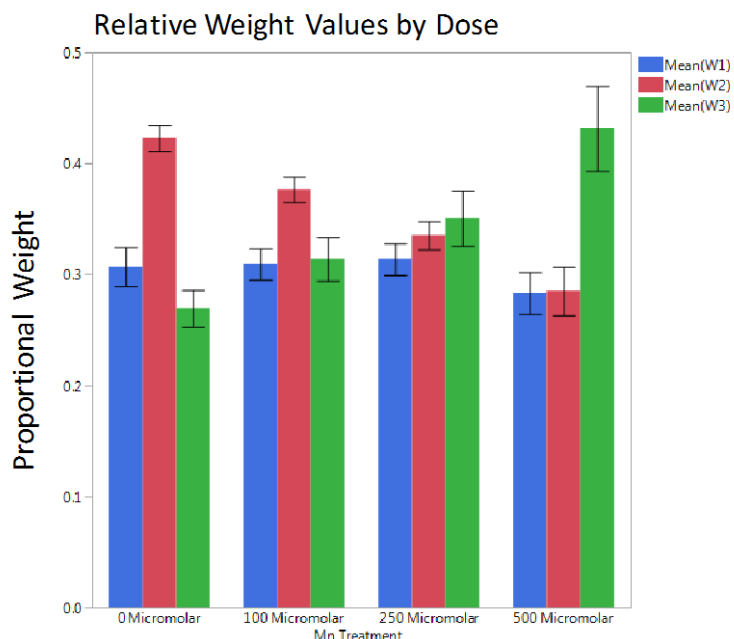


Figure 38: When treated with increasing doses of MnCl_2 , neurons display a drop in weight of component 2, and increases in weight of component 3.

This shift is represented quantitatively by the statistically significant decrease in $W2/(W1+W3)$ between 0 and 500 μM and statistically significant increase in $W3/(W1+W2)$ between 0 and 500 μM (Figure 40a-c). $W1/(W2+W3)$ does not change significantly.

These results, in concert with the altered cell morphology, suggest that decreases in component 2 may be evidence of impaired healthy oxidative metabolism in neurons treated with manganese, and that increases in component 3 may be associated with oxidative stress and apoptosis. Increased apoptosis is further supported by increased caspase-3 activity upon MnCl_2 treatment (Figure 39).

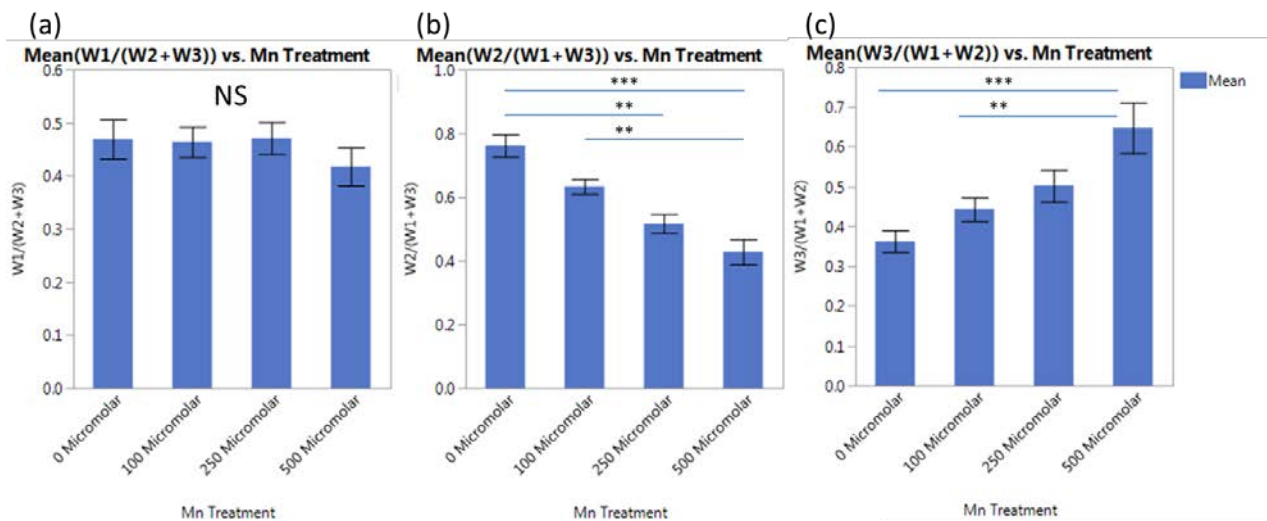


Figure 40: Relative weights redox ratio components in Mn-treated neuron monocultures (a) $W1/(W2+W3)$ (b) $W2/(W1+W3)$ (c) $W3/(W1+W2)$

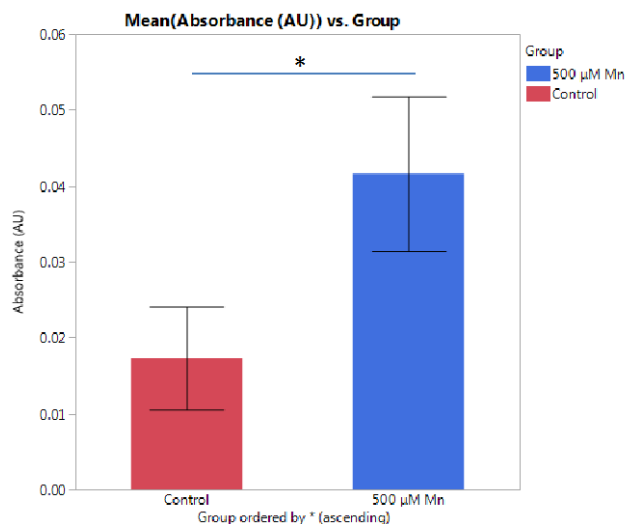


Figure 39: Caspase-3 assay in control vs. Mn-treated neurons

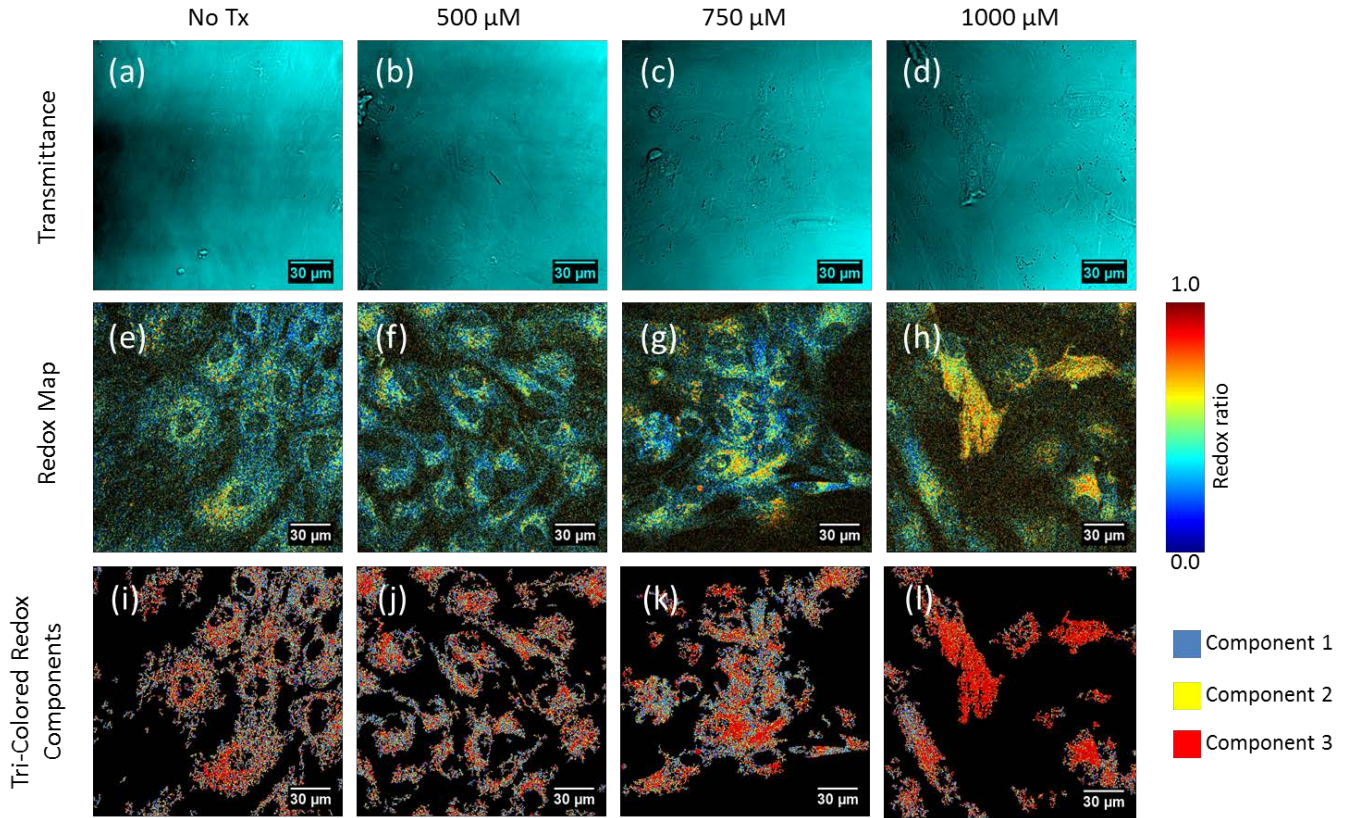


Figure 41: Effects of increasing doses of MnCl_2 on astrocyte morphology and redox ratio. (a-d) Transmittance images (e-h) Redox ratio maps (i-l) Redox component maps

We also assessed the impact of increasing doses on MnCl_2 on astrocytes. Initially, we tested the effects of 100, 250, and 500 μM MnCl_2 on the astrocytes and saw minimal effects (data not shown), for this reason, the dose range was increased to 500-1000 μM . In the transmittance images, we see that astrocyte morphology changes with increasing MnCl_2 dose (Figure 41a-d), becoming rougher in appearance. In concert with these morphological changes, we also see increases in redox ratio (Figure 41e-f). Finally, as with neurons, we increasingly

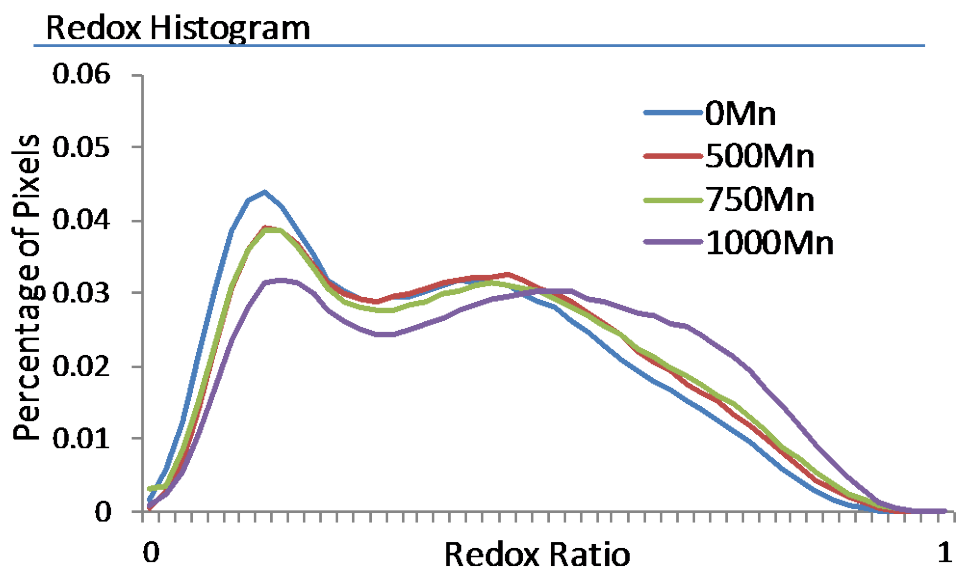


Figure 42: Redox histograms of MnCl_2 -treated astrocytes reveal a shift to the right with increasing doses, similar to neurons, but at higher concentrations

see component 3 dominate individual astrocytes (Figure 41i-l). The shifts in redox

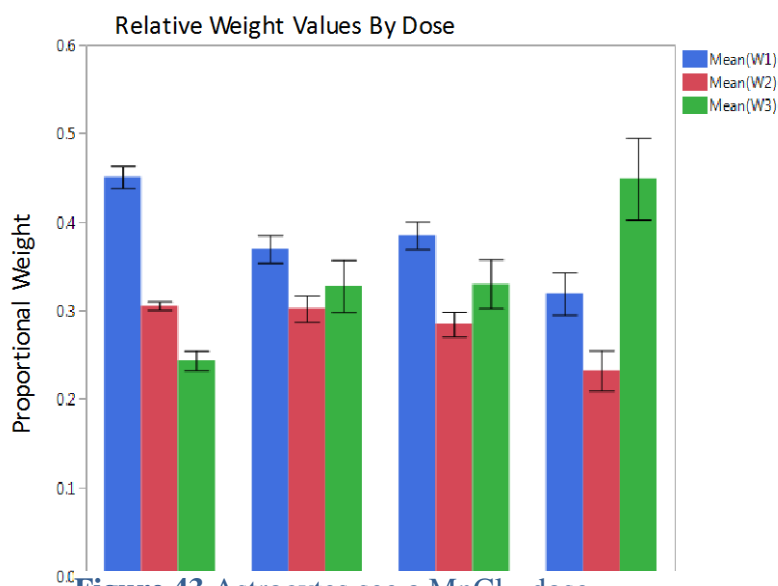


Figure 43 Astrocytes see a MnCl_2 dose-dependent increase in weight of component 3 and decrease in weights 1 and 2.

ratio histograms
also reflect the
increasing
dominance of
component 3
with dose
(Figure 42).

Similar to neurons, astrocytes experience relative increases in component 3 with dose, however they see decreases in both components 1 and 2 with dose, rather than primarily component 2 (Figure 43). These shifts are reflected in statistically significant decreases in $W1/(W2+W3)$ and $W2/(W1+W3)$ and

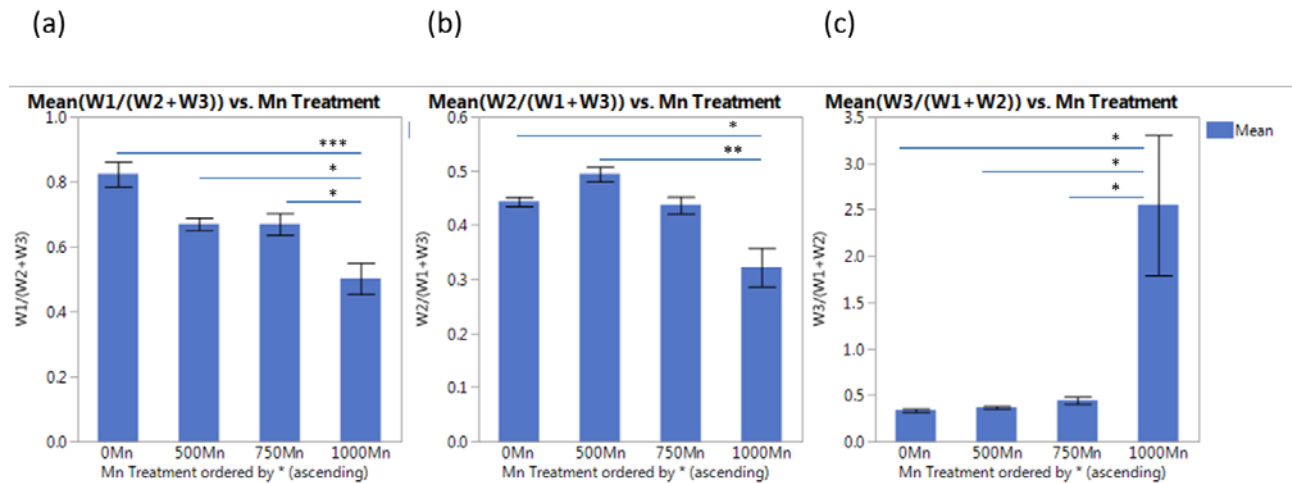


Figure 44: When astrocytes are treated with sufficiently high doses of Mn, they show a decrease in relative weights of components 1 and 2, and an increase in component 3.

increases in $W3/(W1+W2)$ between the 0uM and 1000uM $MnCl_2$ groups (Figure 44). It appears that while astrocytes are more resilient than neurons to low doses of Mn, both glycolytic and oxidative forms of energy production see a relative decline with Mn treatment, making way for a dramatic increase in the contribution of component 3. This component may indicate oxidative stress or apoptosis in the astrocytes. Mn-treated astrocytes exhibit an increase in caspase-3, however it is not statistically significant (Figure 45).

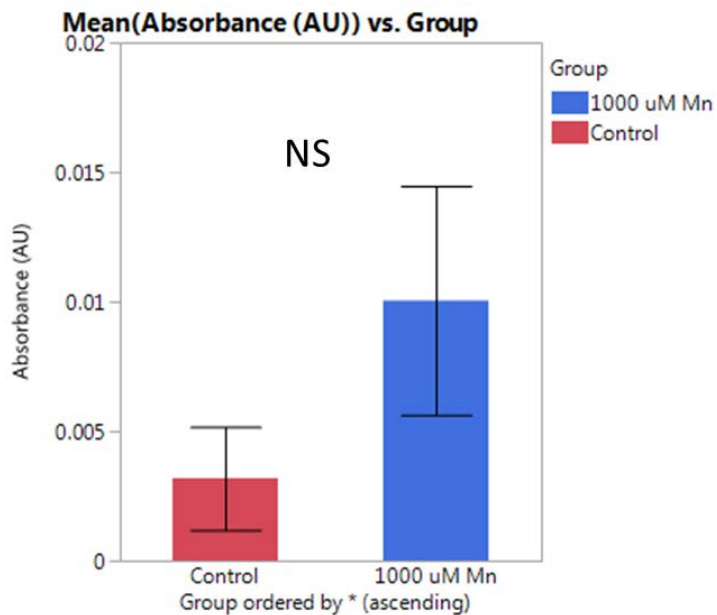


Figure 45: Caspase-3 assay in control and Mn-treated astrocytes

In summary,

both astrocytes and neurons exhibit morphological changes and increasing relative weight of redox ratio component 3 with MnCl_2 treatment.

Astrocytes exhibit changes at higher doses

than neurons, which is consistent with their greater resilience to mitochondrial assaults. The MnCl_2 -induced increase in redox ratio may be attributed to apoptosis or oxidative stress.

2.c.iii.6. Effect of Manganese on Monoculture Mitochondrial

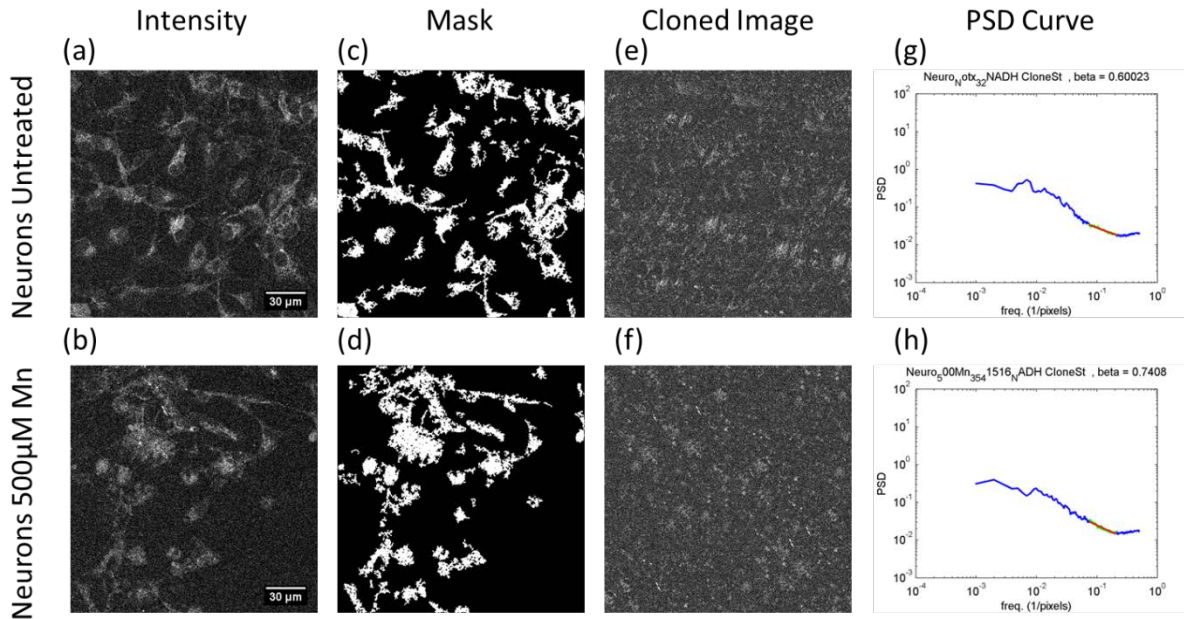


Figure 46: NADH intensity images (a-b), masks (c-d), cloned images (e-f), and PSD curves (g-h) for neurons with and without Mn treatment

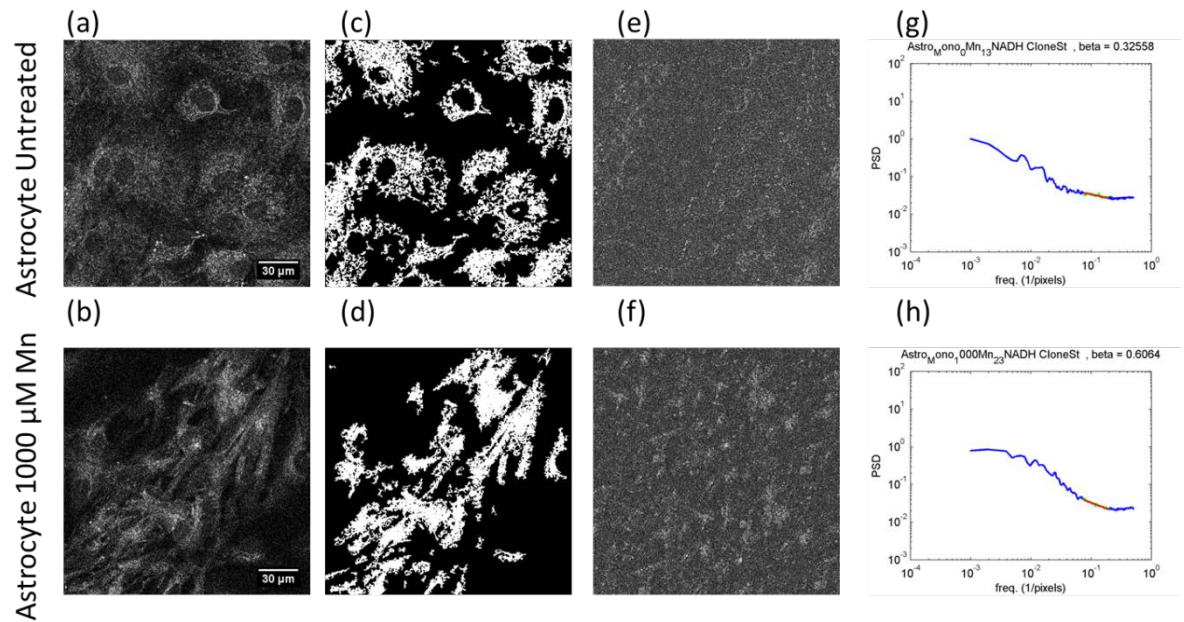


Figure 47 NADH intensity images (a-b), masks (c-d), cloned images (e-f), and PSD curves (g-h) for astrocytes with and without Mn treatment

Organization

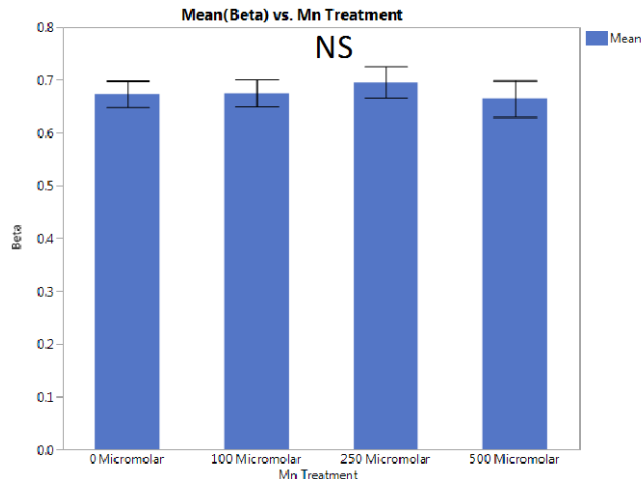


Figure 48: Neuron β value is not significantly different between treatment groups.

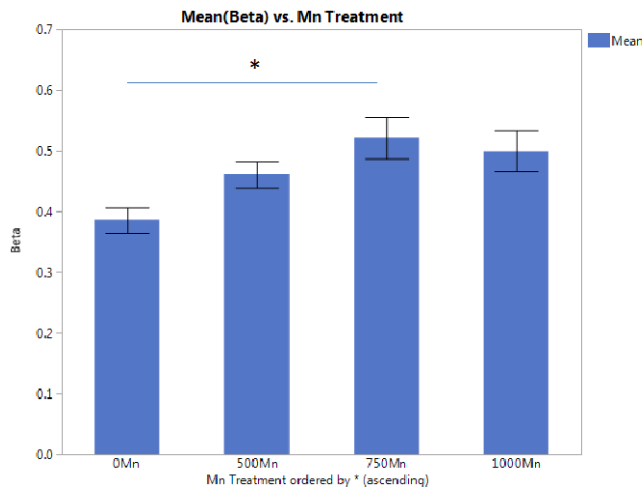


Figure 49: Astrocyte β value increases between 0 and 750 μ M treatment

Manganese treatment does not appear to significantly alter neuron mitochondrial organization as analyzed using our methods – there is no significant difference in β value between groups (Figure 48). This is likely due to the

fact that neuron mitochondria are very densely packed relative to astrocyte mitochondria, and it is therefore difficult for our analysis methods to distinguish subtle changes in mitochondrial patterns at the given resolution.

Astrocytes, on the other hand, do show significant

alterations in clustering with Mn treatment. β shows an increasing trend between 0, 500, and 750 μ M which is statistically significant between 0 and 750 μ M. The trend then levels off. This trend is consistent with previous research suggesting

that Mn treatment may cause increased mitochondrial fragmentation. The leveling from 750 to 1000 μM may indicate that the astrocyte mitochondria have hit a limit to their remodeling as metabolism begins to fail and cells undergo apoptosis.

2.c.iii.7 Effect of Manganese on Monoculture NADH Fluorescence

Lifetime

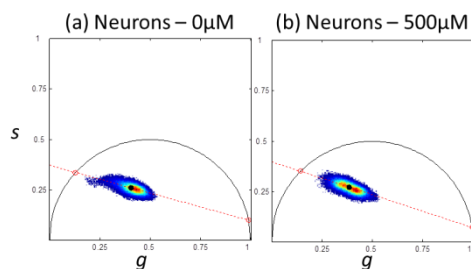


Figure 51: Phasor plots of NADH lifetime data from untreated (a) and Mn-treated (b) neurons

NADH fluorescence lifetime images were taken of neurons with and without 500 μM MnCl_2 (Figure 50a-b). Phasor plots illustrate a shift to longer NADH

lifetimes in the Mn-treated neurons (Figure 51). This shift is quantified in a

statistically significant increase in bound fraction with Mn treatment (Figure 54a).

Imagewise standard deviation of bound fraction shows a statistically significant decrease with Mn treatment (Figure 54b).

Increasing bound fraction could be associated with increased oxidative stress, as bound fraction has been shown to

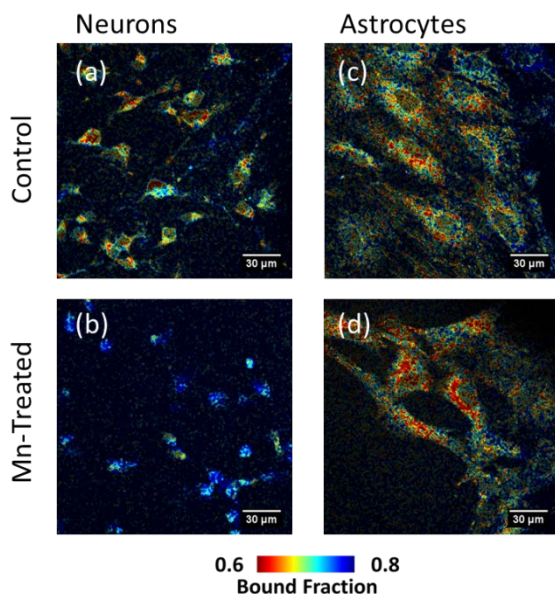


Figure 50: NADH fluorescence lifetime images of neurons with and without 500 μM Mn (a-b) and astrocytes with and without 1000 μM Mn (c-d)

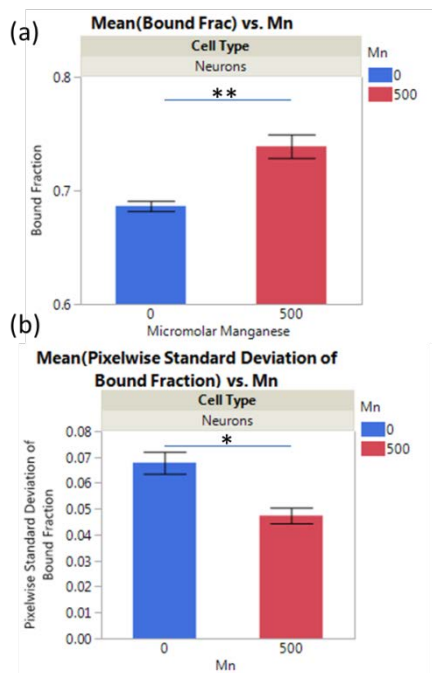


Figure 54: (a) Control vs. Mn-treated neuron bound fraction (b) Control vs. Mn-treated neuron imagewise bound fraction standard deviation

(a) Astrocytes - 0 μ M Mn (b) Astrocytes - 1000 μ M Mn

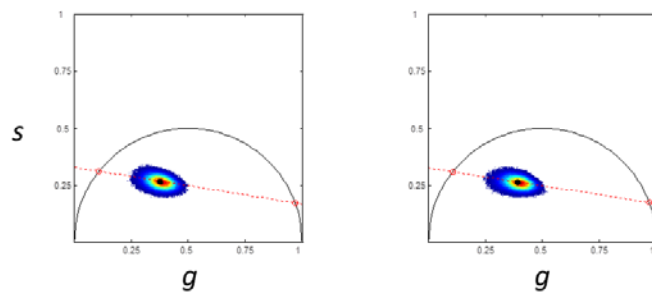


Figure 53: Phasor plots of NADH lifetime data from untreated (a) and Mn-treated (b) astrocytes

increase with hydrogen peroxide application in neural stem cells [83].

FLIM data was also collected on

astrocytes with and without treatment with 1000

μ M MnCl_2 (Figure 50c-d). Astrocytes show a

shift to shorter lifetimes with Mn treatment

(Figure 53). This shift is quantified in the

statistically

significant decrease

in bound fraction

between control and

Mn-treated

astrocytes (Figure

52a). This result

may indicate a shift

towards glycolytic

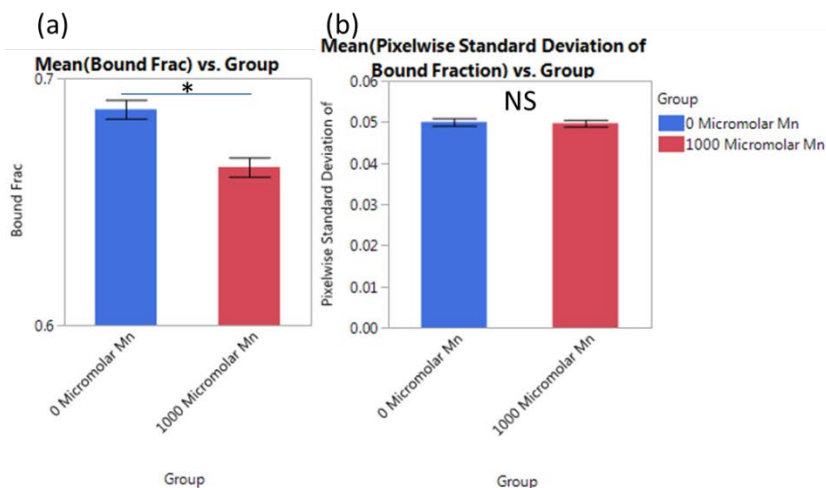
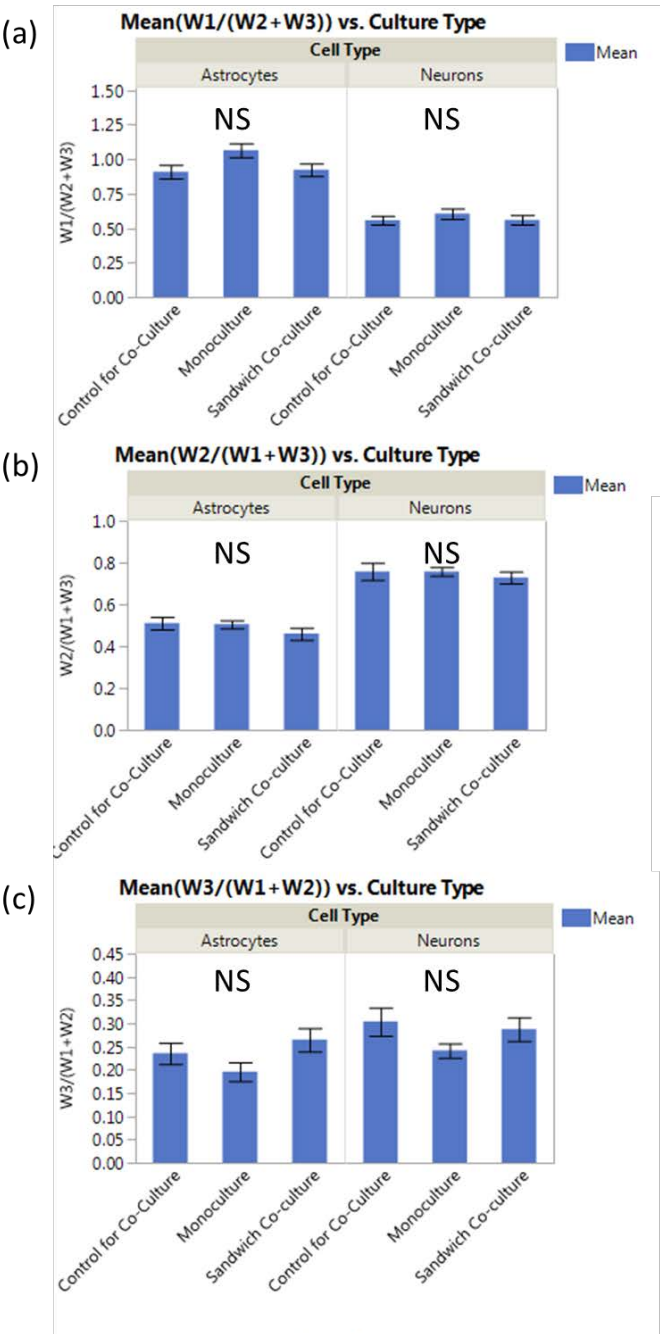


Figure 52: (a) Control vs. Mn-treated astrocyte bound fraction (b) Control vs. Mn-treated astrocyte imagewise bound fraction standard deviation

metabolism as Mn impairs oxidative metabolism. Standard deviation of bound fraction is consistent between groups (Figure 52b)

2.c.iii.8. Astrocyte and Neuron Co-Culture Systems

Astrocyte and neuron redox ratio distributions were next compared across multiple co-culture conditions in order to evaluate whether culturing cells together could modulate metabolism. In the first “sandwich” co-culture setup, redox ratio histograms do not appear markedly different between culture conditions (Figure 56). This homogeneity is further confirmed by the consistency in $W1/(W2+W3)$, $W2/(W1+W3)$, and $W3/(W1+W2)$ values between conditions (Figure 55). The lack of other statistically significant differences suggests that the sandwich co-culture condition does not meaningfully modify cell metabolism as measured by optical redox ratios.



70 **Figure 55:** Relative redox component values in sandwich co-cultures

The second co-culture condition involved transferring conditioned media between the cell types. When examining the redox histograms, differences between conditions appear relatively minor (Figure 58). The quantitative data shows no significant changes in $(W1/(W2+W3))$ (Figure 60a). However there is a significant decreases in $(W2/(W1+W3))$ between the astrocyte-conditioned media group and both the fresh media and neuron-conditioned media groups for astrocytes (Figure 60b), perhaps because astrocyte-conditioning depletes the media of certain nutrients, resulting in altered metabolic activity for that group. The increase in $(W2/(W1+W3))$ between the astrocyte-conditioned media and fresh media for neurons and in $(W3/(W1+W2))$ between astrocyte-conditioned

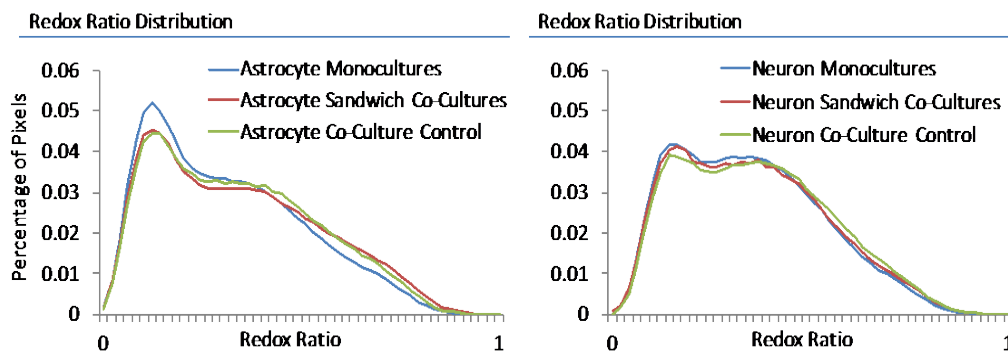


Figure 56: Redox histograms for sandwich co-cultures

and fresh media in astrocytes (Figure 60b-c) are likely due to the age of the media, rather than an effect of the astrocyte-conditioning, since the neuron-conditioned groups show similarly increased trends and are not significantly different than the astrocyte-conditioned media.

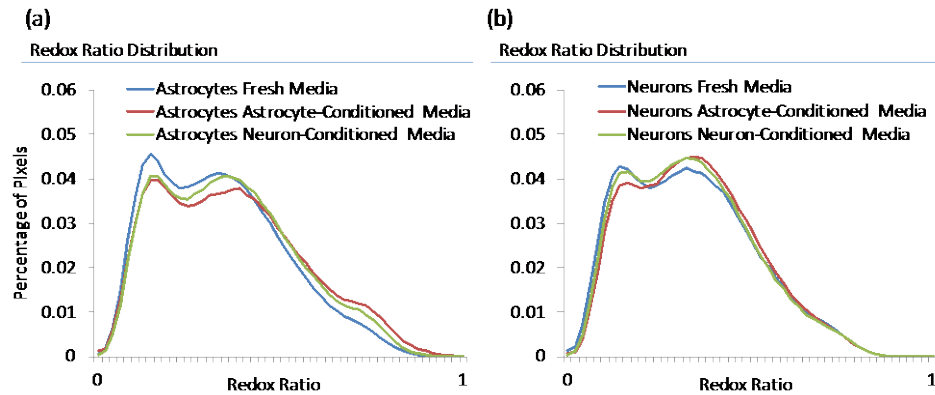


Figure 58: Redox ratio distributions for astrocytes (a) and neurons (b) in conditioned-media experiments

The final co-culture setup allowed cells to interact via transwell membranes. The redox distributions show little change between groups for astrocytes, and a slight rightward shift for neurons (Figure 57a-b). There is a significant decrease in $(W2/(W1+W3))$ for neurons cultured with astrocytes in transwells relative to the neuron monoculture control, as well as a trending increase in $(W3/(W1+W2))$ (Figure 59). This modulation could suggest that the presence of the astrocytes

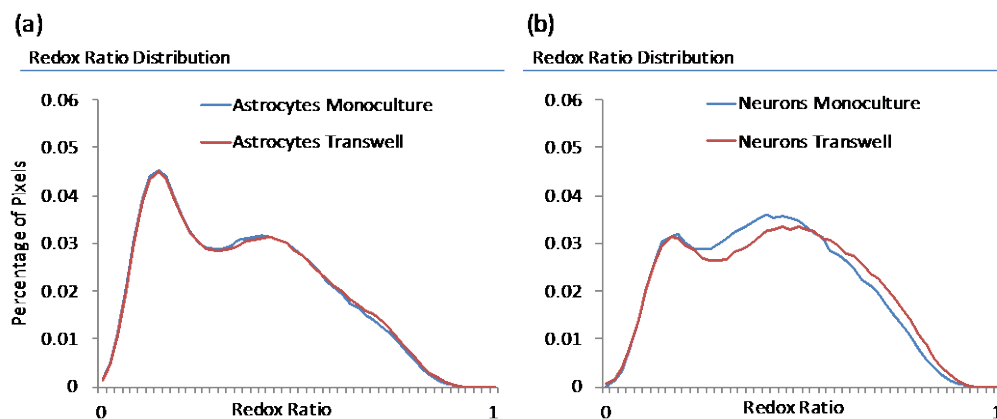


Figure 57: Redox ratio distributions for astrocytes (a) and neurons (b) in transwell experiments

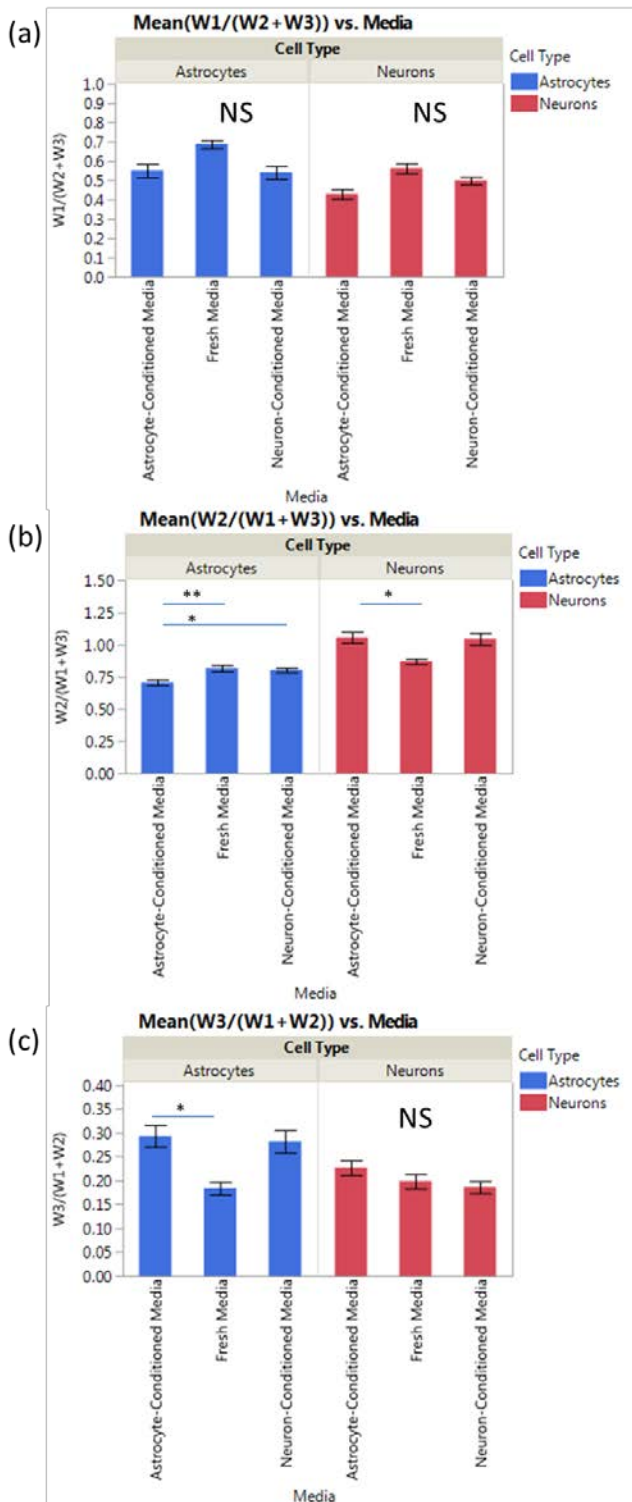


Figure 60: Redox ratio components for media conditioning experiments.

may have actually reduced neuron oxidative metabolism or caused them to exhibit shifts otherwise associated with stress. Additional experimentation would be needed to establish the reproducibility of this effect.

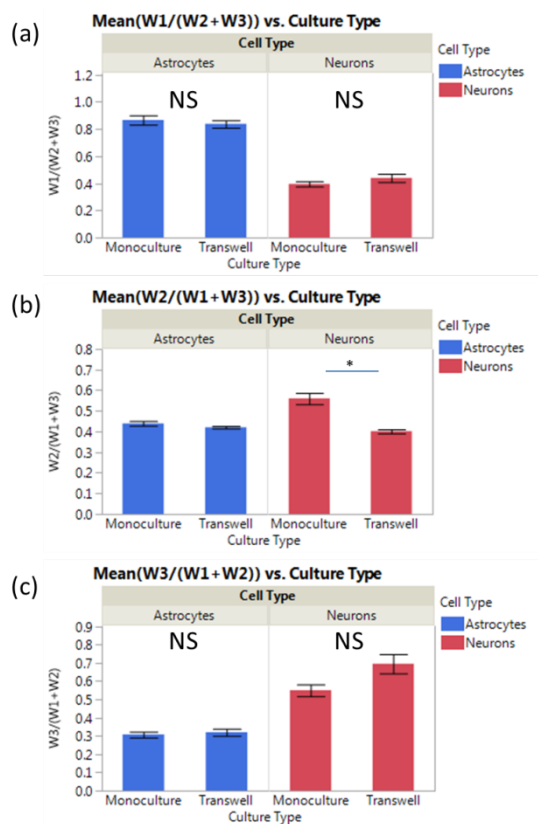


Figure 59: Redox ratio components in media transfer experiments

2.c.iii.9. Effect of Manganese on Co-Culture Systems

We next assessed the effects of MnCl_2 on sandwich co-culture conditions in order to determine whether astrocytes could protect neurons from MnCl_2 toxicity. We selected $500\mu\text{M}$ as the MnCl_2 dose because it was a dose demonstrated to have low effect on astrocytes, but significant effect on neurons.

In redox histograms of control and Mn-treated sandwich co-cultures, we see that astrocytes show minimal modulation by either culture condition or MnCl_2 concentration (Figure 62). This result is consistent with our expectation that astrocytes are minimally affected by $500\mu\text{M}$ MnCl_2 . Manganese-treated neurons, on the other hand, seem to show a reduced rightward shift in both the co-culture control and sandwich co-culture condition, suggesting that the sandwich setup may reduce the effect of MnCl_2 on the cells. However, the quantitative metrics are largely insignificant between culture types (Figure 64), except for between the Mn-treated neurons in sandwich co-cultures vs. in monocultures for $(W2/(W1+W3))$. However, there is no significant difference between the result in sandwich co-cultures and the co-culture control, so the difference obtained may be more attributable to the sandwich setup than to interactions between the two cell types.

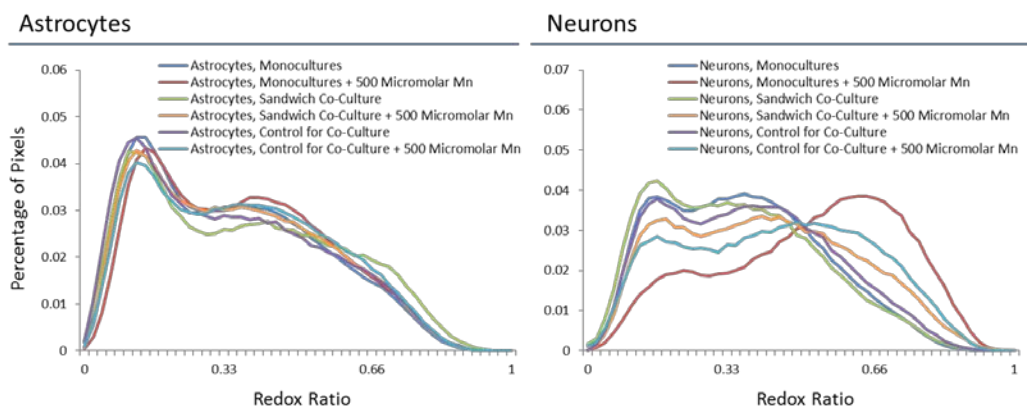


Figure 62: Redox distributions for sandwich co-cultures treated with Mn

We also examined whether co-culturing neurons and astrocytes in transwells could reduce the impact of MnCl_2 treatment on either cell type. As with the sandwich co-cultures, there appear to be minimal effects of the culture conditions on the redox histograms (Figure 61). Statistical comparisons of between culture types for a given cell type and dose level do not show any

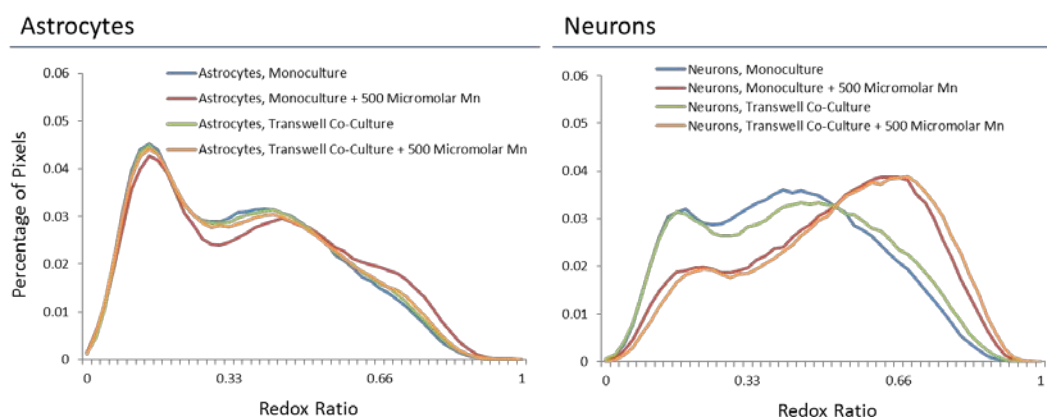


Figure 61: Redox distributions for transwells treated with Mn

statistically significant differences between culture types within the Mn-treated groups (Figure 63). This result suggests that transwell co-cultures also do not mitigate the impacts of MnCl_2 poisoning on neurons.

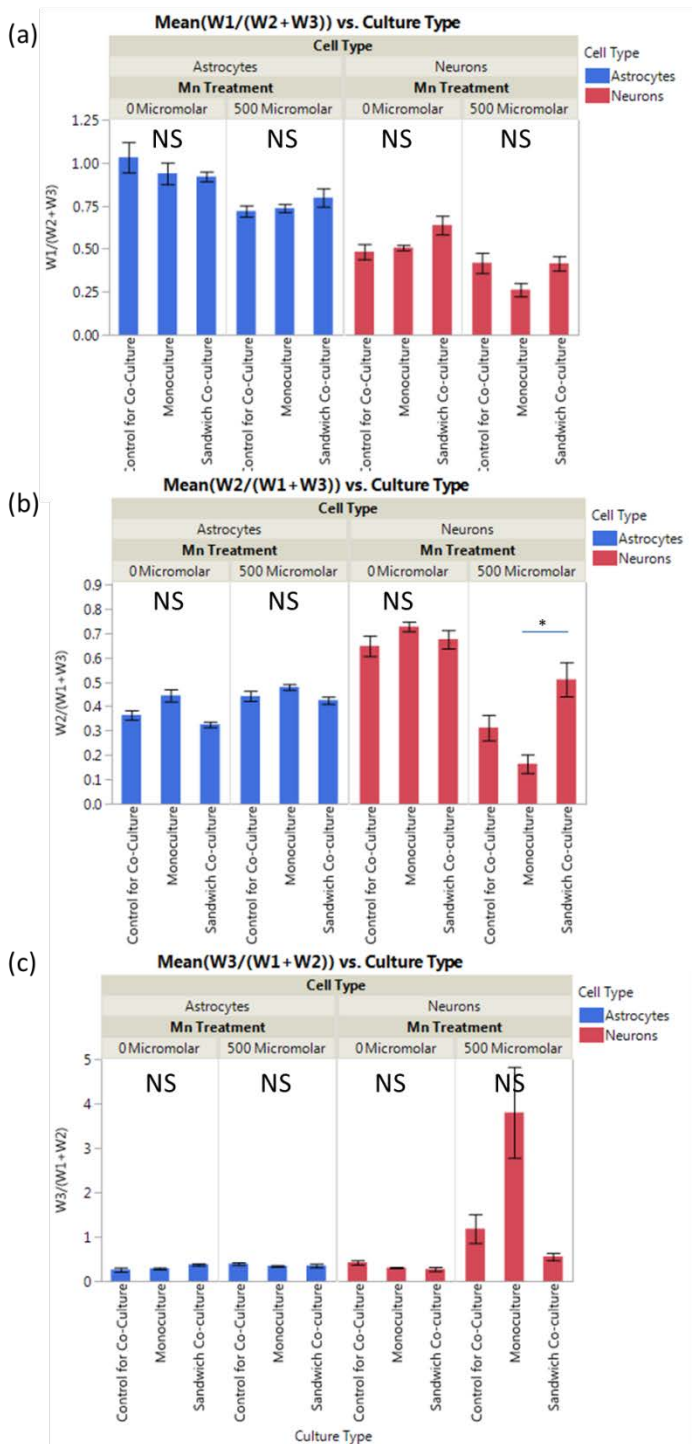


Figure 64: Redox components for sandwich co-cultures treated with Mn

76

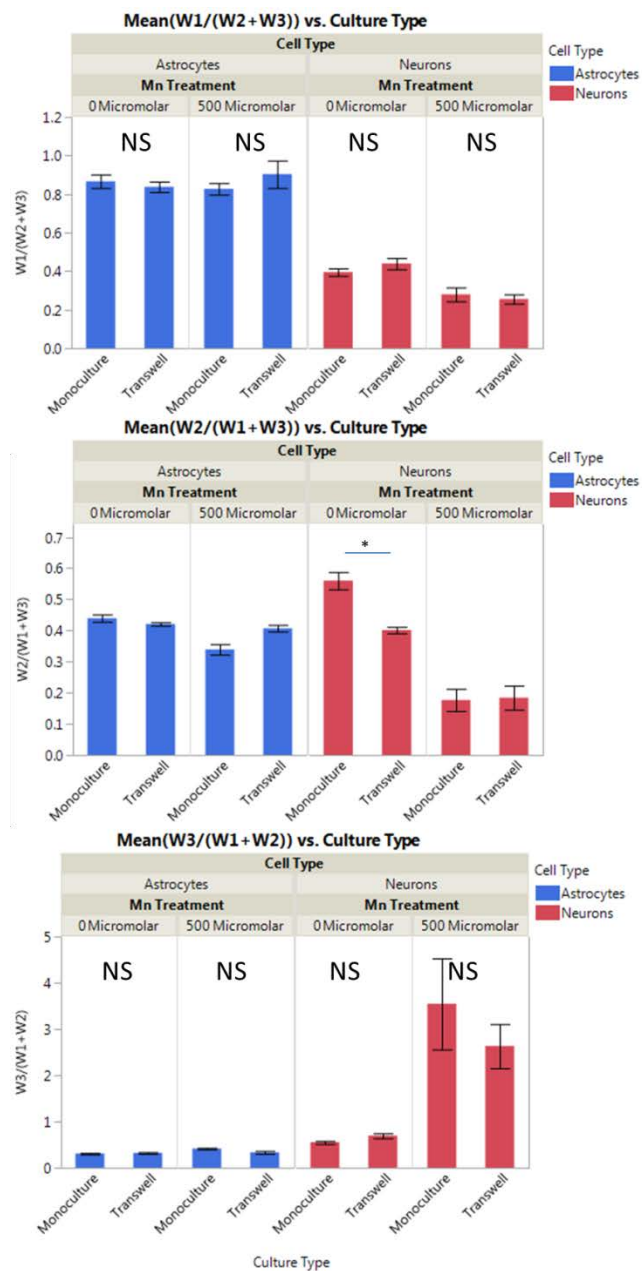


Figure 63: Redox components for transwell co-cultures treated with Mn.

2.C.IV. DISCUSSION

These initial results establish the utility of TPEF imaging of endogenous fluorophores NADH and FAD for detecting metabolic differences in healthy neurons and astrocytes, as well as their differing responses to manganese toxicity. We demonstrated that pixelwise optical redox ratios (defined as $FAD/(FAD + NADH)$) in the two cell types fall into three Gaussian distributions, representing multiple metabolic states and potentially different populations of mitochondria. In healthy neurons and astrocytes, neurons had a significantly greater $W2/(W1+W3)$ and $W3/(W1+W2)$ than astrocytes. Astrocytes had a significantly higher relative weight $W1/(W2+W3)$ than neurons. These quantitative metrics reflect that a greater proportion of neuronal pixels fall into higher-redox-ratio distributions than astrocytes, a difference typically associated with increased oxidative vs. glycolytic metabolism, as suggested by increased FAD vs. NADH fluorescence [7]. These results are consistent with numerous studies suggesting that neurons tend to utilize oxidative metabolism more exclusively than astrocytes, which also show robust glycolytic activity [8].

Neurons also exhibit significantly higher mitochondrial clustering than astrocytes. Previous research has linked higher clustering to increased glycolysis through oxygen-deprivation studies, which would seem to contradict our redox results [82]. However, examination of the NADH intensity images, cloned images, and PSD curves for the two cell types suggests that the results may reflect

differences in mitochondrial density within the two cell types, which have dramatically different morphology, as opposed to mitochondrial networking alterations. Neuron mitochondria tend to be densely packed within a tiny soma, while astrocyte mitochondria may spread out within a widespread cytoplasm. Therefore, resolution limitations may prevent us from accurately discerning neuron mitochondrial networks within the packed soma, thus driving high clustering values relative to astrocytes, whose networks may be more clearly delineated in images.

Preliminary NADH FLIM data from astrocytes and neurons show that astrocytes have a greater average NADH bound fraction than neurons, but that neurons have a greater average standard deviation of bound fraction values, with an apparent tail along the NADH trajectory corresponding to long fluorescence lifetimes. Bound NADH is typically viewed as evidence of oxidative activity, while free NADH is typically viewed as evidence of glycolytic activity [69]. While astrocytes' higher average bound fraction could thus be interpreted as an indicator of more oxidative activity, neurons' broader spread in bound fraction values and population of high bound-fraction pixels suggest robust oxidative activity in neurons as well. Additionally, differences in binding status could reflect different baseline mitochondrial states between the two cell types – for example, neurons may allow for more TCA-derived NADH buildup within the

mitochondria prior to oxidation than astrocytes, yielding a lower bound fraction in spite of mitochondrial activity.

Both cell types exhibited morphological and redox changes in response to MnCl_2 treatment. Neurons exhibited neurite loss and a significant decline in $W2/(W1+W3)$ and increase in $W3/(W1+W2)$ between the control and $500\mu\text{M}$ conditions. Neurons which began to show nuclear blebbing and axonal loss also lost their heterogeneous mixture of all the three redox ratio components and were increasingly dominated by component 3. The increase in $W3/(W1+W2)$ may be attributed to an increase in apoptosis or oxidative stress – both have been tied to high redox ratios in previous studies [60, 62, 64]. The presence of apoptosis in particular is suggested by axonal loss and morphological changes, as well as by the increase in caspase-3 levels detected in manganese-treated neuron cultures. The decrease in $W2$ could be interpreted as a decline in neurons' predominant oxidative activity, as manganese poisoning is known to impair respiratory activity [39].

While astrocytes were not dramatically impacted by $500\mu\text{M}$ of manganese, $1000\mu\text{M}$ doses produced greater effects to morphology, redox ratio, and mitochondrial organization. These results are consistent with previous research suggesting that neurons are more vulnerable than astrocytes to manganese poisoning [39]. At $1000\mu\text{M}$, astrocytes changed in texture and also saw a decline in both $W1/(W2+W3)$ and $W2/(W1+W3)$ as well as an increase in

W3/(W1+W2) relative to the untreated conditions. As with neurons, increases in W3 may be tied to either apoptosis or oxidative stress. However, caspase-3 levels were not shown to be significantly increased in astrocytes, possibly reflecting a slower apoptosis process (caspase-3 is a late apoptosis marker) or fewer cells undergoing apoptosis in resilient astrocyte cultures. That W1 and W2 remained relatively constant at doses toxic to neurons and then declined together at high doses alongside increasing W3 suggests that neither glycolytic or oxidative processes are selectively impaired by the toxicity, consistent with astrocytes' ability to maintain and modulate metabolic activity even while experiencing some toxicity.

Astrocytes also exhibited increases in mitochondrial clustering between 0 and 750uM doses, consistent with previously observed mitochondrial fission in manganese-poisoned brain cancer cultures [55, 56]. Neurons showed similar clustering levels across Mn doses, which, given that they were experiencing significant redox changes, may reflect the limits of our image resolution to reflect networking changes between tightly packed mitochondria within the soma.

Preliminary FLIM data also revealed that neurons and astrocytes have differing responses to Mn treatment. Neurons saw an increase in bound fraction when treated with manganese, which corresponded to toxic alterations in morphology. This increase may have been due to oxidative stress, as previous research has shown an increase in NADH fluorescence lifetime when cells are

treated with hydrogen peroxide [83]. Astrocytes saw a decrease in bound fraction when treated with manganese, typically interpreted as a shift towards more glycolytic metabolism [70], providing evidence that astrocytes modulate metabolism in response to Mn toxicity.

The various co-culture conditions we employed were unsuccessful in modulating baseline cell metabolism, as quantified via changes in relative weights of redox ratio components. Nearly all of the cases with significant differences in $W1/(W2+W3)$, $W2/(W1+W3)$, or $W3/(W1+W2)$ reflected changes between co-cultures and monoculture conditions, rather than differences between co-cultures and their appropriate co-culture controls. These shifts may therefore be attributed to alterations caused by the various co-culture setups, for example, a lack of nutrient circulation in the sandwich co-culture setup, or the degradation of media in the conditioned-media experiments, rather than changes caused by cell interactions. While there was a significant decrease in $W2/(W1+W3)$ between astrocytes treated with astrocyte-conditioned and neuron-conditioned media, it is not clear whether this change had more to do with a depletion of nutrients in the astrocyte-conditioned media relative to neuron-conditioned media (astrocytes require media changes more often than neurons), than to do with factors secreted by neurons. Unfortunately it would be difficult to develop a controlled experiment to test this due to the confounding factors of media age, media consumption/processing by cells, and factor secretion by cells. While the

transwell condition showed some potential modulation in neuron metabolism relative to the control, the result trended in the direction of the apoptotic / stressed cells in the Mn-treated studies (e.g., decreasing $W2/(W1+W3)$ and increasing $W3/(W1+W2)$). We would need to determine whether this result was reproducible, and if so, whether the condition was actually harming, rather than enhancing, cell health.

A lack of metabolic modulations in co-cultures vs. monocultures may have been a result of the amount of time the cells were cultured together, the lack of physical contact or proximity between cell types, or a low level of neuronal firing activity in the cultures. In both the sandwich co-cultures and media transfer conditions, cells were exposed to one another's soluble factors released over 2 days or less, which may have been insufficient to allow enough soluble factor release to cause metabolic alterations. Unfortunately, increasing the timeframe for soluble factor release in these two culture conditions is limited by the need for fresh media in both conditions every 2-3 days. In the transwell condition, cells were cultured together for >5 days, however the timeframe only included 1-2 days in which neurons had formed mature neurite networks. It is possible that culturing neurons and astrocytes together for additional time after neurons had formed mature networks may alter metabolic exchange. Physical contact or close proximity between the cell types may also be crucial to metabolic coupling; excess glutamate in neural synapses is thought to trigger astrocytic glycolysis and

glutamate recycling [8], so the physical separation between cell types in our experiments may have prevented physiologic interactions. Culturing astrocytes and neurons in physical contact with one other would pose a challenge for separating cell types' respective autofluorescence signals, however co-staining with a cell-specific marker could enable some segmentation [72]. Finally, many studies of the metabolic coupling between astrocytes and neurons suggest that neuronal firing activity is needed to create metabolic demand that triggers glycolytic astrocyte metabolism[84]. Though previous research has shown spontaneous firing of neurons in primary cultures of similar age and preparation to ours [85, 86], we did not study the signaling activity in our own cultures. The level of firing activity may not have been high enough to induce metabolic changes representing coupling.

The sandwich and transwell co-culture conditions also did not show astrocyte protection of neurons during manganese poisoning, as evidenced by insignificant differences between $W1/(W2+W3)$, $W2/(W1+W3)$, and $W3/(W1+W2)$ between the different culture conditions for a given cell type and dose level. From a technical standpoint, this may have been a result of $MnCl_2$ doses used, time of co-culture, or time of imaging. It is conceivable that astrocytes could have provided protection to neurons against lower doses of manganese or may have provided early protection to neurons that was not effective at the 24-hour timepoint. However, these insignificant results may also be reasonably

representative of the relative roles astrocytes and neurons play in scenarios of manganese toxicity. While astrocytes do provide antioxidants to neurons under healthy conditions, these are known to be reduced in toxic conditions [53]. Though we selected a manganese dose level (500uM) that appeared to strongly impact neurons and minimally impact astrocytes based on dosing studies in monocultures, astrocytes may still have been limited in their ability to offer sufficient energy substrates, antioxidants, and glutamate recycling to fully protect neurons [50, 53, 54, 87]. Future studies to elucidate mechanisms of toxicity protection could alternatively examine astrocyte and neuron responses to manganese given with or without known antioxidants [87].

In summary, TPEF optical redox imaging of NADH and FAD in astrocyte and neuron monocultures effectively showed metabolic differences between the two cell types' healthy redox status that were consistent with prior research suggesting that neurons rely more heavily on oxidative metabolism than astrocytes, which also produce energy via glycolysis. Astrocyte and neuron redox responses to manganese poisoning were consistent with research suggesting that neurons are more vulnerable to toxicity, as well as established optical redox ratio changes reflecting oxidative stress and apoptosis. Mitochondrial organization analysis showed distinct clustering patterns between the cell types, as well as differing responses to manganese poisoning. FLIM results also revealed cells' differing responses to toxicity. These results established TPEF of NADH and

FAD fluorescence as useful tool for studying mitochondrial activity and organization in brain cells. While results from co-cultures were largely insignificant, these primarily require further optimization of the cell culture conditions, as opposed to imaging methods. In the future TPEF could be used to study metabolic changes during neuronal activation and for a range of toxicity / protection studies.

2.D. CHARACTERIZING NORMAL VS. DISEASED CELL METABOLISM IN ADULT HUMAN NEURAL PROGENITOR CELLS (AHNPs) DERIVED FROM HEALTHY AND PARKINSON'S PATIENTS

2.D.I. INTRODUCTION

Having characterized primary astrocyte and neuron redox and mitochondrial organization responses to manganese poisoning via TPEF of NADH and FAD, we wished to compare the results to a PD model with the hypothesis that NADH and FAD autofluorescence changes due to manganese toxicity would resemble metabolic changes resulting in neurodegeneration. We therefore imaged adult human neural progenitor (AHNPs) cells derived from brains of patients with and without PD. AHNPs are astrocytic stem cells that have been derived from human brain tissue samples and expanded ex vivo [88]. Control AHNPs, derived from patients undergoing surgery to treat forms of epilepsy, typically can be differentiated into multiple brain cell types and are being explored for applications in neural regeneration [88]. AHNPs derived post-mortem from patients with PD have more limited differentiation potential but are also expandable and useful for studies of PD [89]. In this study, we compared mitochondrial redox ratio and organization between control and PD-derived AHNPs and identified similar trends to those found in Mn-treated primary cells.

2.D.II. MATERIALS AND METHODS

2.d.ii.1. Cell Culture

Control and PD-derived hippocampal AHNPs were provided by collaborators in the Steindler Laboratory. These cells had been expanded in N5 medium (DMEM, N2, 5% fetal bovine serum, bovine pituitary extract) supplemented with endothelial growth factor and basic fibroblast growth factor, and were plated on glass-bottomed petri dishes for imaging.

2.d.ii.2. Imaging

Similar to studies with primary cells, images were taken with a Leica SP2 confocal microscope fitted with a Ti:Sapphire laser. Laser light was focused to the sample using a 40x water-immersion objective (NA 1.1), and neutral density filters were used to achieve a power of 20-25 mW at the stage. Samples were excited with light at 755 and 860nm and fluorescence images were formed using non-descanned detectors filtered to collect light at 460 +/- 20nm and 525 +/- 25nm. Images were 512x512 pixels, with the zoom feature of the built-in Leica Control software employed to achieve a 187x187 micron field of view. Images were formed based on an average of 8 scans. 5-8 non-overlapping images were taken per petri dish or well, and 2-3 dishes or wells were imaged per cell type, for a total of ~15 images per cell type.

2.d.ii.3. Data Analysis

For redox analysis, images were first processed using the same approach described for primary cultures. Redox histograms and continuous redox maps were also formed using the same approach. To determine the basis redox ratio

components for the redox histograms, we used the `gmdistribution.fit` function within Matlab to fit a 3-component Gaussian mixed model to the aggregated pixels from the images of the control AHNPs. The fitting was performed 10 times, and the mean and standard deviations of the three components were averaged across the 10 iterations. We then determined the image-by-image relative weights of the redox basis components as described for primary cultures, using the basis components from the control AHNPs. Redox ratio tri-colored component maps were constructed using cutoffs based on the midpoint between the Gaussian component means derived from the aggregate control AHNPs redox ratio distribution. Mitochondrial organization analysis followed the approach previously described for primary cells [81, 82].

2.d.ii.4.Statistics

Statistical software (JMP) was used to evaluate differences in means of various image metrics (e.g., redox ratio component weight ratios, β) between groups (i.e., control vs. PD-derived AHNPs). First, image-wise values were split by group and experiment to identify and exclude outliers. Outliers were identified as values falling greater than 1.5 times the interquartile range above the 75th quantile of the data, or 1.5 times the interquartile range below the 25th quantile of the data. When the final data set was established, a mixed model was specified, including cell type as a fixed effect and petri dish as a random effect. The model was estimated using a restricted maximum likelihood (REML) method, and an F-

test was used to assess the significance of the fixed effect. If the effect was significant, a post-hoc student's t-test was applied to determine the significance of difference between groups. In cases where the model did not converge due to little variation in a random effect (e.g., petri dish), we determined that the effect could reasonably be excluded from the model and we estimated the revised model as described above. Error bars indicate standard error. * indicates $p < 0.05$, ** indicates $p < 0.01$, and *** indicates $p < 0.001$.

2.D.III. RESULTS

Images of control and PD-derived ANHPs show distinct morphology and redox

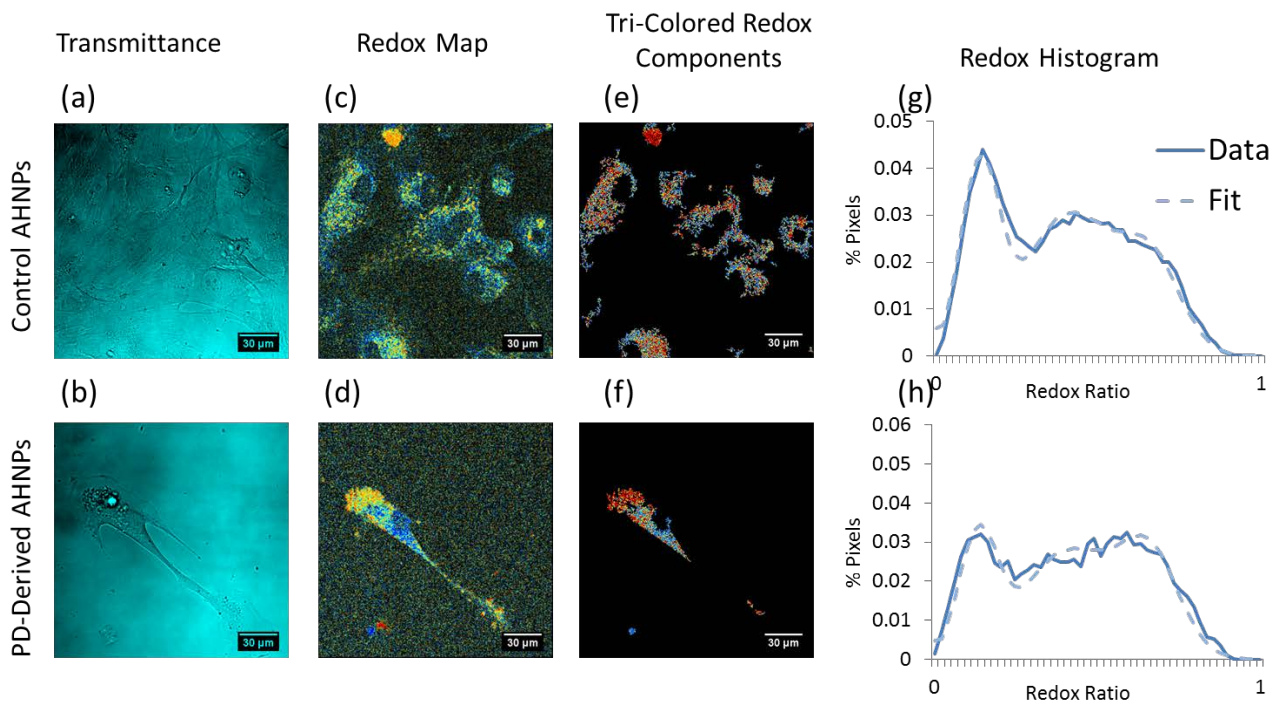


Figure 65: Images of control and PD-derived ANHPs (a-b) Transmittance images (c-d) Redox maps (e-f) False-colored redox components (g-h) Redox histograms with fits

patterns. Control AHNPs resemble healthy primary astrocytes and generally grew densely (Figure 65a). PD-derived AHNPs grew sparsely and often had a stressed appearance, with more limited spread and cytoplasmic irregularities (Figure 65b). Redox ratio maps show high redox ratio regions in PD-derived AHNPs, which is confirmed by the dominance of component 3 in regions of the PD-derived AHNPs, relative to the more heterogeneous control cells (Figure 65c-f). Redox histograms further indicate a rightward shift in redox ratios of PD-derived cells relative to the control, in both individual images as well as in the aggregate (Figure 65g-h, Figure 66). The control AHNP redox distribution is unmixed into three Gaussian sub-distributions, which can be interpreted as pixels in separate

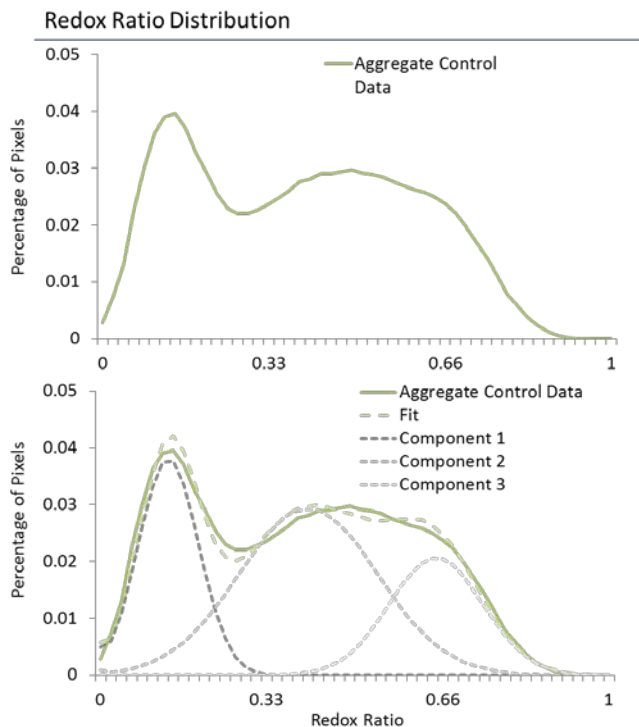


Figure 67: Gaussian redox components un-mixed from the control AHNP redox distribution.

redox states (Figure 67). The control AHNPs have the greatest weight of component 1, similar to results observed in primary cultured astrocytes (Figure 69). Parkinson's-derived AHNPs have the greatest weight of component 3, consistent with results from manganese-poisoned neurons and astrocytes (Figure 69). These differences between groups are reflected in

the significantly higher value of $W1/(W2+W3)$ in the control group relative to the PD-derived group, as well as the significantly higher value of $W3/(W1+W2)$ in the PD-derived group relative to the control group (Figure 68). Mitochondrial clustering trended higher in PD-derived cells than in control cells, however the difference was not statistically significant (Figure 70-Figure 71).

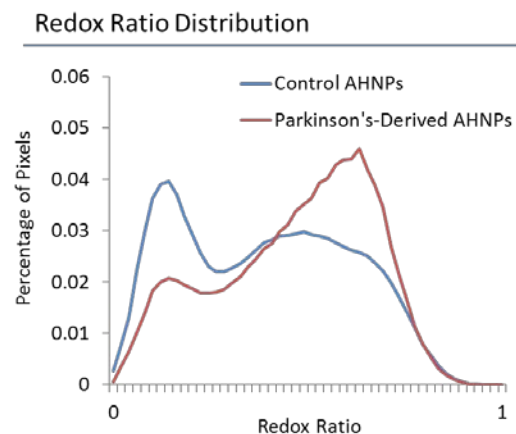


Figure 66: Redox ratio distributions for control and PD-derived AHNPs

2.D.IV. DISCUSSION

The results obtained from imaging control and PD-derived AHNPs were consistent with those obtained from images of control and manganese-treated

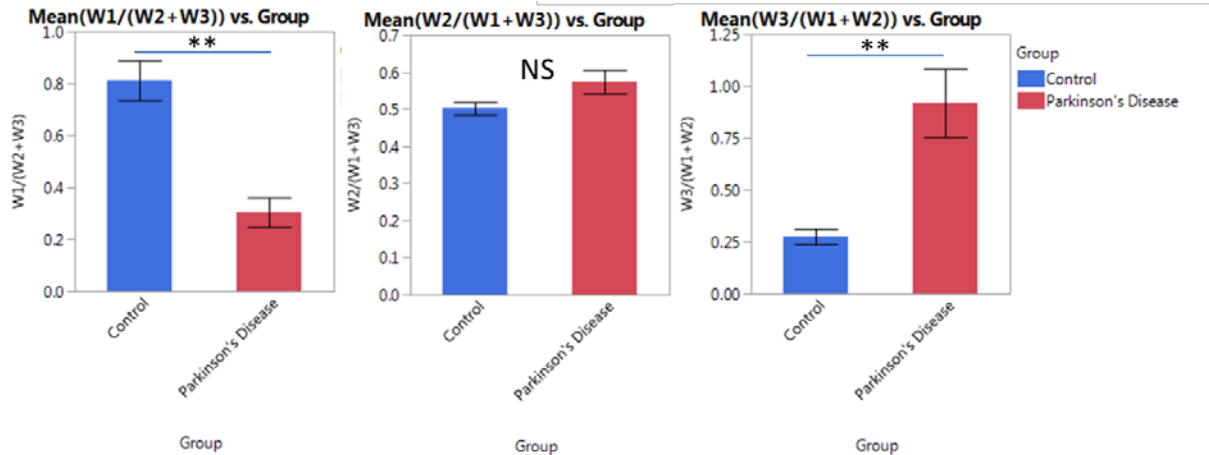


Figure 68: Redox components for AHNPs

primary neurons and astrocytes. When compared with control groups, both PD-derived and Mn-treated cells had an increase in high redox-ratio component 3 relative to the other redox components, as quantified by a significant increase in $W3/(W1+W2)$. Increased weight on this high redox-ratio component may be tied to increased apoptosis or oxidative stress in the PD-derived cells. Mitochondrial

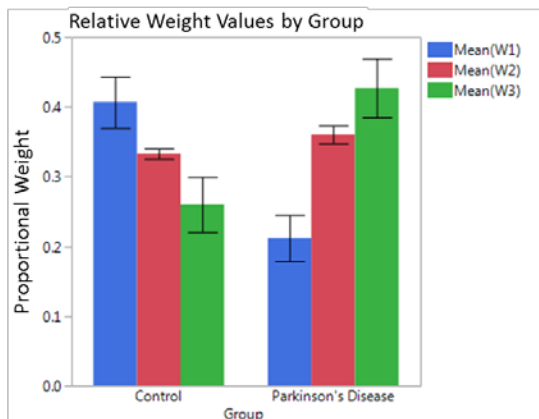


Figure 69: Component weights for AHNPs

clustering also trended higher in the PD-derived group than in the control group – the difference was not statistically significant, but could indicate imbalanced fission/fusion dynamics in these cells. In sum, the results obtained in AHNPs were

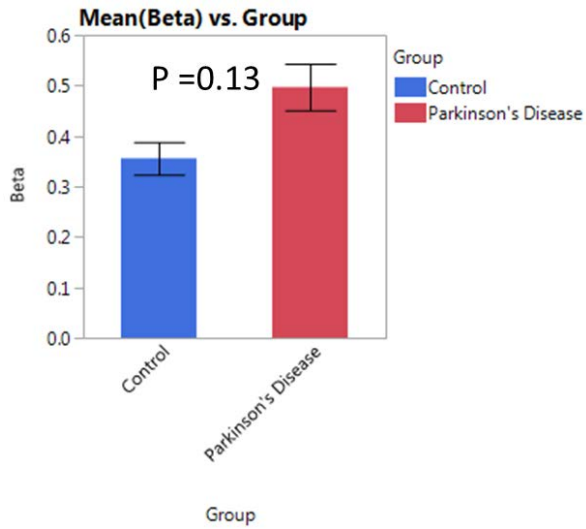


Figure 70: Clustering results for AHNPs

similar to the results obtained in the control and Mn-treated primary rat brain cells, and were also consistent with previous research tying increased optical redox ratios to oxidative stress and apoptosis.

This experiment establishes a connection between metabolic

changes in manganese toxicity and neurodegeneration. It also demonstrates that our imaging and analysis methods are not only relevant for dose-optimized toxicity studies, but also in detecting metabolic differences between healthy and diseased human-derived cells.

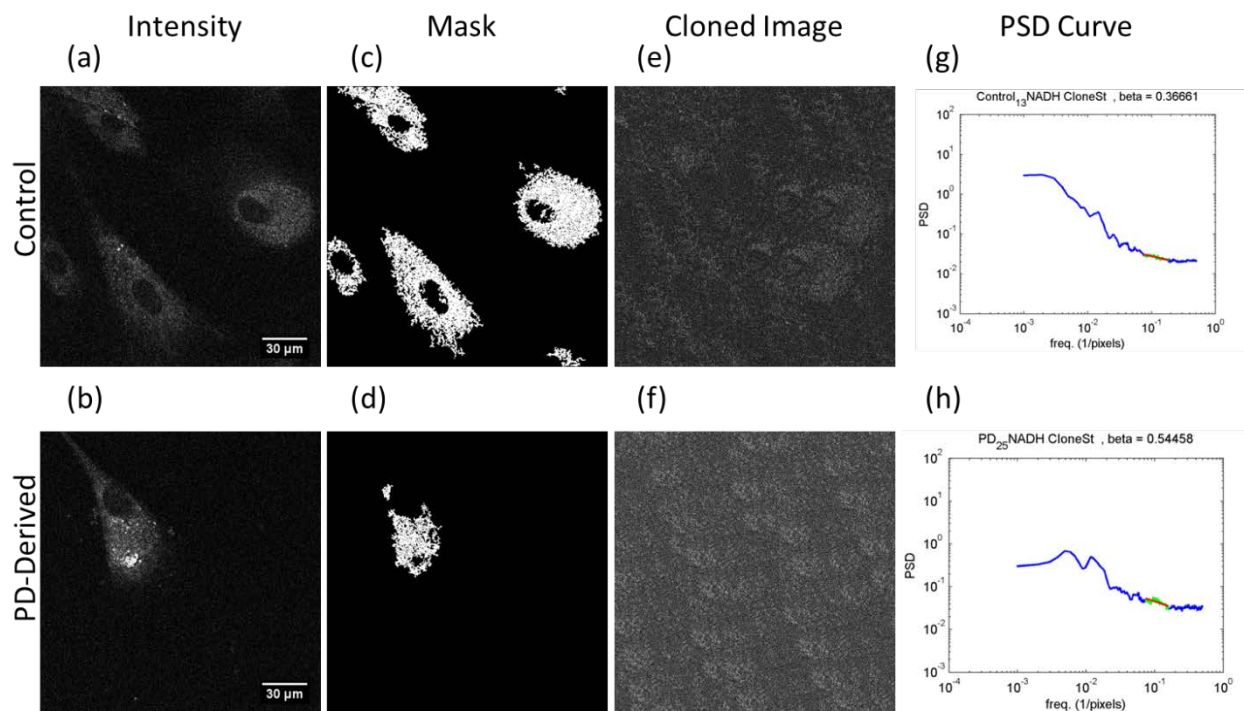


Figure 71 Control vs. PD-derived AHNP NADH intensity images (a-b) image masks (c-d) cloned images (e-f) and PSD curves (g-h)

3. AUTOMATED IMAGE ANALYSIS FOR NEURITE DENSITY QUANTIFICATION IN A 3D BIO-ENGINEERED BRAIN MODEL

3.A. BACKGROUND AND INTRODUCTION

In tissue, the extracellular matrix (ECM) encompasses all acellular components and provides structural support in addition to facilitating cell development, proliferation, differentiation, and communication [90]. The ECM typically contains fibrous structural proteins such as collagen and fibronectin, in addition to proteoglycans and glycosaminoglycans (GAGs) involved in cell signaling and adhesion [91]. Brain ECM tissue is unique in that it comprises a relatively low percentage of the tissue volume (20%), and has a very high ratio of GAGs relative to collagen [92, 93]. The brain ECM boasts a specialized set of proteins and biochemical factors contained within microdomains to supply the correct factors in the correct locations to support the various activities of brain cells [94]. One example is the enrichment of heparin and chondroitin sulfate proteoglycans in the neurogenic niche, which are thought to be important to stem cell proliferation and differentiation [94]. Another example is secretion of matricellular proteins by astrocytes, which supports neuronal networking by promoting synapse formation [95].

Three-dimensional bioengineered brain models are increasingly becoming an important tool for studying neuronal networking and physiology [96].

Employing a realistic ECM in these models is essential to promoting cell growth

and realistic cell-ECM relationships [96]. A recent study from the Kaplan Laboratory evaluated the effects of three types of ECM (adult, fetal, and collagen), as well as the effects of matricellular proteins on neuronal network formation in 3D engineered cortical tissue [97]. Multiple parameters were used to evaluate the effects of each ECM condition, including morphology, cell viability, and functional activity [97].

In this study, one metric of neuronal network health was morphological neurite density as measured using TPEF imaging [97]. TPEF proved to be a useful approach for quantifying structure of neuronal networks in 3D tissue specimens due to its high resolution, signal-to-noise ratio, and optical sectioning capabilities [15]. We developed an automated image analysis approach to quantify neuronal network density in order to statistically test differences between the ECM conditions. The approach successfully showed improvements in network density in adult and fetal ECM conditions, as well as conditions with added matricellular proteins, relative to the collagen control.

3.B. MATERIALS AND METHODS

3.B.1. DATA COLLECTION

Images of 3D bio-engineered brain models using multiple ECM conditions (collagen, adult ECM, fetal ECM, +/- matricellular proteins) were provided by collaborator Disha Sood from the Kaplan Laboratory. Details of cell culture can

be found in the published study [97]. Samples were formalin-fixed and stained with a primary mouse monoclonal antibody for beta-III-tubulin, a neuronal marker, and a corresponding anti-mouse Alexa 488 fluorescent secondary antibody. Sood acquired images of the samples using an SP2 Leica confocal microscope fitted with a Ti:Sapphire laser. Light was focused to the sample using a 20x objective (0.7 NA air). Samples were excited at 760nm and fluorescence emission was collected via a non-descanned detector centered at 525nm +/- 25nm. 1024x1024 pixel images (corresponding to a 750x750micron field of view) were acquired in z-stacks of 150-200 1micron steps to capture the neurite networks. One z-stack was obtained for each of n=4-5 cultures per ECM condition.

3.B.II. IMAGE ANALYSIS APPROACH

Images were processed in several steps to smooth neurites, remove cell bodies, identify the neurite area and appropriate background area, and obtain a final neurite density value. First, image contrast was enhanced. Next, Gaussian bandpass filtering was applied to smooth the features of the images. An intensity-based adaptive thresholding approach (Otsu method) was used to generate an initial cell mask, which was then multiplied by the original image to remove background. The contrast of the resulting image was enhanced again, followed by sequential bandpass filtering. Tophat filtering was employed to further separate sharp peaks in the image, and the image was binarized based on a global intensity threshold. Small objects less than 50 pixels in size were removed from the image,

and morphological operations were performed to bridge disconnected pixels and to smooth the edges of the mask by including pixels with a majority of on pixels in their 9x9 nearest neighborhood. This binarized image served as the neurite mask for calculating total neurite area. In order to determine neurite density, we identified an appropriate background region by excluding areas where few / no neurite extensions were observed. To identify this region, we dilated the final neurite mask by successively increasing radii (25, 50, 100, 150, or 200 pixels) until there were 5 or fewer connected components in the image. This dilated mask represented the background area mask. Neurite density was obtained by dividing the number of positive pixels in the neurite area mask by the number of pixels in the total background area mask. Percent neurite density for a given z-stack was calculated as the average of the percent neurite density across the images comprising the z-stack.

3.B.III. STATISTICS

Statistical analysis was performed using JMP. Group mean neurite density values were compared using a one-way analysis of variance followed by a post-hoc Dunnett Test using “collagen without matricellular proteins” as the control. Error bars indicate standard error. * indicates $p < 0.05$, ** indicates $p < 0.01$, and *** indicates $p < 0.001$.

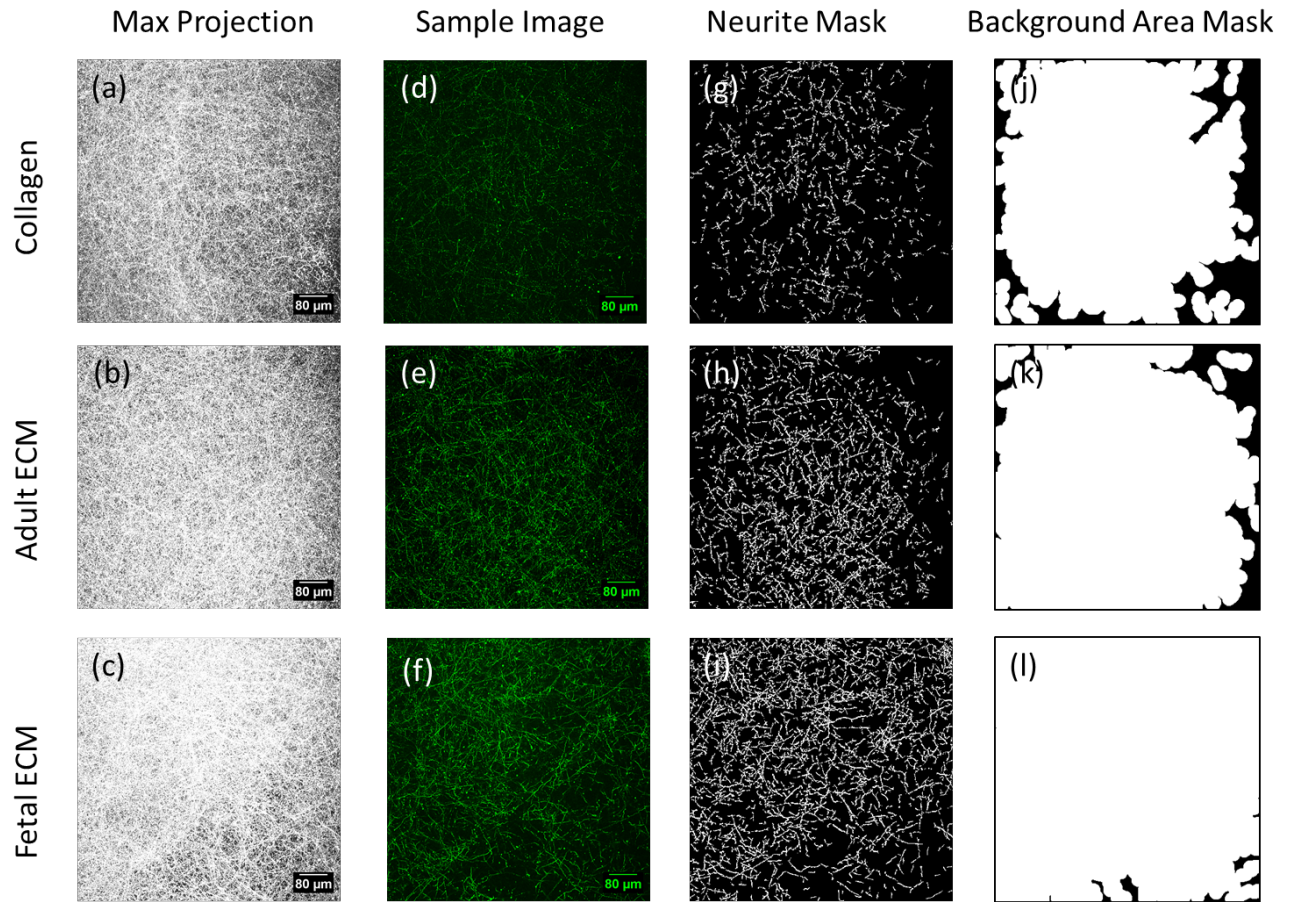


Figure 72: Representative images and masks from various ECM conditions (a-c) Maximum projection images of z-stacks (d-f) Representative raw images (g-i) Neurite masks (j-l) Background area masks

3.C. RESULTS

Z-stacks of neurite networks in stained 3D bioengineered cortical models were obtained using two-photon fluorescence microscopy. We used an automated image analysis approach on each image within each z-stack to quantify the stack's average percent neurite density. The approach was able to incorporate results from individual images in order to provide detail not available from maximum

projections of the stacks (Figure 72a-f). In determining average neurite density, the analysis both identified the neurite regions (Figure 72g-i) as well as relevant background regions, excluding background areas where neurite growth was minimal (Figure 72j-l).

Statistical comparisons of percent neurite density between different ECM conditions (collagen, fetal ECM, adult ECM, with or without matricellular proteins) showed that mean neurite density in both of the fetal ECM conditions

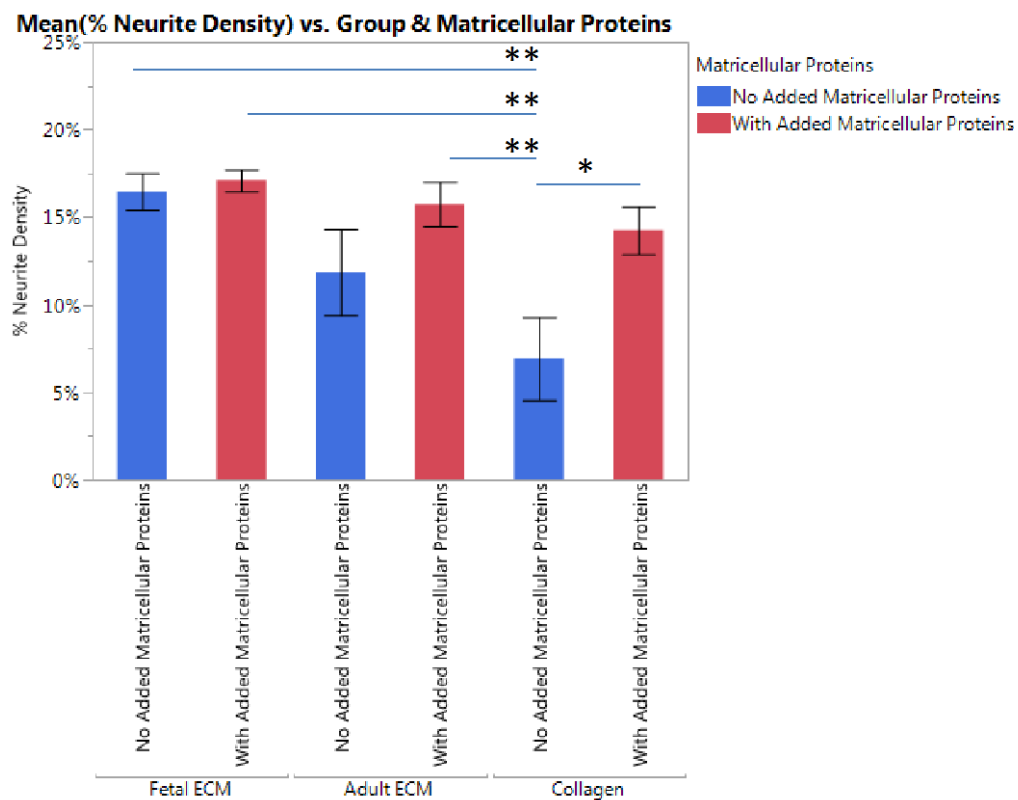


Figure 73: Comparison of neurite network density between ECM and matricellular protein conditions.

were statistically greater than the collagen control, as were the adult ECM and collagen conditions when supplemented with matricellular proteins (Figure 73).

3.D. DISCUSSION

The automated image analysis of two-photon z-stacks from 3D bioengineered cortical tissue successfully quantified visually apparent differences in the network density between ECM conditions (Figure 72a-f). Fetal ECM had a higher network density relative to the collagen control, consistent with additional supporting data that fetal ECM promotes dense neurite network formation [97]. Cultures with matricellular proteins included in the ECM also showed increased network formation relative to the collagen control, which is consistent with their known role in synaptogenesis [95]. Automated image analysis is shown to be a useful tool for quantifying neurite networks in 3D cultures in order to study the effects of culture conditions, such as ECM, on network growth.

4. OPTICAL TWEEZERS FOR THE STUDY OF LOCAL BIOMECHANICS

4.A. INTRODUCTION AND BACKGROUND

Extracellular matrix (ECM) mechanical properties are known to influence brain cell development and plasticity [98]. Research on healthy brain tissue mechanical properties has yielded a variety of results across length-scales, due to local tissue heterogeneity [99]. Use of microrheometry to assess local mechanical properties, particularly in the context of specific diseases or injuries (such as traumatic brain injury), has been more limited [99]. With the advent of functional, three-dimensional tissue-engineered brain models [96] measurements of local tissue mechanical properties could provide a valuable understanding of mechanical cues involved in both normal and pathological processes.

To this end, an optical tweezing instrument has been developed for the study of local ECM biomechanics [3]. Optical tweezers (OT) consist of a laser beam tuned to trap microscale particles through a balance of gradient and scattering forces. Optical tweezers apply force to particles, and the associated displacement can be used to calculate substance viscoelastic moduli [100]. Our optical tweezers system simultaneously displaces and images a fluorescent polystyrene bead by raster-scanning the tweezer beam over the bead and collecting the bead's fluorescence response. The apparent bead enlargement in the resulting scanning traction image reflects bead displacement [3]. Because the

traction imaging is fluorescence-based, the system is well-suited for integration with two-photon excited fluorescence imaging and second harmonic generation imaging, which would allow for future determination of relationships between cell metabolism, collagen organization, and ECM mechanical properties.

Tissue stiffness is quantified in terms of elastic modulus, a ratio between stress and strain during elastic deformation [101]. In our system, bead displacement is calculated based on the enlargement of a polystyrene bead in a scanning traction image and is related to elastic modulus as follows:

$$G' = \frac{k_{trap}\sigma}{2\pi ax_{gel}\sqrt{2e}} \quad (1)$$

G' is elastic modulus, k_{trap} is the stiffness constant of the tweezer, σ is the Gaussian profile width of the laser beam, a is the bead radius, and x_{gel} is the maximum displacement of the bead by the tweezing beam [3, 102]. Once k_{trap} has been calibrated, local G' measurements can be taken in tissue samples by simply measuring x_{gel} from scanning traction images of beads in a given tissue region.

Previous work on this system provided some technical validation of the approach, as well as results of initial microrheometry measurements in breast tissue models [3]. The technical validation successfully showed directional increase of bead displacement in collagen gels with increasing tweezer power, as well as a steeper increase in displacement with laser power for collagen gels with lower bulk elasticity than gels with higher bulk elasticity [3]. The tweezer

stiffness constant was calculated using equation (1) by measuring the bulk stiffness (G') of one of the collagen gels with parallel plate rheometry, and displacement (x_{gel}) from scanning traction images. This calibrated trap stiffness was then used to calculate G' from direct measurements of bead displacement in engineered tissue [3].

Proper calibration of OT is essential for taking accurate direct measurements of substance stiffness. The calibration approach in the initial studies has certain weaknesses. First of all, calculating stiffness constant from equation (1) assumes that bulk (G') value of a given gel represents local microrheology. Microrheology of collagen gels is known to be very heterogenous [103-105]. Therefore, bulk moduli of collagen gels are not necessarily representative of local gel stiffness, and the calibrated trap constant may not be accurate. Second of all, the trap stiffness constant was previously calibrated based upon a single gel and measurement of G' . It remains to be demonstrated that the relationship in equation (1) holds true between multiple gels (i.e., whether the trap stiffness constant is consistent for a given laser power across gels). There is no study of the predictive power of the instrument, and based on this initial work, we cannot yet be confident of its precision or accuracy.

To address these concerns, we set out to calibrate the system using polyacrylamide gels, which are known to have consistent rheology across length scales [106]. We assessed the power-dependence of bead displacement in

polyacrylamide. We also compared the average displacement of beads in gels of differing bulk stiffnesses (e.g., 6 vs. 23 pascals). We ultimately demonstrate the limited sensitivity and predictive power of the tweezing system in polyacrylamide.

Calibration concerns aside, previous research in collagen gels also raised the question of whether or not the OT system samples primarily the elasticity of the collagen fiber network, or additionally reflects how easily the beads move through the gel pores and interstitial space [3]. This issue has been similarly raised by other researchers studying the complex and heterogenous local composition and rheology of collagen gels [103]. In order to shed light on this question, we conducted additional experiments in collagen gels. We first reproduced the power-dependence trends previously observed in collagen gels. We then added a high concentration of chemical cross-linker to bind beads to the collagen network, and no longer observed the same power-dependence trends. This result suggests that microrheometry measurements cannot be directly mapped to collagen network stiffness.

4.B. MATERIALS AND METHODS

4.B.1. INSTRUMENTATION

The instrument used for these experiments consisted of a custom-built inverted microscope allowing for the capture of confocal reflectance, two-photon

beam over a small area of the sample ($\sim 7 \times 7$ microns) centered on a fluorescent, 2-micron polystyrene bead. As the tweezing beam was scanned over the bead, we assumed that the bead came to an equilibrium position with respect to the beam. The fluorescence generated by the interaction between the bead and the beam at each position was collected by the PMT, directed into an amplifier, collected by a DAQ board, and used to construct an image in another custom Labview program. The scanning traction images were captured in approximately 50s/frame, with a ~ 20 ms dwelltime per pixel. 1000 samples were averaged at each pixel to give the final pixel value. We imaged ~ 10 beads per condition (i.e. gel preparation or laser power).

4.B.II. PREPARATION OF CALIBRATION GELS

We prepared 3 mg/ml collagen gels according to standard methods of raising the pH of a collagen solution with NaOH. Carboxyl-functionalized 2 micron fluorescent beads were included in the solution at a concentration of 0.01% w/v. Prior to the addition of NaOH, either a high (10 mg/ml) or low (0.3 mg/ml) concentration of 1-ethyl-3-(3-dimethylaminopropyl) carbodiimide hydrochloride (EDC) was added. The EDC high concentration is thought to be sufficient to cross-link carboxyl beads to substrates, in this case the collagen gel [107]. The low concentration served as a control. A parallel plate rheometer measured the bulk rheometry of the two gels to be approximately 15 pascals.

Polyacrylamide hydrogels were prepared with 3% acrylamide, 0.04-0.05% bis-acrylamide according to standard methods [108]. Polystyrene 2-micron fluorescent beads were included in the gels at a concentration of 0.01% w/v. Parallel plate rheometry measured the bulk rheometry of these gels to be between 5 and 50 pascals, depending on the concentration of bis-acrylamide. The presence of polystyrene beads did not impact the bulk rheometry of the gels.

4.B.III. IMAGE ANALYSIS

We used an automated Matlab script to determine the equivalent diameter of the optically trapped beads (Figure 75). The script first normalized the intensity values in the image to account for differences in gain between different images. The script then determined the average and standard deviation of the image background intensity based upon a band of dark pixels around the perimeter of the image. The image was binarized, with the intensity threshold set to be two standard deviations above the average background intensity. Built-in Matlab functions were used to approximate the mask as an ellipsoid and return values of the bead major and minor axes. These axes were converted to micron-scale

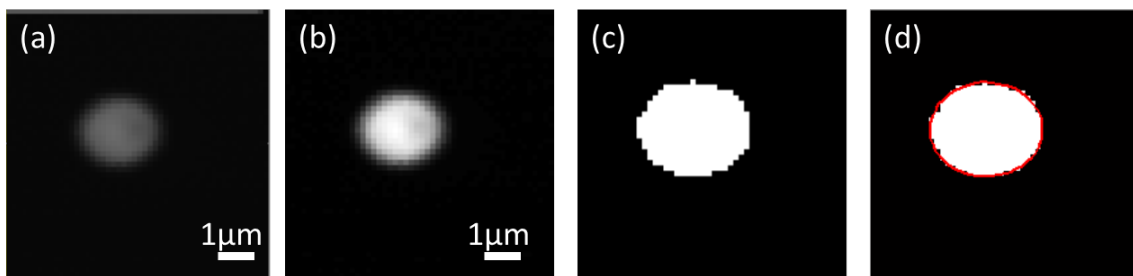


Figure 75: (a) Raw bead image (b) Normalized bead image (c) Bead mask (d) Mask with ellipsoid fit

lengths, and an equivalent diameter was calculated (diameter of a circle with the same area as the ellipse measured).

4.B.IV. STATISTICS

Statistical software (JMP) was used to evaluate differences in mean bead equivalent diameter between groups (i.e., gel preparations, fixed laser power). First, image-wise values were split by group to identify and exclude outliers (<2% of the data). Outliers were identified as values falling greater than 1.5 times the interquartile range above the 75th quantile of the data, or 1.5 times the interquartile range below the 25th quantile of the data. When the final data set was established, a linear regression model was specified and an F-test was used to assess the significance of the fixed effect (e.g., laser power). If the effect was significant, a post-hoc Tukey HSD test was applied to determine the significance of difference between groups. Error bars indicate standard deviation. * indicates $p < 0.05$, ** indicates $p < 0.01$, and *** indicates $p < 0.001$.

4.B.V. NOTES ON ALTERNATIVE METHODS:

Previous research in collagen gels employed a 40x water immersion objective (1.1 NA) for trapping and imaging. However, when we used this objective in ~20 pascal polyacrylamide gels, we did not see any significant increase in apparent bead diameter for powers between approximately 1 and 7 mW at the stage. We concluded that the trapping was not strong enough to displace beads in polyacrylamide and therefore explored two higher-NA options –

a 60x oil immersion objective (1.4 NA) and a 63x water immersion objective (1.2 NA). Relative to the 40x objective, the 60x and 63x objectives had much lower power throughput (62% of power through 40x vs. 28% through the 60x and 18% through the 63x), meaning that more power must be directed to the tweezing beam (vs. the fast-frame imaging beam) to achieve a given power at the stage. For example, to achieve 7mW power at the stage, ~120mW was directed through the tweezing beamline for the 40x, ~350mW for the 60x, and ~560mW for the 63x. Most (>80%) of this power was lost through the 70:30 beam-splitter and mirrors, however the objective used still impacted throughput significantly (error in power measurements were due to the use of different power meters at different scales). It is also worth noting that for the 63x objective, the poor throughput eventually limited data collection for high powers at the stage; when most of the laser power was directed to the tweezing beam (rather than the imaging beam), the user had no fast-imaging guidance for positioning the tweezing beam relative to the sample.

We qualitatively compared the differences in optical trapping between the three objectives by using them to trap 2-micron beads suspended in water at power values of 1, 3, 5, and 7 mW at the microscope stage. In this comparison, the 60x objective showed, qualitatively, the most consistent trapping throughout the 1-7 mW power range. Because the 60x objective had the highest numerical

aperture, reasonable power throughput, and appeared to trap beads most readily in water, we employed it for the experiments described.

Polyethylene oxide solutions were also initially prepared as potential calibration samples, given their consistent rheology across length-scales [109]. Solutions measured an elastic modulus of ~20 Pa for 6% w/v PEO. We deprioritized PEO-based approaches because PEO has a more significant viscous character (higher G'') than PA for the same elastic modulus (G') value, which would have complicated interpretation of results and cross-validation with other microrheometry approaches, such as atomic force microscopy.

We attempted to prepare a 3 mg/ml collagen gel with 0.01% w/v non-functionalized fluorescent polystyrene beads and a high concentration of EDC as an additional control. However, multiple samples of this preparation failed to gel properly, dissolving upon addition of phosphate buffered saline – perhaps due to an interaction between the EDC and the bead solvent.

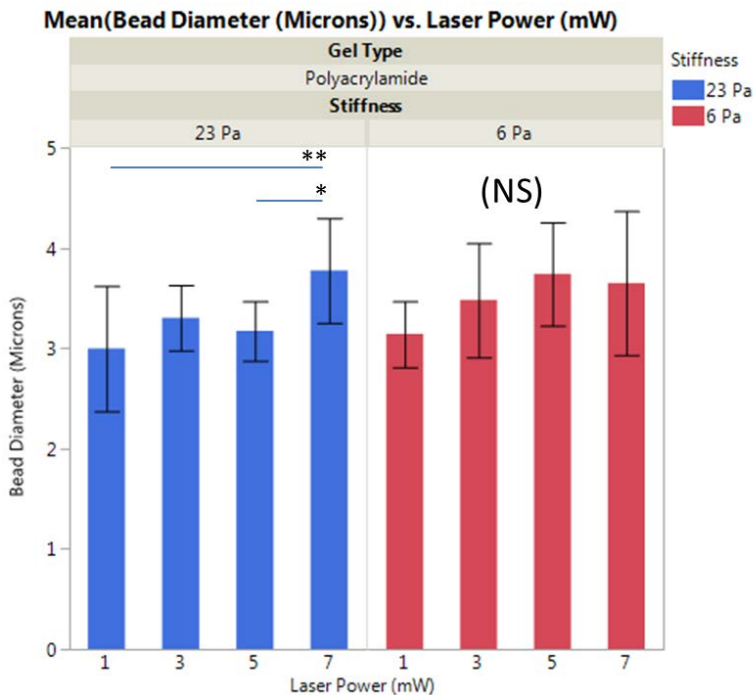
The above described image analysis approach was consistent with previous experiments (Peng, 2013). However, a range of alternative approaches were explored and compared via a study of carboxyl-functionalized beads fixed to a collagen-coated plate with EDC. 10 scanning traction images were taken of the same EDC-linked bead. The images were analyzed using five different approaches and the standard deviations of the calculated diameters were evaluated for consistency. The beads were first sized manually in ImageJ, which gave an

average bead diameter of 2.3 microns and a standard deviation of 0.14 microns. Next, they were analyzed with a standard-deviation-based thresholding approach (as described above, though without intensity normalization), which gave an average bead diameter of 3.9 microns and a standard deviation of 0.9 microns. They were also evaluated using the Otsu method, yielding an average bead diameter of 1.9 microns and a standard deviation of 0.057 microns. In another approach, a Gaussian curve was fit to the row in the image that contained the maximum intensity. The full-width at half maximum of the Gaussian curve was used to characterize the diameter of the image. This approach gave 1.5 micron FWHM in both the x- and y-directions, with standard deviations of 0.015 and 0.020 in the x- and y-directions, respectively. Finally, bead size was characterized by calculating the intensity-weighted standard deviation of bead position in the row and column containing the brightest pixel. This approach yielded a 1.4 micron average diameter and 1.2 micron standard deviation.

While the Otsu method gave a low standard deviation between samples, it generally gave a bead diameter value slightly lower than the known size of the bead. This result suggested that signal around the edges of the bead was truncated by the binarization, which is disadvantageous, given that we expected to detect small changes in bead position in the changes in signal towards these edges. The Gaussian-curve fitting approach was considered unsuitable because the fluorescent response function of the bead to the tweezing beam was not actually

Gaussian. Finally, calculating the standard deviation of intensity-weighted position would make sense in the case where the bead fluorescence was greatest at the center of the bead, and consistently decreasing with position on either side of the bead. However, the bead images frequently displayed dark spots possibly due to photobleaching, sectioning, and other artifacts. These artifacts impacted the intensity-weighted position analysis, giving high variation and unrepresentative results. For all of these reasons, we chose to retain the original thresholding approach because it captured the intensity above the background near the edges of the bead without being impacted by the presence of dark spots. Ideally, future work would computationally model the expected fluorescence response of the bead to the incident laser beam at each pixel, and characterize bead size based on

Figure 76 The apparent size of polystyrene beads in a 23- and 6-pascal polyacrylamide gel



fitting images to this model. However, such an analysis would still need to account for bead photobleaching.

4.C. RESULTS

4.C.I. MEASUREMENTS IN POLYACRYLAMIDE GELS

Collagen gels are known to have a high

degree of heterogeneity in local rheology [103-105]. Because their local values are not reliably consistent with bulk rheometry values, collagen gels are not suitable for system calibration. In effort to clarify previous results in collagen and obtain values with which to calibrate the optical tweezers measurements, we performed power-dependence studies in polyacrylamide gels, which are known to have consistent rheometry across length-scales [106]. Beads embedded in a 23 pascal polyacrylamide gel showed a significant increase in apparent bead diameter between 1 and 7 mW power and between 5 and 7 mW (Figure 76). Beads embedded in a softer, 6 pascal polyacrylamide gel showed a qualitatively similar increase in apparent bead diameter with power, however, differences between levels were not statistically significant (Figure 76). It appears that some increases in power do increase bead displacement in polyacrylamide gels, as with prior results of unbound beads in collagen gels. However, the lack of consistently statistically significant differences between laser powers in soft polyacrylamide gels suggests that a greater increase in power is required to see a significant displacement than in polyacrylamide than in collagen gels with similar bulk moduli.

To determine whether or not bead displacements in polyacrylamide could reflect differences between two gel stiffnesses within the 1-7 mW power range, we directly compared the results from the 6 and 23 pascal gels. There was no significant difference between the measured bead diameters for the two gels,

except at 5 mW (Figure 77). This result suggests that bead displacements in this OT system may not be sufficiently sensitive to predict differences in gel stiffness on this scale.

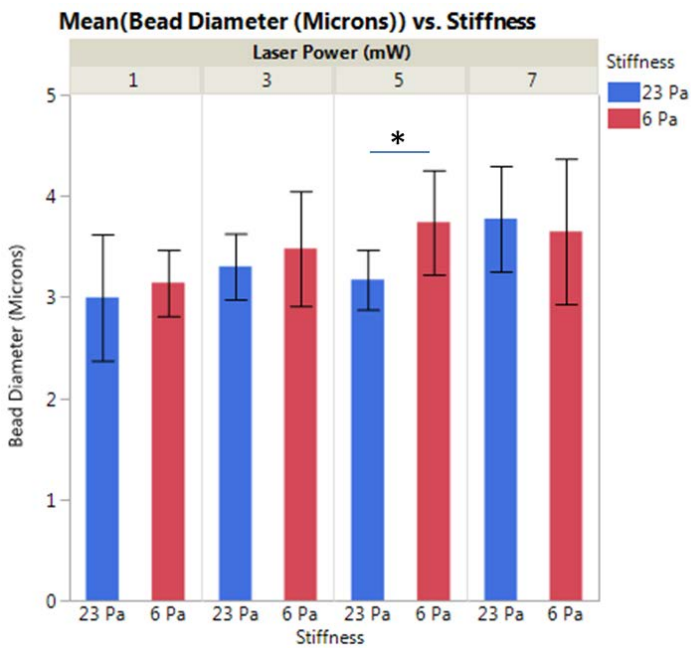


Figure 77: Comparison of apparent bead diameters in polyacrylamide gel

4.C.II.

MEASUREMENTS IN COLLAGEN GELS

In addition to collecting calibration data in polyacrylamide gels, we also sought to

confirm previous data in collagen gels, and

assess whether or not measurements were probing the elasticity of the collagen network, or simply the space between fibers. In order to test this, we first examined the power-dependence of apparent bead diameter in collagen gels with a low concentration (0.3 mg/ml) of EDC chemical crosslinker. Next, we added a high concentration of EDC (10 mg/ml) to examine how cross-linking beads to the collagen network would impact the apparent diameter relative to the low-EDC condition. When a 15 pascal collagen gel was prepared with carboxyl-

functionalized beads and a low concentration of EDC, we observed significant differences in apparent bead diameter between optical tweezer power levels of 1 mW and 5 mW, and 1 and 7 mW (:). This result was consistent with previous results suggesting beads are displaced more significantly within collagen gels as optical tweezer power is increased [3]. However, the question remained of whether the restoring force of the gel on the optical tweezers was truly due to the elasticity of the collagen network, or a combined result of the elastic collagen network, and beads sliding through interstitial fluid. When a high concentration of EDC was added to crosslink the beads to the collagen gel [107], the clear power trend disappeared. There was no statistically significant difference between the average diameter measured at 1 mW and those measured at 3, 5, or 7 mW (Figure

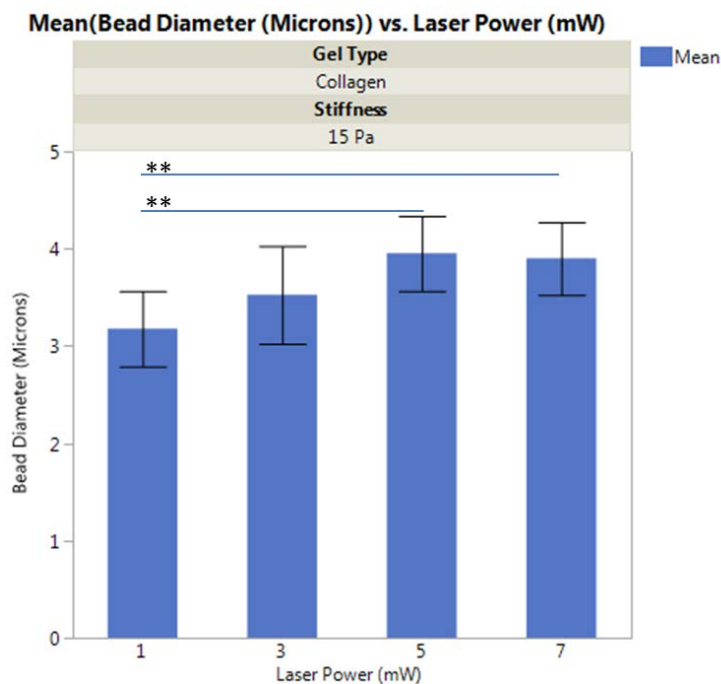


Figure 78: The apparent size of carboxyl-functionalized beads in a 15 pa collagen gel prepared with a low concentration (0.3mg/ml) of EDC

79). Assuming that low concentrations of EDC are insufficient to bind beads to collagen, and high concentrations of EDC are sufficient to bind collagen, these results suggest that this optical tweezing

system can displace beads that are unbound to the surrounding collagen network, but cannot displace beads bound to the surrounding collagen network within this power range. The consistent bulk elastic modulus (15 pascals) between the two gels suggests that increasing EDC concentration does not alter bulk collagen gel stiffness.

4.D.

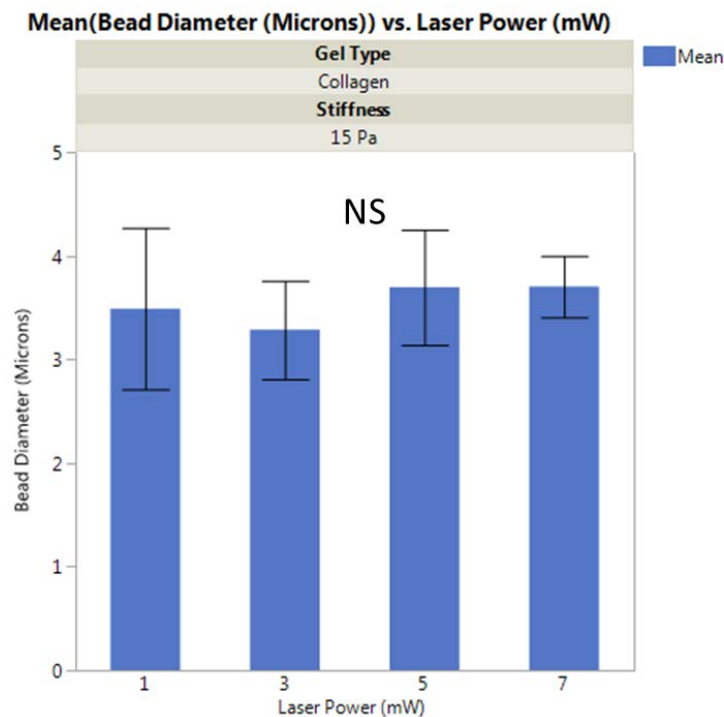


Figure 79: The apparent size of carboxyl-functionalized beads in a 15 pa collagen gel prepared with a high concentration (10mg/ml) of EDC

DISCUSSION

The results of these experiments present several questions regarding the project's technical feasibility using current approaches. Reliable determination/calibration of the OT trap stiffness constant is essential to obtain accurate microrheometry measurements with the system. The existing calibration approach, which relies on relationships between bead displacement and bulk G'

values, has faced challenges. First of all, beads embedded in polyacrylamide do not consistently show significant displacement increases (as indicated by apparent bead diameter) at the same power levels required to displace beads embedded in collagen gels of comparable bulk stiffness. Without sensitive data from a gel that has consistent rheology across length scales, this calibration approach will not be feasible. Perhaps more importantly, bead displacement does not appear consistently different/distinguishable between gels of different elastic moduli (6 pascals vs. 23 pascals). Calibrating with each of these gels would therefore yield different trap stiffnesses for a given power level; even if a single value were determined, it is doubtful whether resulting measurements of G' would be particularly sensitive on the order of pascals (or even tens of pascals). In all, this calibration (and measurement) approach may not be sensitive enough for the types of measurements we hope to take with the system.

There are various possibilities for addressing these technical challenges. To increase trap strength and therefore bead displacement in polyacrylamide, we could slightly increase the size of the microsphere probes. We could also increase the laser power, though power will ultimately be limited by photobleaching (an effect we already witness at 7mW) and cell viability in engineered tissue systems. We could also use a calibration approach that does not rely on comparisons with bulk measurements, for example, determining tweezer stiffness with an oscillating trap in water [104, 105]. However, even if the system is properly calibrated, there

still remains the question of the reliability and sensitivity of measurements, if there is no significant difference in bead diameter at 6 vs. 23 pascals. Improving this sensitivity may require upgrading to a more sensitive position detection system, similar to those used by other researchers (e.g., quadrant photodiode or videocamera) [103-105]. Finally, data analysis approaches could be improved by modeling the bead's expected fluorescence response when interacting with the tweezer beam and characterizing bead displacement based upon image fits to this model. However, such a model would have to account for photobleaching artifacts in order to be useful.

Even if calibration were possible, there also remain questions regarding the broader purpose and significance of the project. First of all, it is unclear that the dynamic range of the instrument could measure physiologically relevant stiffness values. Some literature values have suggested that brain ECM may be as stiff as ~1000 pascals [110], and the 3D-engineered brain cultures in the Kaplan Laboratory utilize a 100-1000 pascal collagen gel. If our system has low sensitivity in the <25 pascal range, it may not give meaningful measurements in the range of hundreds (or thousands) of pascals.

Even more broadly, collagen gels are a very heterogenous medium, and optical tweezer microrheometry may be difficult to interpret. While it would be desirable to sample primarily the elasticity of the collagen fibril network surrounding the gel, individual fibrils are known to have elastic moduli on the

order of megapascals [111, 112]. Our results are consistent with a very stiff collagen network – beads bound to collagen fibers with a high concentration of EDC cannot be displaced by our optical tweezing system in the power range tested. Therefore, it is unlikely that microrheology measurements (which are typically on the order of tens of pascals) of unbound beads are sampling collagen network stiffness [103-105]. Additionally, Shayegan and Forde note that collagen gel pore sizes are much larger than the probe beads used [113]. They therefore conclude that microrheometry measurements of collagen reflect a combination of collagen fibril stiffness, ease of bead migration through gel pores, and solvent viscosity [103]. Whether or not these measurements are valid or valuable remains an object of debate.

All in all, the current experimental approaches have been unsuccessful in providing data for sensitive calibration of the OT system. The experiments have also revealed that OT bead displacement (according to scanning traction images) is not sensitive to increases in gel stiffness on the order of 10-20 pascals. Additionally, current literature questions the usefulness of microrheometry in collagen gels. Careful consideration of these challenges is needed to determine the best path forward with development of this microrheometry instrument.

5. THESIS CONCLUSIONS AND FUTURE RESEARCH

DIRECTIONS

The studies described in this thesis show the broad potential for the application of TPEF to a range of questions in neuroscience and tissue engineering. Each project yielded key conclusions, and also laid the groundwork for future experiments.

The metabolic imaging studies offered several major conclusions. By analyzing distributions of astrocyte and neuron optical redox ratios, we showed that neuronal distributions tended to have greater weight on high redox ratios than astrocyte distributions, indicating more exclusive reliance on oxidative phosphorylation for energy production. This result was consistent with previous research characterizing astrocyte and neuron metabolic profiles as more glycolytic and more oxidative, respectively [8]. We also showed that astrocyte and neuron redox ratio distributions have increasing weight on very high redox-ratio components when treated with manganese, a neurotoxin yielding similar clinical effects to PD. These results were consistent with higher weight on high redox ratio components in PD-derived AHNPs, drawing a link between autofluorescence changes in PD and manganese poisoning. While previous study of optical redox ratios in neurodegeneration has been limited, increased redox ratios have been shown to be related to apoptosis and oxidative stress, both

features of neurodegeneration, in other cell types and disease models [60-62, 64]. Though we imaged cells in a number of co-culture conditions, we did not collect any conclusive evidence that co-culturing cells altered optical redox ratio or changed the impacts of manganese on cells. However, these experiments in sum demonstrate the utility of TPEF in capturing metabolic information about brain cells via NADH and FAD autofluorescence that is consistent with previous neuroscience research.

These initial metabolic imaging studies lay the groundwork for addressing a number of future neuroscience-related research questions using TPEF. One potential future research direction would involve joining the broader research conversation regarding autofluorescence in neuronal firing [73]. Previous studies have highlighted the difficulty of isolating sources of autofluorescence signals in brain slices [73]. Our high-resolution imaging approach in 2D cultures may be uniquely suited to characterize this signal, either cellularly or subcellularly, in conjunction with chemical stimulation and / or patch-clamping. In addition to localizing the signal or attributing it to a particular organelle or cell type, redox ratio distributions could offer insight into metabolic changes reflected by the autofluorescence. Additionally, incorporating electrical stimulation into the metabolic imaging could allow for clearer detection and characterization of cell-cell metabolic coupling in mixed cultures.

The neurite analysis approach described in the thesis highlights TPEF's ability to provide quantitative structural information in stained 3D bioengineered cortical tissue. We successfully quantified neurite network density through an automated image processing algorithm which showed significant increases in neuronal network density when fetal ECM, adult ECM, or matricellular proteins were incorporated in the 3D brain model, relative to the simple collagen-only control. Future research may employ a similar analysis approach to screen between various other growth conditions for optimizing tissue models.

The optical tweezers project highlighted several challenges in the development and calibration of a sensitive microrheometry tool incorporating TPEF. While previous results had shown expected increases in microsphere displacement (as measured using TPEF contrast) with increasing laser power in collagen gels, we were not able to consistently achieve the same results in polyacrylamide gels, which are more reliable for calibration given their consistent rheometry across length-scales. The results questioned the sensitivity and reproducibility of the OT measurements, as well as the strength of the OT and its potential for trapping in stiffer substances. Additional experiments in collagen gels further suggested that OT measurements sample the collagen interstitial fluid, as opposed to the elasticity of the collagen network, unless chemically crosslinked to the collagen, at which point the network is too stiff to be probed by the tweezers. While these outcomes question the validity and utility of these types of

measurements, there still remain options for improving the trap strength stiffness and measurement sensitivity, as highlighted in Section 4. However, further efforts must clearly consider the requirements of future applications in order to ensure the relevance of the instrumentation improvements.

Perhaps the most interesting potential future directions involving TPEF in brain tissue are those that would utilize combinations of the techniques and approaches described in this thesis. A logical next step would be to study endogenous cell fluorescence in 3D brain models in conjunction with quantitative studies of neurite network density. The combination of metabolic and structural information could provide new insights into metabolic processes involved in formation of neural networks. It could also provide verification of the physiological relevance of various improvements upon existing 3D bioengineered brain tissue, or development of disease models. However, these types of studies would rely on having sufficient autofluorescence signal within thick, scattering scaffolds to obtain useful metabolic information. Careful optimization of relevant imaging methods and data analysis approaches would be required. Nevertheless, these types of potential future experiments highlight TPEF's unique ability to offer non-invasive tissue assessment along with high resolution and optical sectioning, all with low enough photodamage to permit live cell imaging. TPEF is truly a unique and powerful tool with the potential to greatly enhance our

understanding of brain cell metabolism as well as structure and function within bioengineered tissue.

6. APPENDIX

CELL CULTURE PROTOCOLS:

Astrocyte Isolation and Cell Culture Protocol

Astrocyte Media Preparation (use for expanding cells):

FBS

Penicillin/streptomycin or antibiotic/antimycotic

DMEM/F12

- Supplement desired quantity of DMEM/F12 with 10% FBS and 1% Pen/Strep (or Anti/Anti)
- Filter media using a filter bottle or syringe and small filter

Co-Culture Media Preparation (use for imaging cells if comparing with neurons or co-culturing cells)

B27

FBS

Antibiotic/antimycotic

Glutamax

Neurobasal medium

- Supplement desired quantity of neurobasal medium with 2% B27, 2% FBS, 1% glutamax, and 1% anti/anti
- Filter media using a filter bottle or syringe and small filter

Astrocyte Isolation:

Embryonic day 18 rat cortices

Astrocyte media

- 1 cortex (half of brain) will give enough astrocytes for approximately 28.5 cm² of growth area
- To isolate astrocytes, add one cortex per 1 ml astrocyte media using a 25ml pipette
- Using a 10ml pipette, pipette the cortex up and down in the media 10x to break down tissue
- If there are still visible chunks, pipette additional times
- Add additional media (if needed) for seeding
- Add cells/media to culture plates, allow to attach
- Keep in incubator

Maintenance:

Change media every 2-3 days, swap to 2% FBS after 5-7 days to slow cell proliferation

Neuronal Cell Culture Protocol**Neuron Media Preparation (use when not comparing with astrocytes):**

B27

Antibiotic/Antimycotic

Glutamax

Neurobasal medium

- Supplement desired quantity of neurobasal medium with 2% B27, 1% glutamax, and 1% anti/anti
- Filter media using a filter bottle or syringe and small filter

Co-Culture Media Preparation (use for imaging cells if comparing with astrocytes or co-culturing cells)

B27

FBS

Antibiotic/antimycotic

Glutamax

Neurobasal medium

- Supplement desired quantity of neurobasal medium with 2% B27, 2% FBS, 1% glutamax, and 1% anti/anti
- Filter media using a filter bottle or syringe and small filter

Plate Coating:

Poly-d-lysine

- Prepare a 0.1mg/ml solution of PDL in sterile distilled water (enough volume to cover plates you are coating)
- Add PDL solution to plates, allow to coat for 1 hour
- Wash 3x with sterile PBS
- Leave last PBS in plates until plating cells (aspirate first)

Maintenance:

- Change media 1x weekly

REDOX RATIO AND PSD CODE

```
%%%%%%%%%%%%%%%%%%%%%%%%%%%%%%%%%%%%%%%%%%%%%%%%%%%%%%%%%%%%%%%%%%%%%%%%%
%REDOX and PSD Analysis Code
% adapted from code by Kyle Quinn (kyle@quinnlab.org)
% adapted by Emily Stuntz to incorporate new thresholding
approaches,
% calculate values for redox histograms, redox component maps
%%%%%%%%%%%%%%%%%%%%%%%%%%%%%%%%%%%%%%%%%%%%%%%%%%%%%%%%%%%%%%%%%%%%%%%%%

%% Step 0:  User inputs
function redox_psd_0603(wk,group,numb)

well=[wk,group,numb]; %subfolder for specific group
typeim='Image';%specify 'Image' or 'Series'

[~,~,ImageIndex] = xlsread('Image_List_0603.xls');
ImageIndex = ImageIndex(2:end, 1:end);
ListLength = size(ImageIndex,1);

map_stack = zeros(512,512,ListLength);
data_readout = zeros(ListLength,62);

for z=1:ListLength
%specify the image series numbers corresponding the 755, 860 nm
images
imageID = ImageIndex{z,1};
ser755=double(ImageIndex{z,2});
ser860=double(ImageIndex{z,3});

lipot=10/255;%set threshold for significant lipofuscin signal

%% STEP 1: Load the data
%create string to look up 755 images
basestr='_Image000_ch0';

if ser755>=100
    basestr(7:9)=num2str(ser755);
elseif ser755>=10
    basestr(8:9)=num2str(ser755);
else
    basestr(9)=num2str(ser755);
end
Imagename=basestr(2:9);%e.g. 'Image020'

%load the images
NDD1_755=imread([well,basestr,'0.tif']);
NDD2_755=imread([well,basestr,'1.tif']);
```

```

%find correct ND filter, objective, and
%date of the experiment
ND_755 = NDsearch_v2(well,Imagename);
ob = Objsearch_v2(well,Imagename);

%for the 755 images, find the correct gains and offsets
Gain_NDD1_755 = Gainsearch_v2(well,Imagename,'NDD1');
Gain_NDD2_755 = Gainsearch_v2(well,Imagename,'NDD2');
Off_NDD1_755 = Offsetsearch_v2(well,Imagename,'NDD1');
Off_NDD2_755 = Offsetsearch_v2(well,Imagename,'NDD2');

disp(['image data collected at 755nm loaded'])

%label the correct string for the 860 images
basestr='_Image000_ch0';

if ser860>=100
    basestr(7:9)=num2str(ser860);
elseif ser860>=10
    basestr(8:9)=num2str(ser860);
else
    basestr(9)=num2str(ser860);
end

%load the 860 data
clear NDD1_860 NDD2_860 NDD3_860

NDD1_860=imread([well,basestr,'0.tif']);
NDD2_860=imread([well,basestr,'1.tif']);
Imagename=basestr(2:9);%e.g. 'Image020'

%find correct ND filter, objective
ND_860 = NDsearch_v2(well,Imagename);
%for the 860 images, find the correct gains and offsets
Gain_NDD1_860 = Gainsearch_v2(well,Imagename,'NDD1');
Gain_NDD2_860 = Gainsearch_v2(well,Imagename,'NDD2');
Off_NDD1_860 = Offsetsearch_v2(well,Imagename,'NDD1');
Off_NDD2_860 = Offsetsearch_v2(well,Imagename,'NDD2');
disp(['image data collected at 860nm loaded'])

% convert data to 8bit range
if strcmp(class(NDD1_755),'uint16')
    NDD1_755=double(NDD1_755)/4095*255;
    NDD2_755=double(NDD2_755)/4095*255;
    NDD1_860=double(NDD1_860)/4095*255;
    NDD2_860=double(NDD2_860)/4095*255;

    disp('12bit image detected')
elseif strcmp(class(NDD1_755),'uint8')

```

```

NDD1_755=double(NDD1_755);
NDD2_755=double(NDD2_755);
NDD1_860=double(NDD1_860);
NDD2_860=double(NDD2_860);

disp('8bit image detected')
else
    disp('error');
end
%% STEP 2: Register images
%register images by computing the correlation coefficient
between 755 and 860 data for
%different shifts in the 860 position

%save initial copies of the images
NDD1_755p=NDD1_755;
NDD2_755p=NDD2_755;
NDD1_860p=NDD1_860;
NDD2_860p=NDD2_860;

%first add a buffer around the images
sp=20;
NDD1_755=zeros(2*sp+1+512,2*sp+1+512,size(NDD1_755p,3));
NDD2_755=zeros(2*sp+1+512,2*sp+1+512,size(NDD1_755p,3));
NDD1_860=zeros(2*sp+1+512,2*sp+1+512,size(NDD1_755p,3));
NDD2_860=zeros(2*sp+1+512,2*sp+1+512,size(NDD1_755p,3));

NDD1_755(sp+1:sp+512,sp+1:sp+512,:)=NDD1_755p;
NDD2_755(sp+1:sp+512,sp+1:sp+512,:)=NDD2_755p;

%register images

disp(['image registration']);
%combine the two channels
i7=NDD1_755p+NDD2_755p;
i8=NDD1_860p+NDD2_860p;
[xq,yq] = meshgrid(-sp:1:sp,-sp:1:sp);
clear Rv

%compute the correlation coefficient for different shifts
i=1;
for xd=-sp:1:sp
    for yd=-sp:1:sp
        Rv(xd+sp+1,yd+sp+1,i)=corr2(i7(sp+1:512-sp,sp+1:4:512-sp,i),i8(sp+1+xd:512-sp+xd,sp+1+yd:4:512-sp+yd,i));
    end
end

%find shift with max correlation
xqq=reshape(xq,1,[]);

```



```

yqq=reshape(yq,1,[]);
Rvq=reshape(Rv(:, :, i),1,[]);
[m ind]=max(Rvq);

disp(['860 displacement:
',num2str((xqq(ind).^2+yqq(ind).^2).^5)]);
disp(['860 correlation: ',num2str(m)]);

%shift 860 images
NDD1_860(sp+1-yqq(ind):sp+512-yqq(ind),sp+1-xqq(ind):sp+512-
xqq(ind),i)=NDD1_860p(:, :, i);
NDD2_860(sp+1-yqq(ind):sp+512-yqq(ind),sp+1-xqq(ind):sp+512-
xqq(ind),i)=NDD2_860p(:, :, i);

%now cut out that buffer region that was added to all images
NDD1_755(513+sp:2*sp+513,:)=[];
NDD1_755(:,513+sp:2*sp+513)=[];
NDD1_755(1:sp,:)=[];
NDD1_755(:,1:sp)=[];

NDD2_755(513+sp:2*sp+513,:)=[];
NDD2_755(:,513+sp:2*sp+513)=[];
NDD2_755(1:sp,:)=[];
NDD2_755(:,1:sp)=[];

NDD2_860(513+sp:2*sp+513,:)=[];
NDD2_860(:,513+sp:2*sp+513)=[];
NDD2_860(1:sp,:)=[];
NDD2_860(:,1:sp)=[];

NDD1_860(513+sp:2*sp+513,:)=[];
NDD1_860(:,513+sp:2*sp+513)=[];
NDD1_860(1:sp,:)=[];
NDD1_860(:,1:sp)=[];

clear NDD1_860p NDD1_755p NDD2_860p NDD2_755p

%% STEP 3: normalize intensities by gain and power

% if there is a positive background intensity value for some
reason
% remove that by detecting the mode of the images. This value
must be
% below an 8 bit value of 30.
ac(1)=mode(nonzeros((NDD1_755.*(NDD1_755<=30)))));
ac(2)=mode(nonzeros((NDD2_755.*(NDD2_755<=30)))));
ac(3)=mode(nonzeros((NDD1_860.*(NDD1_860<=30)))));
ac(4)=mode(nonzeros((NDD2_860.*(NDD2_860<=30)))));

```

```

NDD1_755_test = NDD1_755;
NDD1_755_test_vec =
sort(reshape(nonzeros(NDD1_755_test),1,[]),'descend');
NDD1_755_max = NDD1_755_test_vec(round((1-
0.99)*length(NDD1_755_test_vec)));
NDD1_755_test_2 = NDD1_755_test/NDD1_755_max;
NDD1_755_test_2 = NDD1_755_test_2.*(NDD1_755_test_2<1) +
(NDD1_755_test_2>=1);

NDD2_755_test = NDD2_755;
NDD2_755_test_vec =
sort(reshape(nonzeros(NDD2_755_test),1,[]),'descend');
NDD2_755_max = NDD2_755_test_vec(round((1-
0.99)*length(NDD2_755_test_vec)));
NDD2_755_test_2 = NDD2_755_test/NDD2_755_max;
NDD2_755_test_2 = NDD2_755_test_2.*(NDD2_755_test_2<1) +
(NDD2_755_test_2>=1);

NDD1_860_test = NDD1_860;
NDD1_860_test_vec =
sort(reshape(nonzeros(NDD1_860_test),1,[]),'descend');
NDD1_860_max = NDD1_860_test_vec(round((1-
0.99)*length(NDD1_860_test_vec)));
NDD1_860_test_2 = NDD1_860_test/NDD1_860_max;
NDD1_860_test_2 = NDD1_860_test_2.*(NDD1_860_test_2<1) +
(NDD1_860_test_2>=1);

NDD2_860_test = NDD2_860;
NDD2_860_test_vec =
sort(reshape(nonzeros(NDD2_860_test),1,[]),'descend');
NDD2_860_max = NDD2_860_test_vec(round((1-
0.99)*length(NDD2_860_test_vec)));
NDD2_860_test_2 = NDD2_860_test/NDD2_860_max;
NDD2_860_test_2 = NDD2_860_test_2.*(NDD2_860_test_2<1) +
(NDD2_860_test_2>=1);

NDD1_755=NDD1_755-ac(1);
NDD2_755=NDD2_755-ac(2);
NDD1_860=NDD1_860-ac(3);
NDD2_860=NDD2_860-ac(4);

NDD1_755_test_2 = NDD1_755/NDD1_755_max;
NDD1_755_test_2 = NDD1_755_test_2.*(NDD1_755_test_2<1) +
(NDD1_755_test_2>=1);

NDD2_755_test_2 = NDD2_755/NDD2_755_max;
NDD2_755_test_2 = NDD2_755_test_2.*(NDD2_755_test_2<1) +
(NDD2_755_test_2>=1);

NDD1_860_test_2 = NDD1_860/NDD1_860_max;

```

```

NDD1_860_test_2 = NDD1_860_test_2.*(NDD1_860_test_2<1) +
(NDD1_860_test_2>=1);

NDD2_860_test_2 = NDD2_860/NDD2_860_max;
NDD2_860_test_2 = NDD2_860_test_2.*(NDD2_860_test_2<1) +
(NDD2_860_test_2>=1);

% look up power measurements for that day by loading excel table
that I use
% to record every power measurement that I ever take. These
lines search
% for the excel row that matches the date, wavelength, ND filter,
and
% objective used
[ndata, headertext] = xlsread('power_bydate.xls');
datev=Datesearch(well);
dcor=(str2num(datev)==ndata(:,1));
ocor=(ob==ndata(:,2));
wcor755=(755==ndata(:,3));
wcor860=(860==ndata(:,3));
ndcor755=(ND_755==ndata(:,4));
ndcor860=(ND_860==ndata(:,4));
power_755=ndata(find((dcor+ocor+wcor755+ndcor755)==4),5);
power_860=ndata(find((dcor+ocor+wcor860+ndcor860)==4),5);

%normalize intensity data by gain, offset, power, and objective
used
NDD1_755n=transferfn2_40x(double(NDD1_755),Gain_NDD1_755,Off_NDD1
_755,power_755,ob);
NDD2_755n=transferfn2_40x(double(NDD2_755),Gain_NDD2_755,Off_NDD2
_755,power_755,ob);
NDD1_860n=transferfn2_40x(double(NDD1_860),Gain_NDD1_860,Off_NDD1
_860,power_860,ob);
NDD2_860n=transferfn2_40x(double(NDD2_860),Gain_NDD2_860,Off_NDD2
_860,power_860,ob);

%create variables for the non-normalized images, which will be
filtered
NDD1_755o=NDD1_755;
NDD2_755o=NDD2_755;
NDD1_860o=NDD1_860;
NDD2_860o=NDD2_860;

%create extra variables for the non-normalized images, which
won't be
%filtered
NDD1_755ou=NDD1_755;
NDD2_755ou=NDD2_755;
NDD1_860ou=NDD1_860;
NDD2_860ou=NDD2_860;

```

```

%determine pixels that have intensities of 255 or 0
NDD1_755sat=(NDD1_755ou==255);
NDD2_755sat=(NDD2_755ou==255);
NDD1_860sat=(NDD1_860ou==255);
NDD2_860sat=(NDD2_860ou==255);

%create a mask for the images that defines any pixel that had a 0
or 255
%value for any channel

satpix=(NDD2_755sat+NDD1_860sat+NDD2_860sat+NDD1_755sat)>0;

NDD1_755=NDD1_755n;
NDD2_755=NDD2_755n;
NDD1_860=NDD1_860n;
NDD2_860=NDD2_860n;

%apply a gaussian filter to smooth out the data spatially
h = fspecial('gaussian',[5 5],1);

%normalized data
NDD1_755=imfilter(NDD1_755n,h);
NDD2_755=imfilter(NDD2_755n,h);
NDD1_860=imfilter(NDD1_860n,h);
NDD2_860=imfilter(NDD2_860n,h);

%raw data
NDD1_755o=imfilter(NDD1_755o,h);
NDD2_755o=imfilter(NDD2_755o,h);
NDD1_860o=imfilter(NDD1_860o,h);
NDD2_860o=imfilter(NDD2_860o,h);

disp(['images normalized and filtered'])

%% STEP 4: Create cell mask

%average the non-normalized NADH and FAD channels to use for ROI
%determination

%042816 - make negative pixels equal to zero before creating mask
NDD2_755ou2 = NDD2_755ou.*(NDD2_755ou>0);
NDD1_860ou2 = NDD1_860ou.*(NDD1_860ou>0);

%combine NADH and FAD image for calculating cell ROI mask
Im2=(double(NDD2_755ou2)+double(NDD1_860ou2))/2;

```

```

% %create cell ROI mask
t = fspecial('gaussian',[3 3],1.5);
Im3 = imfilter(NDD2_755ou2,t);
Im4 = Im3.^1.75;
thr1 = multithresh(Im4,2);
mask1 = Im4>thr1(1);

Im5 = imfilter(NDD1_860ou2,t);
Im6 = Im5.^1.75;
thr2 = multithresh(Im6,2);
mask2 = Im6>(thr2(2));

mask12 = (mask1 + mask2)>0;

% %mask of regions containing no lipofuscin according to
threshold
nolipo=(NDD2_860n<lipot);

mask=mask12.*(1-satpix).*nolipo;

mask = bwareaopen(mask,50);

imwrite(mask,[imageID, '_mask_060316.png']);

%% STEP 5: Compute redox ratio at each pixel

%create version of NADH (NDD2_755) and FAD (NDD1_860) channels
with
%non-zero values for computing redox ratio (to prevent divide by
0
%errors)

%make any negative values zero
NDD1_860n2 = NDD1_860n.*(NDD1_860n>=0);
NDD2_755n2 = NDD2_755n.*(NDD2_755n>=0);

NDD1_860nc=NDD1_860n2.*(NDD1_860n2>0)+( (NDD1_860n2==0).*(NDD1_860
n2+.000000000001));
NDD2_755nc=NDD2_755n2.*(NDD2_755n2>0)+( (NDD2_755n2==0).*(NDD2_755
n2+.000000000001));

%compute redox ratio and make sure the values are between 0 and
1.
redox2=(NDD1_860nc./((NDD1_860nc)+(NDD2_755nc)));

%all pixels should be between 0 and 1;
redox3=(redox2>0).*redox2;
redox3=(redox3<=1).*redox3+(redox3>1);

```

```

%filter redox ratio
h = fspecial('gaussian',[3 3],1);
redox3f=imfilter(redox3,h);
redox4=(redox3f>0).*redox3f;
disp(['redox rate calculated'])

%compute secondary redox ratio with spatially filtered NADH and
FAD
h = fspecial('gaussian',[5 5],.55);
NDD2_755f=imfilter(NDD2_755nc,h);
NDD1_860f=imfilter(NDD1_860nc,h);
% redox_new = (NDD1_860f./(NDD1_860f+NDD2_755f));

%% STEP 6: Display redox ratio map
%create figure displaying redox map of cells on top of Im2 image
%figure;
cm=jet;%load jet color map

%create filtered version of the redox ratio with less filtering
h = fspecial('gaussian',[5 5],.55);
redox2=(NDD1_860nc)./(NDD1_860nc)+(NDD2_755nc));
redoxf=imfilter(redox2,h);
% NDD3_800f=imfilter(log10(NDD3_800n*1000),h);
NDD2_755f=imfilter(NDD2_755n,h);
NDD1_860f=imfilter(NDD1_860n,h);

%another redox ratio - calculated based on filtered versions of

clear Im

%create a nice grayscale image (avgi2) by combining the FAD and
NADH
%channels and optimizing the dynamic range so that 5% of pixels
are
%saturated and 5% of pixels are 0.

mf=max(max(max(NDD1_860f)));
mn=max(max(max(NDD2_755f)));
avgi=(NDD1_860f/mf+NDD2_755f/mn)/2;
ImR=sort(reshape(nonzeros(avgi),1,[],),'descend');
uplim=ImR(round(.05*length(ImR)));
botlim=ImR(round(.95*length(ImR)));
avgi2=(avgi-botlim)/(uplim-botlim);
avgi2=avgi2.*(avgi2<1)+(avgi2>=1);
avgi2=avgi2.*(avgi2>=0);

%reassign redox ratio jet colors to a range of your choosing
based on uplim
%and botlim, then discretize the redox values from 1-64.
cmj=jet;%cm_myo2;

```

```

uplim=1;%%ImR(round(.05*length(ImR)));
botlim=0;%%ImR(round(.95*length(ImR)));
redoxfn=(redoxf-botlim)/(uplim-botlim);
redoxfn=redoxfn.*(redoxfn<1)+(redoxfn>=1);
redoxfn=round(63*(redoxfn.*(redoxfn>=0)))+1;

%assemble the redox ratio map image in increments of different
redox ratio values
    Im=zeros(size(redoxfn,1),size(redoxfn,2),3);
for i=1:64
    imm=(redoxfn==i);
    Im(:,:,1)=Im(:,:,1)+cmj(i,1).*imm.*avgi2;%.*(1-
avgi3);%+avgi3.*imm;%NDD3_800f(:,:,istack);%red;nadh
    Im(:,:,2)=Im(:,:,2)+cmj(i,2).*imm.*avgi2;%.*(1-
avgi3);%green;fad
    Im(:,:,3)=Im(:,:,3)+cmj(i,3).*imm.*avgi2;%.*(1-
avgi3);%+avgi3.*imm;%blue;lipo
end

% figure;
% image(real(Im));axis image;axis off;
imwrite(real(Im),[imageID,'_redox_060316.png']));

%filter intensities
h = fspecial('gaussian',[5 5],.55);
NDD2_755f=imfilter(NDD2_755n,h);
NDD1_860f=imfilter(NDD1_860n,h);
NDD2_860f=imfilter(NDD2_860n,h);
redoxf=imfilter(redox3,h);
t = fspecial('gaussian',[3 3],0.5);
redoxf = imfilter(redox3,t);

% Create base matrices for component falsecoloring
bluematrix = ones(512,512);
bluematrix = bluematrix.*0.2; % assign appropriate jet color
value for blue
yellowmatrix = ones(512,512);
yellowmatrix = yellowmatrix.*0.55; % assign appropriate jet color
value for yellow
redmatrix = ones(512,512);
redmatrix = redmatrix.*0.9; % assign appropriate jet color value
for red

%thresholds based on averaging between mu values
redredox = redoxf>0.44; % add values separate between components
yellowredox = (redoxf>0.23)-redredox;
redredox = redredox.*redmatrix; % add values separate between
components
yellowredox = yellowredox.*yellowmatrix;
blueredox = redoxf<=0.23; % add values separate between
components

```

```

blueredox = blueredox.*bluematrix;
falsecolor_redox = redredox+blueredox+yellowredox;
falsecolor_redox =
falsecolor_redox.*(falsecolor_redox<1)+(falsecolor_redox>=1);
falsecolor_redox =
round(63*(falsecolor_redox.*(falsecolor_redox>=0)))+1;

%assemble the continuous tri-component map image in increments of
different redox ratio values
Im=zeros(512,512,3);
for i=1:64
    imm=(falsecolor_redox==i);
    Im(:,:,1)=Im(:,:,1)+cmj(i,1).*imm.*avgi2;
    Im(:,:,2)=Im(:,:,2)+cmj(i,2).*imm.*avgi2;
    Im(:,:,3)=Im(:,:,3)+cmj(i,3).*imm.*avgi2;
end

imwrite(Im,[imageID, '_06032016_falsecolor_midpoint.png']);
falsecolor_redox_2 = falsecolor_redox.*mask;
clear Im

Im=zeros(512,512,3);
for i=1:64
    imm=(falsecolor_redox_2==i);
    Im(:,:,1)=Im(:,:,1)+cmj(i,1).*imm;%red;nadh
    Im(:,:,2)=Im(:,:,2)+cmj(i,2).*imm;%green;fad
    Im(:,:,3)=Im(:,:,3)+cmj(i,3).*imm;%blue;lipo
end
imwrite(Im,[imageID, '_06032016_falsecolor_midpoint_mask.png']);
clear Im

clear Im

%% % STEP 7: Display intensity map

%figure;

%set upper and lower limits for the intensities of each channel
uplim=.25;
botlim=0;
%fact=ImR(round(.01*length(ImR)));
NDD2_860f=(NDD2_860f-botlim)/(uplim-botlim);
NDD2_860f=NDD2_860f.*(NDD2_860f<1)+(NDD2_860f>=1);
NDD2_860f=NDD2_860f.*(avgi2>=0);
uplim=.5;
botlim=0;
%fact=ImR(round(.01*length(ImR)));
NDD1_860f=(NDD1_860f-botlim)/(uplim-botlim);
NDD1_860f=NDD1_860f.*(NDD1_860f<1)+(NDD1_860f>=1);

```



```

NDD1_860f=NDD1_860f.*(avgi2>=0);
uplim=.15;
botlim=0;
%fact=ImR(round(.01*length(ImR)));
NDD2_755f=(NDD2_755f-botlim)/(uplim-botlim);
NDD2_755f=NDD2_755f.*(NDD2_755f<1)+(NDD2_755f>=1);
NDD2_755f=NDD2_755f.*(avgi2>=0);

%assemble and print image
istack=1;
Im(:,:,1)=NDD2_860f(:,:,istack)/max(max(NDD2_860f(:,:,istack).*mask));%red;nadh
Im(:,:,2)=NDD2_755f(:,:,istack)/max(max(NDD2_755f(:,:,istack).*mask));%green;fad
Im(:,:,3)=NDD1_860f(:,:,istack)/max(max(NDD1_860f(:,:,istack).*mask));%blue;lipo
ImZ=Im/max(max(max(Im)));
ImZ=ImZ.*(ImZ>0);

%% Step 8: Calculate average redox ratio values

%First set of values are computed from the masked region of the
image only
avgRedox=mean(nonzeros(redox3.*mask));%redox ratio computed as
average of pixel-wise ratios
avgN=mean(nonzeros(NDD2_755(:,:,istack).*mask));%NADH channel
avgF=mean(nonzeros(NDD1_860(:,:,istack).*mask));%FAD channel
avgL=mean(nonzeros(NDD2_860(:,:,istack).*mask));%Lipofuscin
channel
avgRedox2=avgF/(avgN+avgF); %redox ratio computed as ratio of
average FAD and NADH intensities

avgRedox_t = mean(nonzeros(redox_t.*mask));
%This set of values are computed from the masked region of the
curve only
avgRedoxW=sum(sum((redox3.*avgi)))/sum(sum((avgi)));
avgNW=mean(nonzeros(NDD2_755(:,:,istack)));
avgFW=mean(nonzeros(NDD1_860(:,:,istack)));
avgLW=mean(nonzeros(NDD2_860(:,:,istack)));
avgRedox2W=avgFW/(avgNW+avgFW);

%Find histogram pixel counts
filtered_data_masked_t3 = redox_t.*mask;
filtered_histogram_vector_t3 = nonzeros(filtered_data_masked_t3);
xbins = linspace(0,1,50);
counts_filtered_t3 = hist(filtered_histogram_vector_t3,xbins);

%PSD analysis
mask_psd = double(NDD2_755ou2)<=125;
imwrite(uint8(NDD2_755ou2), [imageID, '_755ou2_0603.png']);
mask_psd = mask_psd.*mask;

```

```

Im_3o = double(NDD2_755ou2).*mask_psd;
imwrite(mask_psd,[imageID, '_mask_psd_06032016.png']);

[beta_3 cloned_stack_3] =
PSDanalysis_Mask_name_KPQ_DP(Im_3o,5,5,imageID, '755', '755',1);
close

imwrite((uint8(cloned_stack_3(:,:,1))),[imageID, '_cloned_06032016
.png']);

datF=[avgRedoxW avgRedox2W avgNW avgFW avgLW avgRedox avgRedox2
avgN avgF avgL avgRedox_t beta_3 counts_filtered_t3];

%save summary data
save(['datF4_',num2str(ser755), '_',num2str(ser860)], 'datF');

%save all variables
save(['output4_',num2str(ser755), '_',num2str(ser860)]);

data_readout(z,:) = datF;

fclose all
end

xlswrite('Unmixing_Histogram_outputs_060416.xlsx', data_readout);

clear all
close all
fclose all

```

GAUSSIAN UNMIXING CODE

```
% Code to perform Gaussian unmixing on redox ratios
% Should start with a matrix containing all of the masked redox
ratio
% values from all relevant data sets
% Written by E. Stuntz

hist_vals = nonzeros(redoxvals_matrix);

iters = 10;
fitting_outputs = zeros(iters,9);

for m = 1:iters
    OPTIONS = statset('MaxIter',1000,'Display','final','TolFun',1e-
6);

    % Gaussian Unmixing
    k = 3;
    x = gmdistribution.fit(hist_vals,k,'Options',OPTIONS);

    % Extract parameters
    conv = x.Converged;
    muA = x.mu(1);
    muB = x.mu(2);
    sigmaA = x.Sigma(1,1,1);
    sigmaB = x.Sigma(1,1,2);
    weightA = x.PComponents(1);
    weightB = x.PComponents(2);
    muC = x.mu(3);
    sigmaC = x.Sigma(1,1,3);
    weightC = x.PComponents(3);

    % Order outputs by mean
    if muA == max([muA, muB, muC])
        mu1 = muA;
        sigma1 = sigmaA;
        weight1 = weightA;
        if muB == max([muB, muC])
            mu2 = muB;
            sigma2 = sigmaB;
            weight2 = weightB;
            mu3 = muC;
            sigma3 = sigmaC;
            weight3 = weightC;
        elseif muC == max([muB, muC])
            mu2 = muC;
            sigma2 = sigmaC;
            weight2 = weightC;
            mu3 = muB;
            sigma3 = sigmaB;
        end
    end
end
```

```

        weight3 = weightB;
    end
elseif muB == max([muA, muB, muC])
    mu1 = muB;
    sigma1 = sigmaB;
    weight1 = weightB;
    if muA == max([muA, muC])
        mu2 = muA;
        sigma2 = sigmaA;
        weight2 = weightA;
        mu3 = muC;
        sigma3 = sigmaC;
        weight3 = weightC;
    elseif muC == max([muA, muC])
        mu2 = muC;
        sigma2 = sigmaC;
        weight2 = weightC;
        mu3 = muA;
        sigma3 = sigmaA;
        weight3 = weightA;
    end
elseif muC == max([muA, muB, muC])
    mu1 = muC;
    sigma1 = sigmaC;
    weight1 = weightC;
    if muA == max([muA, muB])
        mu2 = muA;
        sigma2 = sigmaA;
        weight2 = weightA;
        mu3 = muB;
        sigma3 = sigmaB;
        weight3 = weightB;
    elseif muB == max([muA, muB])
        mu2 = muB;
        sigma2 = sigmaB;
        weight2 = weightB;
        mu3 = muA;
        sigma3 = sigmaA;
        weight3 = weightA;
    end
end

fitting_outputs(m,:) = [mu1, mu2, mu3, sigma1, sigma2, sigma3,
weight1, weight2, weight3];

end

```

7. REFERENCES

1. Becker, W., *The bh TCSPC Handbook, 6th Edition*. 2015.
2. Notjim. *Neuron*. 2008; Available from: https://commons.wikimedia.org/wiki/File%3ANeuron_-_annotated.svg.
3. Peng, B., *Evaluating Local Cell Matrix Mechanics with Scanning Traction Microscopy*, in *Biomedical Engineering*. 2014, Tufts University.
4. UK, C.R., *Diagram of Astrocyte*. 2014: Wikimedia Commons.
5. BruceBlaus. "*Blausen gallery 2014*". *Wikiversity Journal of Medicine* 2014; Available from: [https://commons.wikimedia.org/wiki/File:Blausen_0704_Parkinsons Disease.png](https://commons.wikimedia.org/wiki/File:Blausen_0704_Parkinsons_Disease.png).
6. UK, C.R. *Diagram of Astrocyte*. 2014; Available from: https://commons.wikimedia.org/wiki/File%3ADiagram_of_an_astrocyte_-_a_type_of_glial_cell_CRUK_029.svg.
7. Georgakoudi, I. and K.P. Quinn, *Optical imaging using endogenous contrast to assess metabolic state*. *Annu Rev Biomed Eng*, 2012. **14**: p. 351-67.
8. Magistretti, P.J. and I. Allaman, *A cellular perspective on brain energy metabolism and functional imaging*. *Neuron*, 2015. **86**(4): p. 883-901.
9. Bear, M.F., B.W. Connors, and M.A. Paradiso, *Neuroscience : exploring the brain*. 3rd ed. 2007, Philadelphia, PA: Lippincott Williams & Wilkins. xxxviii, 857 p.
10. Bhat, A.H., et al., *Oxidative stress, mitochondrial dysfunction and neurodegenerative diseases; a mechanistic insight*. *Biomed Pharmacother*, 2015. **74**: p. 101-10.
11. Prince, M., et al., *The global prevalence of dementia: a systematic review and metaanalysis*. *Alzheimers Dement*, 2013. **9**(1): p. 63-75.e2.
12. de Lau, L.M. and M.M. Breteler, *Epidemiology of Parkinson's disease*. *Lancet Neurol*, 2006. **5**(6): p. 525-35.
13. (CDC), C.f.D.C.a.P., *CDC grand rounds: reducing severe traumatic brain injury in the United States*. *MMWR Morb Mortal Wkly Rep*, 2013. **62**(27): p. 549-52.
14. Syed Hassan, S., et al., *Mental Trauma Experienced by Caregivers of Patients with Diffuse Axonal Injury or Severe Traumatic Brain Injury*. *Trauma Monthly*, 2013. **18**(2): p. 56-61.
15. Masters, B.R. and Society of Photo-optical Instrumentation Engineers., *Confocal microscopy and multiphoton excitation microscopy : the genesis of live cell imaging*, in *SPIE Press monograph PM161*. 2006, SPIE,: Bellingham, Wash. p. 1 online resource (xix, 208 pages).

16. Raichle, M.E. and D.A. Gusnard, *Appraising the brain's energy budget*. Proc Natl Acad Sci U S A, 2002. **99**(16): p. 10237-9.
17. Tomasi, D., G.J. Wang, and N.D. Volkow, *Energetic cost of brain functional connectivity*. Proc Natl Acad Sci U S A, 2013. **110**(33): p. 13642-7.
18. Hirst, J., *Energy transduction by respiratory complex I--an evaluation of current knowledge*. Biochem Soc Trans, 2005. **33**(Pt 3): p. 525-9.
19. Madamanchi, N.R. and M.S. Runge, *Mitochondrial dysfunction in atherosclerosis*. Circ Res, 2007. **100**(4): p. 460-73.
20. Cecchini, G., *Function and structure of complex II of the respiratory chain*. Annu Rev Biochem, 2003. **72**: p. 77-109.
21. Stincone, A., et al., *The return of metabolism: biochemistry and physiology of the pentose phosphate pathway*. Biol Rev Camb Philos Soc, 2014.
22. Bertholet, A.M., et al., *Mitochondrial fusion/fission dynamics in neurodegeneration and neuronal plasticity*. Neurobiol Dis, 2016. **90**: p. 3-19.
23. Santos, D. and S.M. Cardoso, *Mitochondrial dynamics and neuronal fate in Parkinson's disease*. Mitochondrion, 2012. **12**(4): p. 428-37.
24. Tondera, D., et al., *SLP-2 is required for stress-induced mitochondrial hyperfusion*. EMBO J, 2009. **28**(11): p. 1589-600.
25. Nedergaard, M., B. Ransom, and S.A. Goldman, *New roles for astrocytes: redefining the functional architecture of the brain*. Trends Neurosci, 2003. **26**(10): p. 523-30.
26. Krebs, C., J. Weinberg, and E. Akesson, *Lippincott's Illustrated Reviews: Neuroscience*. 2012, Lippincott Williams & Wilkins: Baltimore, MD.
27. Halim, N.D., et al., *Phosphorylation status of pyruvate dehydrogenase distinguishes metabolic phenotypes of cultured rat brain astrocytes and neurons*. Glia, 2010. **58**(10): p. 1168-76.
28. Lovatt, D., et al., *The transcriptome and metabolic gene signature of protoplasmic astrocytes in the adult murine cortex*. J Neurosci, 2007. **27**(45): p. 12255-66.
29. Hertz, L., L. Peng, and G.A. Dienel, *Energy metabolism in astrocytes: high rate of oxidative metabolism and spatiotemporal dependence on glycolysis/glycogenolysis*. J Cereb Blood Flow Metab, 2007. **27**(2): p. 219-49.
30. Bolaños, J.P., A. Almeida, and S. Moncada, *Glycolysis: a bioenergetic or a survival pathway?* Trends Biochem Sci, 2010. **35**(3): p. 145-9.
31. Bélanger, M., I. Allaman, and P.J. Magistretti, *Brain energy metabolism: focus on astrocyte-neuron metabolic cooperation*. Cell Metab, 2011. **14**(6): p. 724-38.

32. Franco-Iborra, S., M. Vila, and C. Perier, *The Parkinson Disease Mitochondrial Hypothesis: Where Are We at?* Neuroscientist, 2015.
33. Sarkar, S., J. Raymick, and S. Imam, *Neuroprotective and Therapeutic Strategies against Parkinson's Disease: Recent Perspectives*. Int J Mol Sci, 2016. **17**(6).
34. Naoi, M., et al., *Mitochondria in neurodegenerative disorders: regulation of the redox state and death signaling leading to neuronal death and survival*. J Neural Transm (Vienna), 2009. **116**(11): p. 1371-81.
35. Santos, D., et al., *The Impact of Mitochondrial Fusion and Fission Modulation in Sporadic Parkinson's Disease*. Mol Neurobiol, 2015. **52**(1): p. 573-86.
36. Scarffe, L.A., et al., *Parkin and PINK1: much more than mitophagy*. Trends Neurosci, 2014. **37**(6): p. 315-24.
37. Dawson, T.M. and V.L. Dawson, *Parkin plays a role in sporadic Parkinson's disease*. Neurodegener Dis, 2014. **13**(2-3): p. 69-71.
38. Chen, P., M. Culbreth, and M. Aschner, *Exposure, epidemiology, and mechanism of the environmental toxicant manganese*. Environ Sci Pollut Res Int, 2016.
39. Aschner, M., et al., *Manganese and its role in Parkinson's disease: from transport to neuropathology*. Neuromolecular Med, 2009. **11**(4): p. 252-66.
40. Brown, S. and N.L. Taylor, *Could mitochondrial dysfunction play a role in manganese toxicity?* Environ Toxicol Pharmacol, 1999. **7**(1): p. 49-57.
41. Gavin, C.E., K.K. Gunter, and T.E. Gunter, *Manganese and calcium efflux kinetics in brain mitochondria. Relevance to manganese toxicity*. Biochem J, 1990. **266**(2): p. 329-34.
42. Wang, F., et al., *Protective role of sodium para-amino salicylic acid against manganese-induced hippocampal neurons damage*. Environ Toxicol Pharmacol, 2014. **37**(3): p. 1071-8.
43. Benedetto, A., C. Au, and M. Aschner, *Manganese-induced dopaminergic neurodegeneration: insights into mechanisms and genetics shared with Parkinson's disease*. Chem Rev, 2009. **109**(10): p. 4862-84.
44. Zhang, S., Z. Zhou, and J. Fu, *Effect of manganese chloride exposure on liver and brain mitochondria function in rats*. Environ Res, 2003. **93**(2): p. 149-57.
45. Kruman, I.I. and M.P. Mattson, *Pivotal role of mitochondrial calcium uptake in neural cell apoptosis and necrosis*. J Neurochem, 1999. **72**(2): p. 529-40.
46. Arundine, M. and M. Tymianski, *Molecular mechanisms of calcium-dependent neurodegeneration in excitotoxicity*. Cell Calcium, 2003. **34**(4-5): p. 325-37.

47. Malecki, E.A., *Manganese toxicity is associated with mitochondrial dysfunction and DNA fragmentation in rat primary striatal neurons.* Brain Res Bull, 2001. **55**(2): p. 225-8.
48. Roth, J.A., et al., *Mechanisms of manganese-induced rat pheochromocytoma (PC12) cell death and cell differentiation.* Neurotoxicology, 2002. **23**(2): p. 147-57.
49. Hirata, S., et al., *Determination of rare earth elements in seawater by on-line column preconcentration inductively coupled plasma mass spectrometry.* Talanta, 2002. **58**(6): p. 1185-94.
50. Hazell, A.S., *Astrocytes and manganese neurotoxicity.* Neurochem Int, 2002. **41**(4): p. 271-7.
51. Gavin, C.E., K.K. Gunter, and T.E. Gunter, *Manganese and calcium transport in mitochondria: implications for manganese toxicity.* Neurotoxicology, 1999. **20**(2-3): p. 445-53.
52. Zwingmann, C., D. Leibfritz, and A.S. Hazell, *Energy metabolism in astrocytes and neurons treated with manganese: relation among cell-specific energy failure, glucose metabolism, and intercellular trafficking using multinuclear NMR-spectroscopic analysis.* J Cereb Blood Flow Metab, 2003. **23**(6): p. 756-71.
53. Sidoryk-Wegrzynowicz, M. and M. Aschner, *Role of astrocytes in manganese mediated neurotoxicity.* BMC Pharmacol Toxicol, 2013. **14**: p. 23.
54. Milatovic, D., et al., *Manganese induces oxidative impairment in cultured rat astrocytes.* Toxicol Sci, 2007. **98**(1): p. 198-205.
55. Alaimo, A., et al., *Manganese induces mitochondrial dynamics impairment and apoptotic cell death: a study in human Gli36 cells.* Neurosci Lett, 2013. **554**: p. 76-81.
56. Alaimo, A., et al., *Deregulation of mitochondria-shaping proteins Opa-1 and Drp-1 in manganese-induced apoptosis.* PLoS One, 2014. **9**(3): p. e91848.
57. Higashi, Y., et al., *Parkin attenuates manganese-induced dopaminergic cell death.* J Neurochem, 2004. **89**(6): p. 1490-7.
58. Zhang, H.T., et al., *PINK1/Parkin-mediated mitophagy play a protective role in manganese induced apoptosis in SH-SY5Y cells.* Toxicol In Vitro, 2016. **34**: p. 212-9.
59. Kubitscheck, U., *Fluorescence Microscopy from principles to biological applications.* 2013, Wiley,: Weinheim. p. 1 online resource (410 p.).
60. Levitt, J.M., et al., *Intrinsic fluorescence and redox changes associated with apoptosis of primary human epithelial cells.* J Biomed Opt, 2006. **11**(6): p. 064012.

61. Brewer, M., et al., *Fluorescence spectroscopy as a biomarker in a cell culture and in a nonhuman primate model for ovarian cancer chemopreventive agents*. J Biomed Opt, 2002. **7**(1): p. 20-6.
62. Ghanian, Z., et al., *Optical imaging of mitochondrial redox state in rodent models with 3-iodothyronamine*. Exp Biol Med (Maywood), 2014. **239**(2): p. 151-8.
63. Maleki, S., et al., *Mitochondrial redox studies of oxidative stress in kidneys from diabetic mice*. Biomed Opt Express, 2012. **3**(2): p. 273-81.
64. Maleki, S., et al., *Optical imaging of mitochondrial redox state in rodent model of retinitis pigmentosa*. J Biomed Opt, 2013. **18**(1): p. 16004.
65. Becker, W., et al., *Fluorescence lifetime imaging by time-correlated single-photon counting*. Microsc Res Tech, 2004. **63**(1): p. 58-66.
66. Vishwasrao, H.D., et al., *Conformational dependence of intracellular NADH on metabolic state revealed by associated fluorescence anisotropy*. J Biol Chem, 2005. **280**(26): p. 25119-26.
67. Skala, M.C., et al., *In vivo multiphoton microscopy of NADH and FAD redox states, fluorescence lifetimes, and cellular morphology in precancerous epithelia*. Proc Natl Acad Sci U S A, 2007. **104**(49): p. 19494-9.
68. Lakowicz, J.R., et al., *Fluorescence lifetime imaging of free and protein-bound NADH*. Proc Natl Acad Sci U S A, 1992. **89**(4): p. 1271-5.
69. Skala, M.C., et al., *In vivo multiphoton fluorescence lifetime imaging of protein-bound and free nicotinamide adenine dinucleotide in normal and precancerous epithelia*. J Biomed Opt, 2007. **12**(2): p. 024014.
70. Chakraborty, S., et al., *Quantification of the Metabolic State in Cell-Model of Parkinson's Disease by Fluorescence Lifetime Imaging Microscopy*. Sci Rep, 2016. **6**: p. 19145.
71. Digman, M.A., et al., *The phasor approach to fluorescence lifetime imaging analysis*. Biophys J, 2008. **94**(2): p. L14-6.
72. Kasischke, K.A., et al., *Neural activity triggers neuronal oxidative metabolism followed by astrocytic glycolysis*. Science, 2004. **305**(5680): p. 99-103.
73. Shuttleworth, C.W., *Use of NAD(P)H and flavoprotein autofluorescence transients to probe neuron and astrocyte responses to synaptic activation*. Neurochem Int, 2010. **56**(3): p. 379-86.
74. Shiino, A., et al., *Three-dimensional redox image of the normal gerbil brain*. Neuroscience, 1999. **91**(4): p. 1581-5.
75. Mayevsky, A. and B. Chance, *Intracellular oxidation-reduction state measured in situ by a multichannel fiber-optic surface fluorometer*. Science, 1982. **217**(4559): p. 537-40.
76. Mayevsky, A., *Brain NADH redox state monitored in vivo by fiber optic surface fluorometry*. Brain Res, 1984. **319**(1): p. 49-68.

77. Chia, T.H., et al., *Multiphoton fluorescence lifetime imaging of intrinsic fluorescence in human and rat brain tissue reveals spatially distinct NADH binding*. Opt Express, 2008. **16**(6): p. 4237-49.
78. Yaseen, M.A., et al., *In vivo imaging of cerebral energy metabolism with two-photon fluorescence lifetime microscopy of NADH*. Biomed Opt Express, 2013. **4**(2): p. 307-21.
79. Grosser, E., et al., *Oxidative burden and mitochondrial dysfunction in a mouse model of Rett syndrome*. Neurobiol Dis, 2012. **48**(1): p. 102-14.
80. Liu, Q., et al., *Compact point-detection fluorescence spectroscopy system for quantifying intrinsic fluorescence redox ratio in brain cancer diagnostics*. J Biomed Opt, 2011. **16**(3): p. 037004.
81. Xylas, J., et al., *Improved Fourier-based characterization of intracellular fractal features*. Opt Express, 2012. **20**(21): p. 23442-55.
82. Xylas, J., et al., *Noninvasive assessment of mitochondrial organization in three-dimensional tissues reveals changes associated with cancer development*. Int J Cancer, 2015. **136**(2): p. 322-32.
83. Stringari, C., et al., *Phasor fluorescence lifetime microscopy of free and protein-bound NADH reveals neural stem cell differentiation potential*. PLoS One, 2012. **7**(11): p. e48014.
84. Pellerin, L. and P.J. Magistretti, *Sweet sixteen for ANLS*. J Cereb Blood Flow Metab, 2012. **32**(7): p. 1152-66.
85. Muramoto, K., et al., *Frequency of synchronous oscillations of neuronal activity increases during development and is correlated to the number of synapses in cultured cortical neuron networks*. Neurosci Lett, 1993. **163**(2): p. 163-5.
86. Chiappalone, M., et al., *Dissociated cortical networks show spontaneously correlated activity patterns during in vitro development*. Brain Res, 2006. **1093**(1): p. 41-53.
87. Lee, E.S., et al., *Estrogen and tamoxifen protect against Mn-induced toxicity in rat cortical primary cultures of neurons and astrocytes*. Toxicol Sci, 2009. **110**(1): p. 156-67.
88. Walton, N.M., et al., *Derivation and large-scale expansion of multipotent astroglial neural progenitors from adult human brain*. Development, 2006. **133**(18): p. 3671-81.
89. Wang, S., et al., *Neurogenic potential of progenitor cells isolated from postmortem human Parkinsonian brains*. Brain Res, 2012. **1464**: p. 61-72.
90. Frantz, C., K.M. Stewart, and V.M. Weaver, *The extracellular matrix at a glance*. J Cell Sci, 2010. **123**(Pt 24): p. 4195-200.
91. Yue, B., *Biology of the extracellular matrix: an overview*. J Glaucoma, 2014. **23**(8 Suppl 1): p. S20-3.

92. Rauch, U., *Brain matrix: structure, turnover and necessity*. Biochem Soc Trans, 2007. **35**(Pt 4): p. 656-60.
93. Ruoslahti, E., *Brain extracellular matrix*. Glycobiology, 1996. **6**(5): p. 489-92.
94. Dityatev, A., C.I. Seidenbecher, and M. Schachner, *Compartmentalization from the outside: the extracellular matrix and functional microdomains in the brain*. Trends Neurosci, 2010. **33**(11): p. 503-12.
95. Kucukdereli, H., et al., *Control of excitatory CNS synaptogenesis by astrocyte-secreted proteins Hevin and SPARC*. Proc Natl Acad Sci U S A, 2011. **108**(32): p. E440-9.
96. Tang-Schomer, M.D., et al., *Bioengineered functional brain-like cortical tissue*. Proc Natl Acad Sci U S A, 2014. **111**(38): p. 13811-6.
97. Sood, D., et al., *Fetal Brain Extracellular Matrix Boosts Neuronal Network Formation in 3D Bioengineered Model of Cortical Brain Tissue*. ACS Biomaterials Science & Engineering, 2016. **2**(1): p. 131-140.
98. Franze, K., P.A. Janmey, and J. Guck, *Mechanics in neuronal development and repair*. Annu Rev Biomed Eng, 2013. **15**: p. 227-51.
99. Meaney, D.F., B. Morrison, and C. Dale Bass, *The mechanics of traumatic brain injury: a review of what we know and what we need to know for reducing its societal burden*. J Biomech Eng, 2014. **136**(2): p. 021008.
100. Nemet, B.A., Y. Shabtai, and M. Cronin-Golomb, *Imaging microscopic viscosity with confocal scanning optical tweezers*. Opt Lett, 2002. **27**(4): p. 264-6.
101. Askeland, D.R., *The science and engineering of materials*. 1984, Monterey, CA: Brooks/Cole Engineering Division. xv, 748, 14 p.
102. Hough, L. and H. Ou-Yang, *A new probe for mechanical testing of nanostructures in soft materials*. Journal of Nanoparticle Research, 1999. **1**(4): p. 495-499.
103. Shayegan, M. and N.R. Forde, *Microrheological characterization of collagen systems: from molecular solutions to fibrillar gels*. PLoS One, 2013. **8**(8): p. e70590.
104. Latinovic, O., L.A. Hough, and H. Daniel Ou-Yang, *Structural and micromechanical characterization of type I collagen gels*. J Biomech, 2010. **43**(3): p. 500-5.
105. Velegol, D. and F. Lanni, *Cell traction forces on soft biomaterials. I. Microrheology of type I collagen gels*. Biophys J, 2001. **81**(3): p. 1786-92.
106. Dasgupta, B.R. and D.A. Weitz, *Microrheology of cross-linked polyacrylamide networks*. Phys Rev E Stat Nonlin Soft Matter Phys, 2005. **71**(2 Pt 1): p. 021504.

107. Spherotech *Particle Coating Procedures*. 2014.
108. Tse, J.R. and A.J. Engler, *Preparation of hydrogel substrates with tunable mechanical properties*. Curr Protoc Cell Biol, 2010. **Chapter 10**: p. Unit 10.16.
109. Dasgupta, B.R., et al., *Microrheology of polyethylene oxide using diffusing wave spectroscopy and single scattering*. Phys Rev E Stat Nonlin Soft Matter Phys, 2002. **65**(5 Pt 1): p. 051505.
110. Javid, S., A. Rezaei, and G. Karami, *A micromechanical procedure for viscoelastic characterization of the axons and ECM of the brainstem*. J Mech Behav Biomed Mater, 2014. **30**: p. 290-9.
111. Shen, Z.L., et al., *Viscoelastic properties of isolated collagen fibrils*. Biophys J, 2011. **100**(12): p. 3008-15.
112. Grant, C.A., et al., *Tuning the elastic modulus of hydrated collagen fibrils*. Biophys J, 2009. **97**(11): p. 2985-92.
113. Yang, Y.L., S. Motte, and L.J. Kaufman, *Pore size variable type I collagen gels and their interaction with glioma cells*. Biomaterials, 2010. **31**(21): p. 5678-88.